Tungsten-Based Catalysts for Environmental Applications

Fabien Can, Xavier Courtois, Daniel Duprez

catalysts

MDPI

Review

Tungsten-Based Catalysts for Environmental Applications

Fabien Can *, Xavier Courtois * and Daniel Duprez

CNRS, UMR7285, Institut de Chimie des Milieux et Matériaux de Poitiers (IC2MP), Université de Poitiers, 4 rue Michel Brunet, CEDEX 09, 86073 Poitiers, France; daniel.duprez@univ-poitiers.fr

* Correspondence: fabien.can@univ-poitiers.fr (F.C.); xavier.courtois@univ-poitiers.fr (X.C.)

Abstract: This review aims to give a general overview of the recent use of tungsten-based catalysts for wide environmental applications, with first some useful background information about tungsten oxides. Tungsten oxide materials exhibit suitable behaviors for surface reactions and catalysis such as acidic properties (mainly Brønsted sites), redox and adsorption properties (due to the presence of oxygen vacancies) and a photostimulation response under visible light (2.6–2.8 eV bandgap). Depending on the operating condition of the catalytic process, each of these behaviors is tunable by controlling structure and morphology (e.g., nanoplates, nanosheets, nanorods, nanowires, nanomesh, microflowers, hollow nanospheres) and/or interactions with other compounds such as conductors (carbon), semiconductors or other oxides (e.g., TiO_2) and precious metals. WO_x particles can be also dispersed on high specific surface area supports. Based on these behaviors, WO_3-based catalysts were developed for numerous environmental applications. This review is divided into five main parts: structure of tungsten-based catalysts, acidity of supported tungsten oxide catalysts, WO_3 catalysts for $DeNO_x$ applications, total oxidation of volatile organic compounds in gas phase and gas sensors and pollutant remediation in liquid phase (photocatalysis).

Keywords: tungsten; WO_3; $deNO_x$; VOC; photocatalysis; sensor

Citation: Can, F.; Courtois, X.; Duprez, D. Tungsten-Based Catalysts for Environmental Applications. *Catalysts* **2021**, *11*, 703. https://doi.org/10.3390/catal11060703

Academic Editors: Annemie Bogaerts and Jean-François Lamonier

Received: 11 May 2021
Accepted: 28 May 2021
Published: 2 June 2021

1. Introduction

Tungsten is the metal having the highest melting point (3410 °C) and a density (19.3 g cm^{-3}) close to that of gold (19.32 g cm^{-3}). α-W (lattice type: body-centered cube) is the crystallographic stable form of tungsten (lattice parameter: 0.3165 nm) [1]. β-W is a metastable cubic (type A15) form of tungsten, first found in products of WO_3 reduction by hydrogen [2]. γ-W is an fcc form of tungsten only detected in thin film. Owing to its unique physical properties, tungsten is widely used in refractory alloys. While group 8–11 elements are currently used as nanoparticles of metals in catalysis, W-based heterogeneous catalysts contain tungsten in the form of oxides, sulfides, carbides or heteropolytungstates [3]. Although less employed than molybdenum sulfides, tungsten sulfides are essential components of hydrotreating catalysts [4,5]. More recently, catalysts and photocatalysts based on tungsten sulfides were developed for application in hydrogen production by water splitting [6–8]. Utilization of tungsten carbides for electrochemical applications was also developed in the domain of hydrogen evolution reaction [9,10]. Due to their high solubility in water, heteropolytungstates serve as precursors of tungsten in the preparation of W-based catalysts [11,12]. They are also utilized in many organic syntheses, especially in oxidation reactions [13]. Associated with metals such cobalt, heteropolytungstates are also excellent water-splitting catalysts [14].

Tungsten-based catalysts are currently utilized for environmental applications (e.g., $DeNO_x$, oxidation in gas and in liquid phases, sensors, photocatalysis). In these catalytic systems, tungsten is nearly always in an oxidized form, either as tungsten oxide particles or in strong interaction with specific supports or dopants. The structures of tungsten oxides, supported or not on other oxides, will be reviewed in Section 2. One of the specificities of tungsten oxides is their acid properties that are examined in Section 3. Catalytic

applications are then reviewed in the following sections: selective catalytic reduction of NO_x by ammonia over WO_3-V_2O_5 and other WO_3-supported catalysts (Section 4), other $DeNO_x$ applications (Section 5), total oxidation of pollutants in gas phase and gas sensors (Section 6) and total oxidation of pollutants in liquid phase with special insight into photocatalytic processes (Section 7). Selective oxidation in gas or liquid phase (for instance, in the cyclohexanol-to-ε-caprolactone process), as well as the area of heteropolytungstates, will not be reviewed in these sections. Readers interested in these topics are invited to read the recent review by Dai et al. [15]. Due to the high number of works published on the catalytic properties of tungsten-based catalysts, Sections 3–7 will be restricted to the 2014–2020 period, occasionally including some earlier reference papers.

2. Structure of Tungsten-Based Catalysts

Although it is important to stress that the bulk crystal structure may have a limited impact on catalysis since reactions occur at the surface of the crystalline solids, which may not exhibit the same chemical composition as the bulk, the structures of tungsten-based catalysts are summarized in this section to offer an in-depth introduction to the materials presented in this review.

2.1. Structure of Unsupported Tungsten Oxides

No less than seven tungsten oxides were identified in the tungsten–oxygen system [1,16]. However, three oxides are currently more often encountered in catalysis and in most applications [3]: WO_3 (yellow oxide), $WO_{2.9}$ or β-tungsten oxide (blue oxide) and $WO_{2.72}$ or γ-tungsten oxide (violet oxide).

2.1.1. Tungsten Trioxide

Tungsten trioxide has several allotropic forms, mainly two monoclinic structures (α-WO_3 and γ-WO_3), a triclinic structure (β-WO_3) and a hexagonal form (h-WO_3). All these forms of WO_3 consist of corner-sharing octahedra of WO_6 units. Monoclinic and triclinic structures form a quasicubic arrangement of the octahedra. They differ by the angles of distortion between the adjacent octahedra. Triclinic WO_3 is stable only at low temperature (T < 17 °C) [17]. Ab initio calculations showed that the ideal cubic arrangement of WO_6 blocks is not stable and would tend to tetragonal structure [18]. Sun et al. recently compared the potentialities of monoclinic WO_3 (m-WO_3) and hexagonal WO_3 (h-WO_3) in electrochemical and gas adsorption applications [19]. The structures of the two forms of WO_3 are represented in Figure 1.

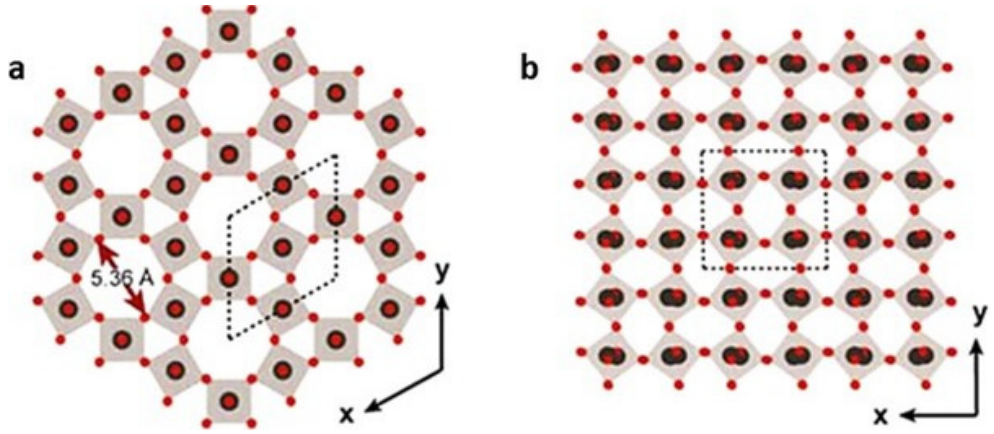

Figure 1. Structure of hexagonal WO_3 (**a**) and monoclinic WO_3 (**b**) projected along the (001) direction. Reprinted from Sun et al. [19] with permission from the American Chemical Society.

While monoclinic WO_3 possesses arrangements of small rhomboid tunnels whose great diagonals are alternatively along x and y axes, hexagonal WO_3 has a network of large

hexagonal tunnels alternating with small triangular ones. Accessibility of internal surface is then better for h-WO_3 than for m-WO_3. This was evidenced in the work of Sun et al. by a higher specific capacitance of h-WO_3 with facilitated proton transportation along the tunnels.

Szilágyi et al. investigated the behavior of m- and h-WO_3 for the photocatalytic reaction of methyl orange decomposition [20]. The two materials were prepared by annealing hexagonal ammonium tungsten bronze in air or N_2. Hexagonal WO_3 is formed by annealing the tungsten bronze $(NH_4)_xWO_{3-y}$ at moderate temperature (470–550 °C), while monoclinic WO_3 is formed at higher temperatures (600–650 °C). Decomposition processes of the hexagonal ammonium tungsten bronze were earlier investigated by the same group, who showed that residual ammonia and/or ammonium ions are vital for stabilizing the hexagonal structure [21]. Blue oxides are formed when $(NH_4)_xWO_{3-y}$ is decomposed in N_2, which shows the presence of reduced tungsten oxides. On the contrary, yellow oxides are obtained by decomposing the tungsten bronze in air. However, XPS of the oxidized materials shows that small amounts of W^{5+} and W^{4+} are still present in the h-WO_3 ox, while tungsten in m-WO_3 ox is entirely in the form of W^{6+}. Monoclinic WO_3 ox is more active than hexagonal WO_3 ox in the photocatalysis reaction because the electron–hole recombination is less probable in WO_3 having 100% W^{6+} (no defect sites). In addition to XRD, Raman spectroscopy is a good technique to distinguish hexagonal and monoclinic WO_3 phases (Figure 2). XRD spectra are consistent with m-WO_3 (ICDD file 43-1035) and h-WO_3 (ICDD file 85-2460). Peak width broadening observed on reduced samples is indicative of distortion and creations of defects in the structure. O-W-O stretching bands allow to clearly distinguish m-WO_3 (two bands at 714 and 806 cm^{-1}) and h-WO_3 (three bands at 651, 693 and 786 cm^{-1}). By contrast, O-W-O deformation vibrations, in the 260–330 cm^{-1} range, are virtually recorded at the same wavenumber for the two forms of WO_3. For that reason, deformation vibration bands cannot be used for the characterization of m- and h-WO_3.

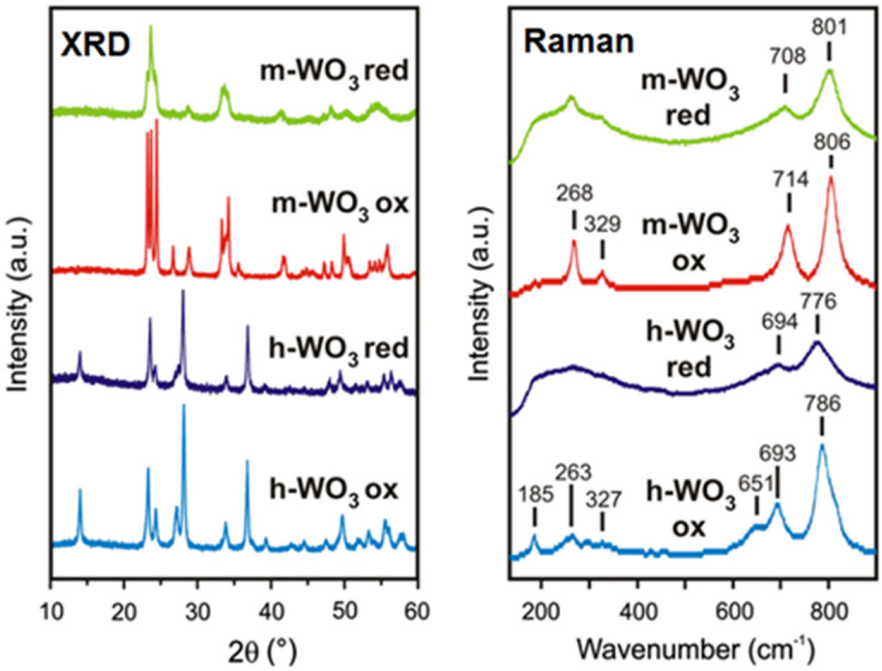

Figure 2. XRD and Raman spectra of monoclinic WO_3 (m-WO_3) and hexagonal WO_3 (h-WO_3) oxidized (air treatment) and reduced (N_2 treatment). Reprinted from Szilágyi et al. [20] with permission from Elsevier.

If the presence of ammonium ions allows h-WO_3 to be stabilized, it is also a key factor in controlling the shape of nanorod crystals [22]. NH_4^+ ions are preferably adsorbed on the (001) facets and block the crystal growing along this axis (Figure 3). Hexagonal nanowires

of WO_3 were also prepared as anodic materials of Li-ion batteries [23]. Hydrothermal treatment of lithium tungstate–lithium sulfate mixed solutions in HCl medium leads to typical nanowires, as shown in Figure 4.

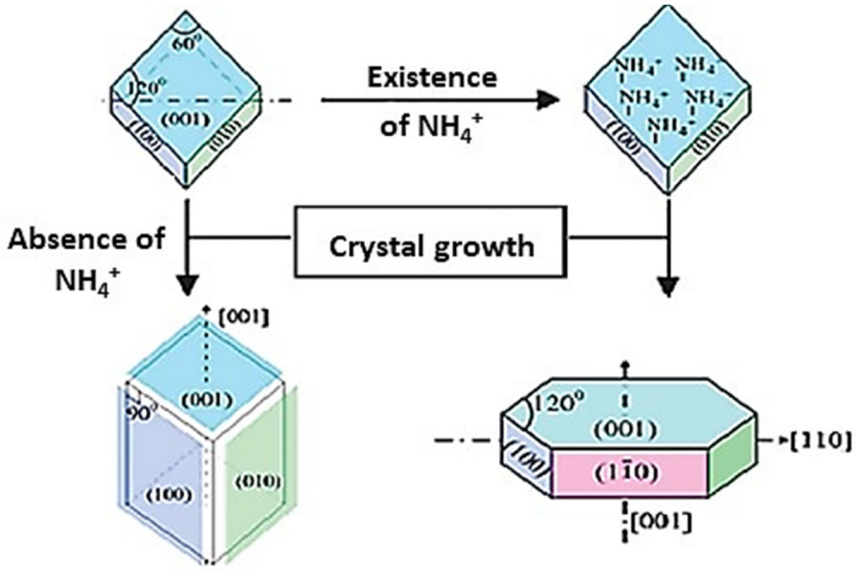

Figure 3. Effect of ammonium ions on the growth orientation of hexagonal single crystal of WO_3 nanorods (hydrothermal synthesis from ammonium tungstate). Reprinted from Zhu et al. [22] with permission from the Royal Society of Chemistry.

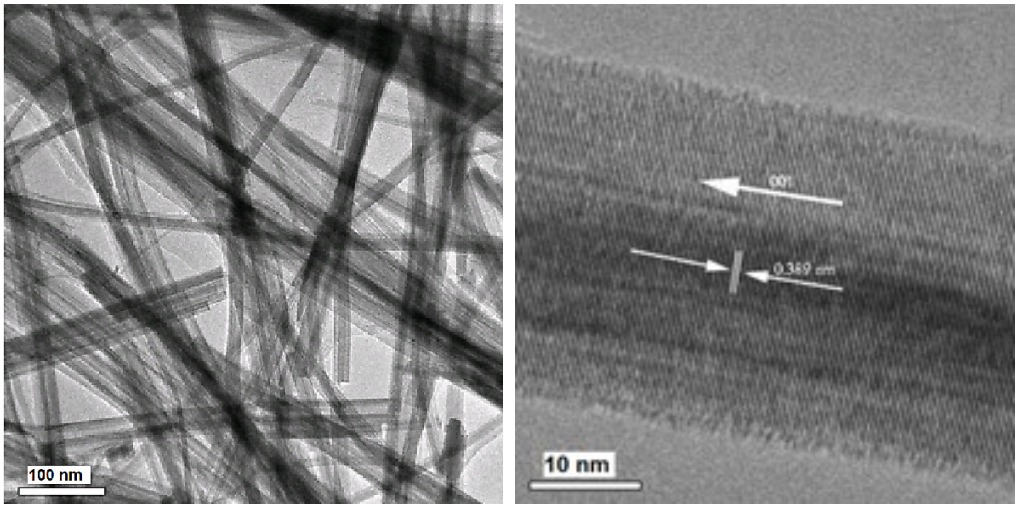

Figure 4. TEM image of h-WO_3 nanowires (left) and HRTEM image of an individual wire growing in the (001) direction. Reprinted from Gu et al. [23] with permission from Elsevier.

Crystal structures, phase transition and physical properties of nanostructured WO_3 oxides have been reviewed by Zheng et al. [24]. Numerous synthesis methods were reported for the preparation of films, ribbons, nanowires, nanotubes, nanorods, etc. In many cases, hexagonal WO_3 is observed in these nanostructures. For instance, leaflike nanoplatelets were prepared by dehydration of orthorhombic tungstite H_2WO_4 to monoclinic WO_3 [25].

2.1.2. Tungsten Trioxide $WO_{2.9}$ Blue Oxide (β-Tungsten Oxide $W_{20}O_{58}$) and Other Suboxides $WO_{3-\delta}$ ($\delta < 0.13$)

Tungsten suboxides phases with formulae W_nO_{3n-1} and W_nO_{3n-2} were first described by Magnéli in 1950 [26,27]. They were fully described by Tilley in 1995 [28]. The lattice (symmetry $P2/m$) consists of blocks of WO_6 octahedra joined by sharing corners (as in

m-WO_3) with certain octahedra sharing edges along a zig-zag dislocation line, as illustrated in Figure 5.

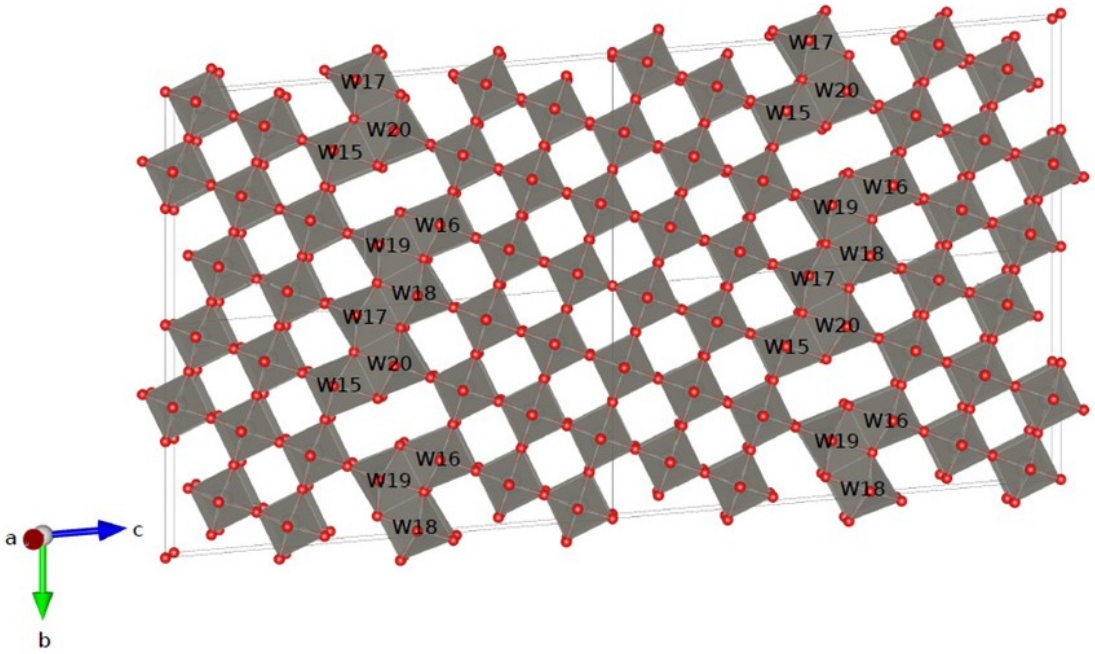

Figure 5. Structure of β-tungsten oxide $WO_{2.9}$, consisting of WO_6 blocks joined by sharing corners (ideal WO_3 oxide) or by sharing edges. WO_6 octahedra sharing edges create zig-zag distortion inside the structure. Tungsten atoms located along the zig-zag stripes are labeled. Reprinted from [29].

WO_{3-x} suboxides are formed when WO_3 is treated in H_2 or alcohol at moderate temperature (>400 °C). First, oxygen vacancies are created without a definite compound being formed [30]. β-Tungsten oxide is usually prepared by heating a mixture of WO_3 and tungsten powder at high temperature (~1000 °C), by reduction of WO_3 in hydrogen around 650 °C [1,27] or by reduction of ammonium paratungstate ($(NH_4)_{10}$ $H_2W_{12}O_{42}$, $4H_2O$) in hydrogen from 430 to 650 °C [31]. It should be noted that the color of ultrafine "WO_3" powders may change from yellow for the greatest particle sizes (>50 nm) to blue for the finest particles (<10 nm) [32]. In the meanwhile, the structure of ultrafine powders changes from triclinic (>50 nm) to cubic (<10 nm). A cubic phase of blue oxide nanosheets was synthetized by direct decomposition of $H_2WO_4 \cdot H_2O$ in H_2/N_2 [33]. The cubic phase is stable up to 280 °C and tends to form a monoclinic phase, complete at 410 °C. Structures similar to those shown in Figure 5 are described as crystallographic shear (CS) by Tilley [28]. By varying the number and orientation of WO_3 blocks sharing edges, it seems possible to reach $WO_{2.889}$ ($W_{18}O_{52}$) composition.

2.1.3. $WO_{2.72}$ Violet Oxide (γ-Tungsten Oxide $W_{18}O_{49}$) and Other Suboxides $WO_{3-\delta}$ ($\delta > 0.2$)

More complex structures are obtained when the O/W ratio decreases to less than 2.88. Solonin et al. described a suboxide $WO_{2.8}$ directly derived from hexagonal WO_3 [34]. They named it h-$WO_{2.8}$; it is formed at the initial stage of h-WO_3 reduction. Mesostructured $WO_{2.83}$ ($W_{24}O_{68}$) was recently prepared by Cheng et al. by using KIT6 silica as a hard template [35]. XRD confirmed the formation of monoclinic $WO_{2.83}$ (PDF # 36-0103). This result contrasts with the formation of $WO_{2.9}$ and $WO_{2.72}$ by reduction of bulk WO_3 (*vide infra*). Cheng et al. showed that the reduction of meso-WO_3 to meso-$WO_{2.83}$ occurred at low temperature due to a fast hydrogen diffusion through the mesoporosity (Figure 6).

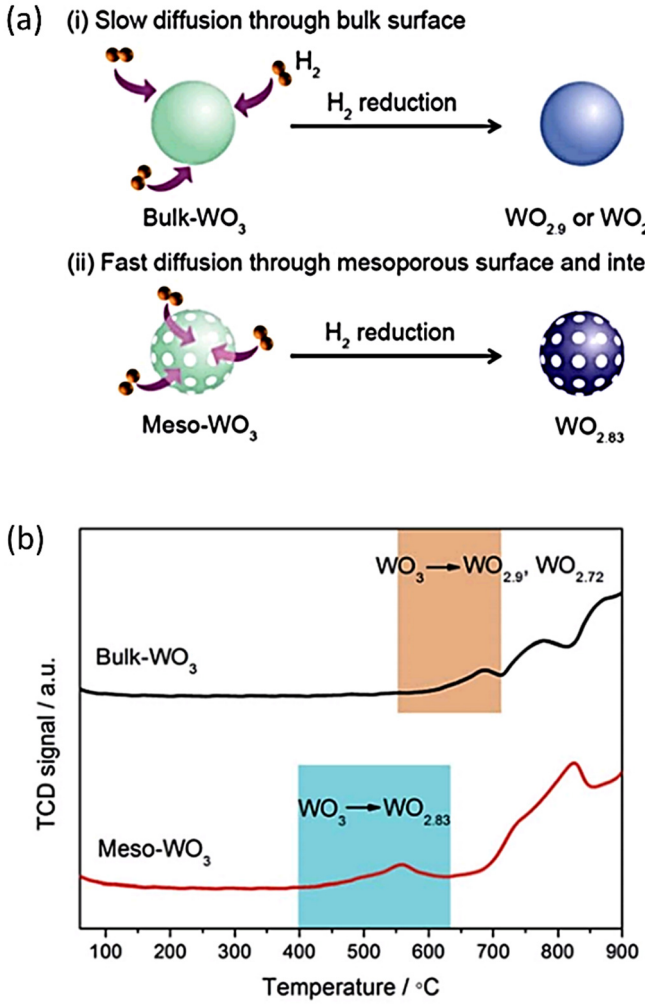

Figure 6. Compared reduction of bulk WO_3 and meso-WO_3 (**a**) and corresponding H_2-TPR profiles (**b**). From Cheng et al. [35] with permission from the Royal Society of Chemistry.

Violet oxide is generally formed by reduction of WO_3 in hydrogen at 900 °C in the presence of water vapor [1]. Sarin showed that $WO_{2.72}$ is the most stable oxide formed by reduction of WO_3 [36]. Intermediary blue oxide $WO_{2.90}$ is difficult to observe. As shown in Figure 7, violet oxide tends to form whiskers [37] or nanoneedles [38]. This 1D morphology seems to be characteristic of $WO_{2.72}$ oxide. While ultrasmall nanoparticles of WO_3 are not easily prepared, Soultanidis et al. succeeded in preparing 1.6 nm particles by thermal decomposition of ammonium metatungstate in oleyamine [39]. XRD revealed that these particles are mainly composed of the $W_{18}O_{49}$ phase (JCPDS 05-0392).

Interestingly, XPS analysis can be performed to assess the chemical composition of tungsten oxide nanopowders. The x value in WO_{3-x} can be determined by means of the ratio between W^{5+}4f and W^{6+}4f-states. For instance, three series of WO_{3-x} were synthesized by Shpak et al. at atmospheric pressure by electric explosion of wires (EEW) with different proportions between argon and oxygen [40]. In Figure 8, WO_{3-x}, $WO_{2.9}$ and $WO_{2.72}$ nanopowder compositions were determined using the W^{6+} response (comps. d-d, $W4f_{7/2}$ at 35.7 eV; comps. e-e, $W4f_{7/2}$ at 36.1 eV for hydroxide) and the W^{5+}-response (comps. c-c, $W4f_{7/2}$ at 34.8 eV).

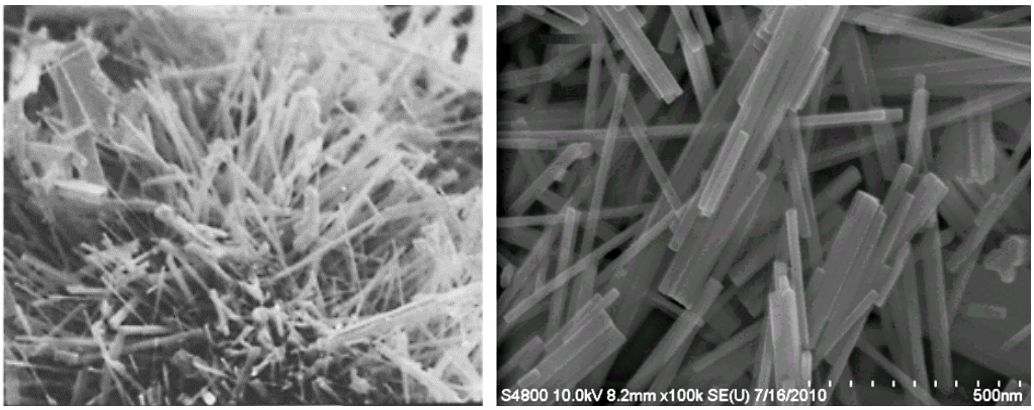

Figure 7. Morphology of violet oxide $WO_{2.72}$: random-plate-like whiskers prepared by Pfeifer et al. [37] (**left**, reprinted with permission from Elsevier); nanoneedles used by Wu [38] from commercial samples (**right**, reprinted with permission from Elsevier).

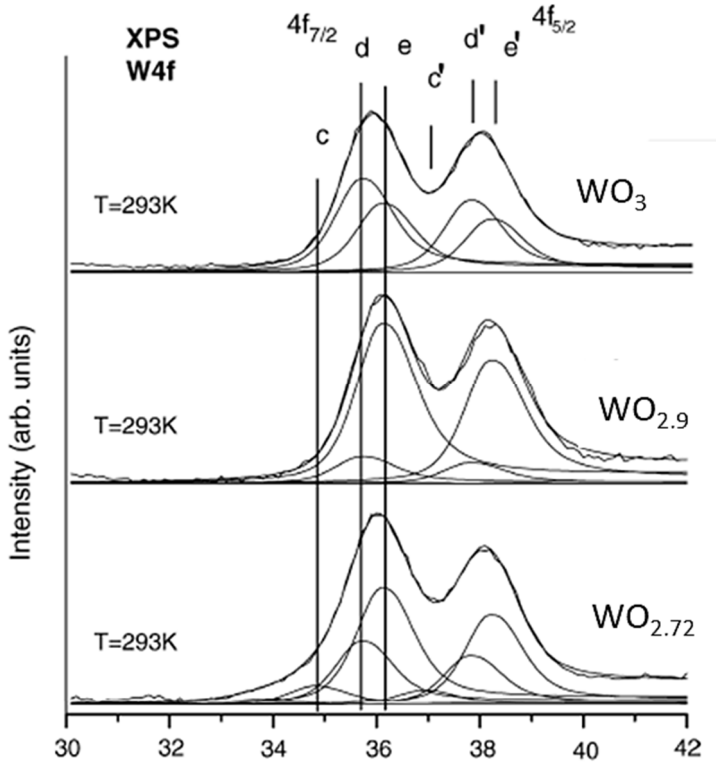

Figure 8. Peak synthesis for W4f-level XPS spectrum of tungsten atoms. The maxima of peak couples correspond to $W4f_{7/2}$ and $W4f_{5/2}$ levels of tungsten atoms for W^{5+} states of oxide (comps. c-c, $W4f_{7/2}$ at 34.8 eV) and W^{6+} states of oxide (comps. d-d $W4f_{7/2}$ at 35.7 eV) and hydroxide (comps. e-e, $W4f_{7/2}$ at 36.1 eV). From Shpak et al. [40], with permission from Elsevier.

2.1.4. Tungsten Dioxide (WO_2)

Tungsten dioxide is a rutile-like oxide, but contrary to TiO_2, WO_2 has a monoclinic structure with distorted octahedron of oxygen ions (C^5_{2h}, $P2_1/c$). This was confirmed by Ben-Dor and Shimony, who succeeded in preparing WO_2 monocrystals [41]. The monoclinic structure was later refined by powder neutron diffraction (PDF# 32–1393) [42]. An orthorhombic form of WO_2 was also reported (PDF# 82–728); it was evidenced in sonochemical preparation [43]. Most preparations of WO_2 were carried out by annealing of WO_3 at high temperatures (up to 1000 °C). A facile preparation at low temperature (500 °C) was reported by Coşkun and Koziol by hydrolysis of WCl_6 in the presence of $NaBH_4$ [44].

Compared to other tungsten oxides, WO_2 presents relatively high conductivity properties. The energy bands and density of states from theoretical calculations confirm a metal-like behavior of WO_2 [45].

2.2. Structure of Supported Tungsten Oxides

The structure of tungsten species dispersed on oxide supports depends on both the nature of support and the concentration of tungsten. In 2007, Knowles et al. reported a detailed overview of the surface chemistry of supported oxide, especially tungsten oxide [46]. WO_3 is more easily dispersed on alumina than on silica, on which WO_3 tends to form agglomerated crystallites [47]. The surface structure of tungsten oxide on various oxide supports (Al_2O_3, TiO_2, Nb_2O_5, ZrO_2, SiO_2 and MgO) was investigated by Raman spectroscopy by Kim et al. [48]. WO_3 on Al_2O_3, TiO_2, Nb_2O_5 and ZrO_2 exhibits strong bands at 1005–1020 cm^{-1} characteristic of terminal W=O mono-oxo species. Bands in the 800–960 cm^{-1} spectral region are also observed. They are attributed to W-O-W species whose intensity increases with the tungsten surface coverage. Bands at 1005–1020 cm^{-1} are not observed in Raman spectra of WO_3/SiO_2 and WO_3/MgO. Two intense bands at 802 and 715 cm^{-1} are visible on the spectra of 5%WO_3/SiO_2. These bands are characteristic of the formation of crystalline WO_3, due to the poor dispersion of WO_3 on this support. Raman spectra of WO_3/MgO are more complex and suggest the formation of crystalline $MgWO_4$ (as well as $CaWO_4$ due to Ca impurity in MgO). In situ Raman spectroscopy coupled to $^{18}O/^{16}O$ exchange allowed Lee and Wachs to precisely identify the surface structure of different oxides (including WO_3) dispersed on silica [49]. In this study, WO_3/SiO_2 showed Raman bands at 968-985-1014 cm^{-1} shifted to 920-935-963 cm^{-1} in totally ^{18}O-exchanged solids. Monoxo and dioxo tungstate species were formed, while crystallized WO_3 was virtually absent (contrary to the previous study). Decisive information on the structure of supported tungsten catalysts can be obtained by UV–Vis. Ross-Meedgarden and Wachs showed that the electronic edge energy (Eg) can be correlated to the nature of W surface species, especially the number of nearest cations surrounding the central M cation [50]. The number of covalent W-O-W bonds around the central W(VI) cation would be given by Equation (1):

$$N_{W\text{-}O\text{-}W} = 11.89 - 2.37Eg \quad (1)$$

with Eg varying from 5.5 eV for isolated WO_4 species (as bi-grafted, di-oxo WO_4 surface sites [51]) to 2.7 eV for crystallized WO_3 3D structures.

Though WO_3 tends to form nanocrystals on silica, there remains an amorphous fraction more or less dispersed. Chauvin et al. developed a methodology coupling XRD and Raman studies for the quantification of W species: surface dispersed WO_x (monomeric and oligomeric), amorphous WO_3 and crystallized WO_3 [52]. On silica, only dispersed W species (monomeric and polymeric) would be formed below 1 W nm^{-2}. For higher concentrations, WO_3 nanoparticles (amorphous and crystallized) are evidenced. This contrasts with other supports (Al_2O_3 [53,54], TiO_2 [55,56], ZrO_2 [57–59]) for which tungsten impregnation up to 4–5 W nm^{-2} leads to well-dispersed catalysts. On these supports, WO_3 nanocrystals are generally observed in the 4.5–9 W nm^{-2} loading range, while large bulklike WO_3 crystals can be observed beyond 9 W nm^{-2} [60]. In the last decades, the WO_3-ZrO_2 catalytic system has been the subject of a huge number of investigations owing to its excellent performances in reactions requiring strong acid sites [61,62]. Recent investigations by HAADF [63] and HRTEM [64] allowed obtaining detailed pictures of the various tungsten species populating the zirconia surface (Figure 9a,b).

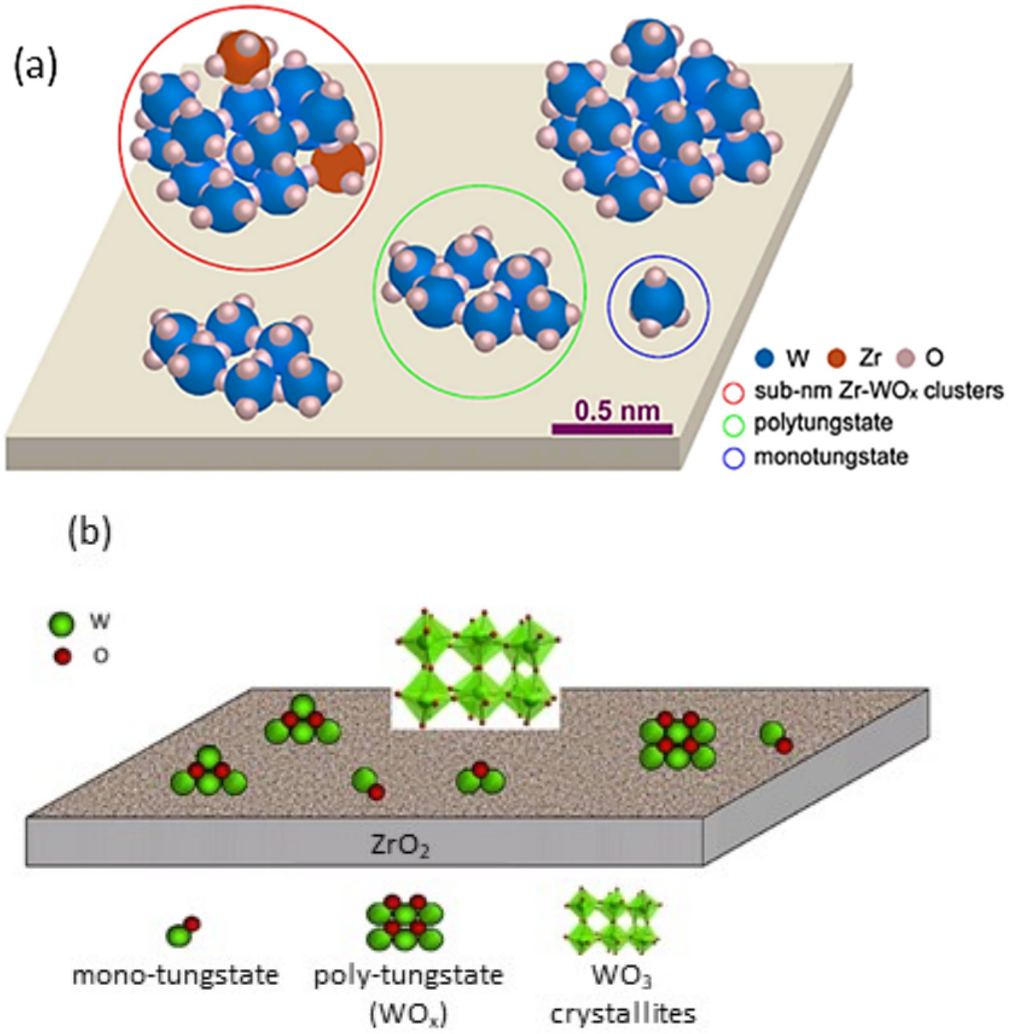

Figure 9. Models of tungsten surface species evidenced (**a**) by STEM and HAADF (Zhou et al. [63], reprinted with permission from Elsevier) and (**b**) by HRTEM (De Angel et al. [64], reprinted with permission from Elsevier).

It should be noted that WO_3 clusters (crystallized or not) may contain Zr atoms from the support (Figure 9a). Tungstate species depicted in Figure 9 are in agreement with the model of growth mode of W species when the surface density exceeds 5 W nm^{-2} [65]. Preparation of tunsgtated zirconia catalysts from Lindqvist-type complexes containing $(W_5O_{18}Zr)^{2-}$ moieties confirmed the structure of such surface species containing both W and Zr atoms, as well as their role in acid catalysis [66]. Structures of oxo-W(VI) species deposited on TiO_2 solids were extensively studied by Tribalis et al. by Raman spectroscopy [56]. Molecular configuration of W surface species depends on the temperature of calcination in O_2. Raman features shifted from 930 cm^{-1} ($Ti_2OH\cdots OWO_3$, main species at 25 °C) to 950 cm^{-1} (Ti-O-WO_3 at 100 °C), then 970 cm^{-1} ($(Ti\text{-}O)_2\text{-}W(=O)_2$ at 120–250 °C) and finally 1030 cm^{-1} for the trisubstituted mono-oxo $(Ti\text{-}O)_3$-W=O at 430 °C.

Though W dispersion is not easily obtained on amorphous silica, recent developments of mesostructured silicas (MCM 41 [67,68], KIT-5 and KIT-6 [69,70], SBA-15 and SBA-16 [71–73]) has allowed inserting significant amounts of tungsten while limiting the formation of WO_3 nanocrystals. This technique has been extended to spongelike silicate TUD-1 discovered at Delft University [74]. Isolated WO_4^{2-} species could be anchored on Ti-modified TUD-1 up to 30% WO_3 [75]. Other techniques including aerosol-assisted sol–gel processes [76] or grafting of tungsten-containing molecules on silica [77,78] were also developed to obtain highly dispersed "single-site" W species.

As a final statement, critical insights of tungsten-based materials reveal no less than seven tungsten–oxygen systems, with three arrangements mainly encountered in the catalysis field: WO_3, $WO_{2.9}$ (β-tungsten oxide) and $WO_{2.72}$ (γ-tungsten oxide). WO_3 presents several allotropic forms: monoclinic, triclinic and hexagonal structure. The structure impacts the photocatalysis activity since the electron–hole recombination is favored by the absence of defects. Tungsten suboxide phase ($WO_{2.9}$) is formed under H_2 treatment and exhibits oxygen vacancies. More complex structures are obtained when the O/W ratio decreases to less than 2.88, and $WO_{2.72}$ is the most stable oxide formed by reduction of WO_3.

3. Acidity of Supported Tungsten Oxide Catalysts

Tungsten oxide WO_3 is among the most acidic transition metal oxides [79]. Very few studies have been devoted to the acid properties of unsupported tungsten oxides. Kanan et al. studied the change of acid site concentration upon dehydroxylation/dehydration of the surface of monoclinic WO_3 [80]. They concluded that the changes in Brønsted/Lewis (B/L) acid site concentration were not related to the degree of dehydroxylation but rather to a mild reduction of the tungsten oxide surface. Choi et al. investigated surface acidity of mesoporous WO_3 synthesized using KIT-6 as a hard template [81]. Acid site characterization (NH_3-TPD, FTIR of adsorbed pyridine) showed that mesoporous WO_3 exposes predominantly Lewis acid sites associated with W^{6+} and probably cus-W^{6+} (cus = coordinatively unsaturated sites). A similar study performed by Kasian et al. showed that acid site concentration of mesoporous tungsten oxide was increased by a mild reductive treatment in hydrogen at 250 °C [82]. Yue et al. studied the reactivity of m-WO_3, h-WO_3, hexagonal tungsten bronze (HATB) and $(NH_4)_{0.33-x}WO_{3-z}$ for the hydroconversion of *n*-heptane reaction (Pd was added to the W oxides as hydrogenation function) [83]. The tungsten oxides were reduced in H_2 at 440 °C, 35 bar. The *n*-C7 reactivity revealed the formation of strong Brønsted acid sites, certainly linked to the reduction of W^{6+} to lower valence states, the protons allowing the neutralization of negative charges localized on W-O-W formed with $W^{(6-x)+}$ ions. Li et al. investigated the behavior of MoO_3 or WO_3 clusters in the conversion of labeled ethanol (CH_2CH_3OD) [84]. Dehydration and dehydrogenation can occur. The overall alcohol conversion would be correlated to Lewis acidity, while the selectivity (dehydration vs. dehydrogenation) would reflect the redox properties of the oxide (i.e., the propensity of Mo or W to reduce from VI to V state in the reaction medium). The reaction was carried out with $(MO_3)_3$ trimers supported on graphene. Other supports and other reactions were tested with contrasted differences between Mo and W oxides depending on the substrate (see the review [85]).

3.1. General Overview

Barton et al. reported that supported tungsten oxide catalysts are able to generate Brønsted acid sites when W^{6+} species are replaced by tungsten cations with lower valency [86]. A general overview of the acidity of tungstated oxides was performed by Zaki et al., who compared the relative strength of acid sites of 10% WO_3 samples deposited on Al_2O_3 (69 $m^2\ g^{-1}$), TiO_2 (34 $m^2\ g^{-1}$) and SiO_2 (136 $m^2\ g^{-1}$) [87]. All samples were calcined at 500 °C. Well-dispersed monotungstates and polytungstates were the most abundant surface species on WO_3/Al_2O_3, while 3D polytungstates were observed on WO_3/TiO_2. On WO_3/SiO_2, tungstosilicates and crystallized WO_3 would be the dominant surface structures. Acid sites were monitored by pyridine adsorption, which can lead to four species: LPy (Lewis acid bound Py), BPy (Brønsted acid bound Py), HPy (hydrogen-bonded Py) and PPy (physically adsorbed Py). FTIR spectra of adsorbed pyridine were recorded at room temperature (Figure 10) and after desorption at 100, 200 and 300 °C.

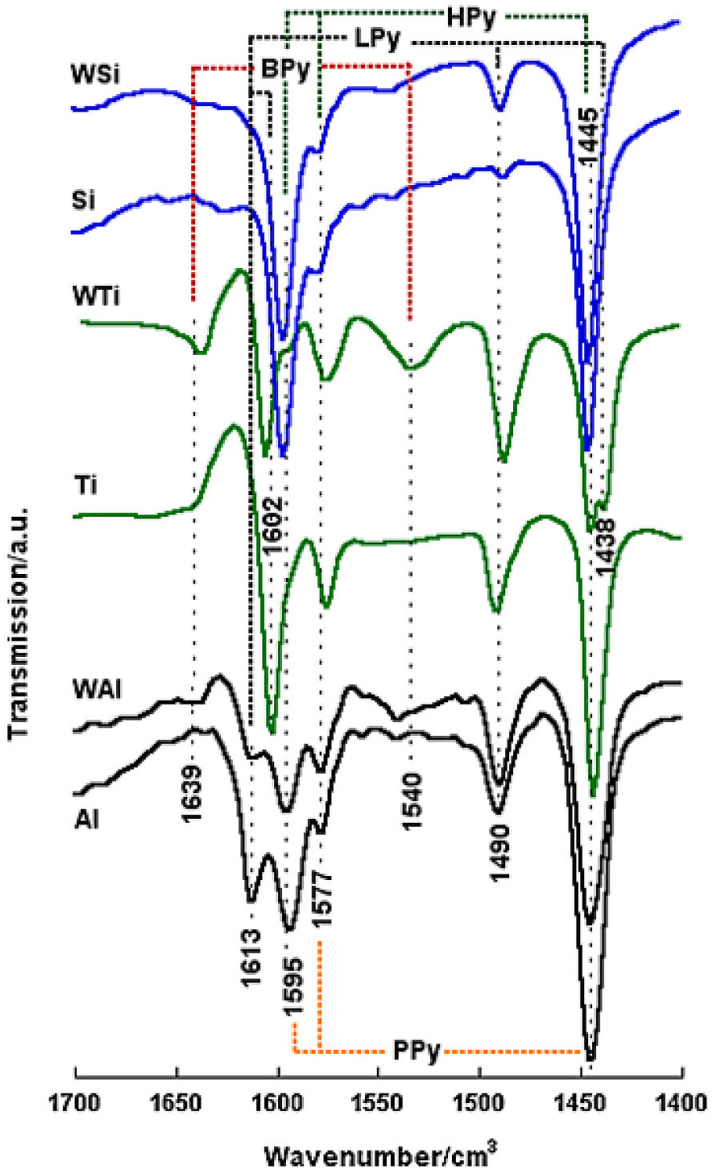

Figure 10. FTIR spectra of adsorbed pyridine at room temperature on Al_2O_3 (Al), TiO_2 (Ti), SiO_2 (Si) and 10%WO_3 on these supports (code: WAl, WTi and WSi, respectively). From Zaki et al. [87] with permission from Elsevier.

Hydrogen-bonded pyridine is the main species at RT on WO_3/SiO_2, but it is unstable and tends to disappear upon heating. Lewis acid sites (LPy) and hydrogen-bonded pyridine (HPy) are clearly observed on WO_3/Al_2O_3, while both BPy and LPy sites are identified on WO_3/TiO_2. Brønsted sites would be very strong on WO_3/TiO_2 (still intense upon heating at 300 °C). The work of Zaki et al. [87] clearly underlines the critical role of the support of tungsten oxides, both in the nature of W species and in their respective acidity.

3.2. Silica-Supported Tungsten Oxides

Due to the quasiabsence of acid sites on silica [88], WO_3/SiO_2 materials were often used to investigate the acidity of tungsten oxides. In their study on WO_3/SiO_2 catalysts (0 to 11.7 wt.% W on a silica of 200 $m^2\ g^{-1}$, i.e., 0 to 2.4 W nm^{-2}), Chauvin et al. monitored the acidity of the samples by FTIR spectroscopy of adsorbed 2,6-dimethylpyridine (lutidine) [52]. The spectra reported in Figure 11a show the presence of Brønsted sites (bands at 1643 and 1630 cm^{-1}). Lewis sites that should give bands at 1620–1600 cm^{-1} are clearly

absent from the samples. Amounts of Brønsted sites linearly increase with the WO_3 surface density up to 1.5 W nm^{-2} (Figure 11b).

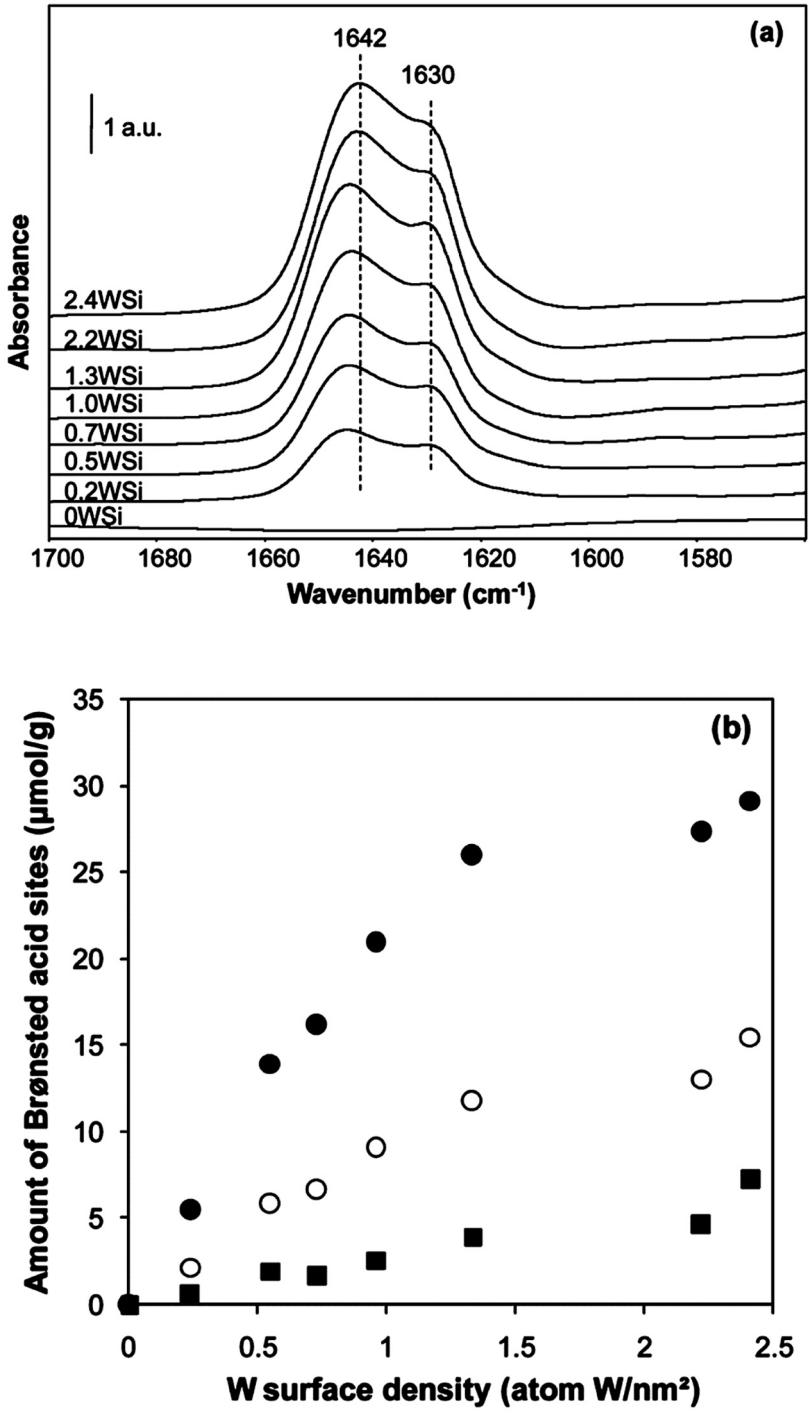

Figure 11. (**a**) FTIR spectra following lutidine adsorption and evacuation at 150 °C over WO_3/SiO_2 of various W surface densities; (**b**) amounts of B sites measured after lutidine evacuation at 150 °C (black circles), 200 °C (open circles) and 250 °C (black squares). From Chauvin et al. [52] with permission from the American Chemical Society.

The acidity of WO_3/SBA-15 oxides was characterized by Hu et al. using pyridine adsorption, solid-state NMR and quantum chemistry calculation [89]. The study was completed by measurements and calculations of ^{15}N NMR chemical shift tensors of pyridine interacting with tungsten oxides and silica. It was shown that W-OH-W dimers are the

principal Brønsted acid sites. W-OH monomers and silanols are very stable with minimal Brønsted acidity. Contrasting with the work of Hue, Gonzalez et al. found quasiexclusively Lewis acid sites in a series of WO_3/SBA-15 materials [90]. Acidity was characterized by pyridine adsorption monitored by FTIR. Bands at 1595 and 1445 cm^{-1} attributed to pyridine coordinated to Lewis acid sites are much more intense than the 1545 cm^{-1} band characteristic of protonated pyridine bound to Brønsted acid sites. However, even though it is relatively weak, the Brønsted site density seems very stable when the temperature of pyridine adsorption is increased from 50 to 100 °C, while the number of Lewis sites is strongly affected (Table 1).

Table 1. Acid site density on SBA-15 and WO_3/SBA-15 measured by pyridine adsorption at 50 and 100 °C. The number of sites is calculated from the integrated area of the band at 1545 cm^{-1} for Brønsted sites and at 1445 cm^{-1} for Lewis sites. From González et al. [90].

Sample	T (°C)	Brønsted Acid Sites	Lewis Acid Sites
		(μmol g^{-1})	(μmol g^{-1})
SBA-15	50 °C	0	152
	100 °C	0	67
5%WO_3/SBA-15	50 °C	24	920
	100 °C	24	92
15%WO_3/SBA-15	50 °C	34	1102
	100 °C	31	350
25%WO_3/SBA-15	50 °C	15	1246
	100 °C	12	458

The reasons for the discrepancy between the work of Hu et al. [89] and that of González et al. [90] are not clear. They may originate from the nature of the tungsten precursor (WCl_6 in toluene for Hu et al. and ammonium metatungstate for González et al.), the final temperature of calcination (400 °C for Hu et al. and of 600 °C for González et al.) or the method of acid site detection (NMR for Hu et al. and FTIR for González et al.). This question should certainly be reconsidered in the future.

WO_3/SiO_2 catalysts were prepared by Kulal et al. for liquid phase nitration of aromatics [91]. A sol–gel technique using ammonium metatungstate and ethyl silicate 40 was employed for the preparation. FTIR of adsorbed pyridine revealed the presence of both Lewis and Brønsted sites. Kulal et al. attributed the formation of Brønsted sites to the presence of polytungstate species, while Lewis sites would require rather isolated W ion centers. The B/L ratio increased with the W loading in the catalysts. At low loading (<5% W), there were virtually no Brønsted sites. Bhaumik et al. developed silica-supported WO_3 and Ga_2O_3 catalysts for lignocellulosic biomass to furfural processes [92]. Although the acidity was not characterized in detail, the authors of this work stated that Lewis sites are the most abundant acid sites on the catalysts.

Tungsten species are generally added by impregnation on the silica support. They may also be incorporated during the preparation of the mesoporous silica. Zhu et al. prepared WZr-KIT6 with various Zr/W ratios by addition of pluronic triblock copolymer to a mixture of tetraethoxysilane (TEOS), ammonium tungstate and $ZrOCl_2$ [93]. Acidity of the materials was measured by adsorption of pyridine monitored by NMR. Both Brønsted and Lewis acid sites coexisted on the catalysts. Lewis acid sites would be mainly linked to the presence of zirconium while tungsten is necessary to generate strong Brønsted acid sites. The materials were tested in ethanol dehydration. Interestingly, it was shown that calcination of the coke catalysts regenerated Brønsted sites, which became even stronger than those on the fresh materials.

Attempts to modify the activity of WO_3/SiO_2 catalysts by means of gold nanoclusters revealed that the acidity of tungsten oxide is not modified by Au (methanol transformation tests) [94]. WO_3/SiO_2 is highly selective for dimethyl ether, while the presence of gold

is necessary for the formation of methyl formate and dimethoxymethane. This result suggests that pure WO_3 possesses only acid sites and virtually no redox sites. The addition of WO_3 was recently used to give acidity to Pt/SiO_2 for glycerol hydrogenolysis to 1,3-propanediol [95]. Tungsten oxide would be present as $W_{25}O_{73}$ with a high proportion of W^{5+}. It also maintains a high dispersion of platinum.

3.3. Alumina-Supported Tungsten Oxides

Acidity of WO_3/Al_2O_3 was studied in the 1980s and 1990s by Soled et al. [96] and Zhang et al. [97]. While alumina possesses virtually no (or very weak) Brønsted sites, the addition of tungsten oxide generates both Brønsted and Lewis sites. Most probably, WO_3 titrates the strongest Lewis sites on alumina to form Brønsted sites. The number and strength of these Brønsted sites increase with the temperature of calcination [96]. The proportion of Brønsted sites also increases with the tungsten loading (Table 2).

Table 2. Effect of W loading on the number of Lewis and Brønsted sites of WO_3/Al_2O_3 (152 m^2 g^{-1}). Acid site distribution was determined by a modified Benesi colorimetric technique. From Zhang et al. [97].

WO3 Loading (wt.%)	Lewis Sites (μmol g^{-1})	Brønsted Sites (μmol g^{-1})	Lewis Sites (%)	Brønsted Sites (%)
0	190	14	93	7
2.5	207	69	75	25
10	220	125	64	36
30	242	182	57	43

Combining lutidine adsorption and other spectroscopic investigation, Chen et al. obtained precise information about the change in acid site concentration with respect to the W surface density [54]. Their results are summarized in Figure 12, which shows that monomeric tungsten species contain quasiexclusively Lewis acid sites, while Brønsted sites are relatively abundant on polymeric species appearing for W density above 1.4 W nm^{-2}.

The acid properties of WO_3-Al_2O_3 catalysts were recently revisited by Kitano et al., who showed that the formation of Brønsted sites depended on the temperature of calcination [98]. They proposed that Brønsted sites are predominantly located at the boundaries between WO_3 monolayer domains (Figure 13).

Potassium-doped WO_3/Al_2O_3 catalysts are able to transform gas mixtures such as $CO_2/H_2S/H_2$, methanol/H_2S or $CH_4/H_2S/CO_2$ into valuable products such as methyl mercaptan (CH_3SH) [99–101]. All these reactions were reviewed by Taifan and Baltrusaitis [102]. Structural and acid–base properties of K_2O-WO_3-Al_2O_3 catalysts were recently investigated by Wang et al. [103], Zhu et al. [104] and Kiani et al. [105]. Raman spectroscopy was used to differentiate and detect crystalline WO_3 (bands at 273, 719 and 809 cm^{-1}), crystalline K_2WO_4 (bands at 324 and 927 cm^{-1}) and dispersed surface oligomeric WO_x species on alumina (strong band at 1021 cm^{-1}). Conformation and position of most of these Raman bands were confirmed by DFT calculation [105]. Surface acidity was probed by NH_3-TPD [103] or NH_3 adsorption monitored by FTIR [104], while basicity was probed by CO_2-TPD. K_2O suppressed both Brønsted and Lewis acidity from the surface WO_x species or exposed Al_2O_3 sites [104]. Adsorption of CO_2, nil on unpromoted WO_3/Al_2O_3 (no basic sites), significantly increases on K_2O-promoted catalysts. Residual acidity could play a major role in catalytic activity, while basicity would be essential for a good selectivity for methyl mercaptan [103].

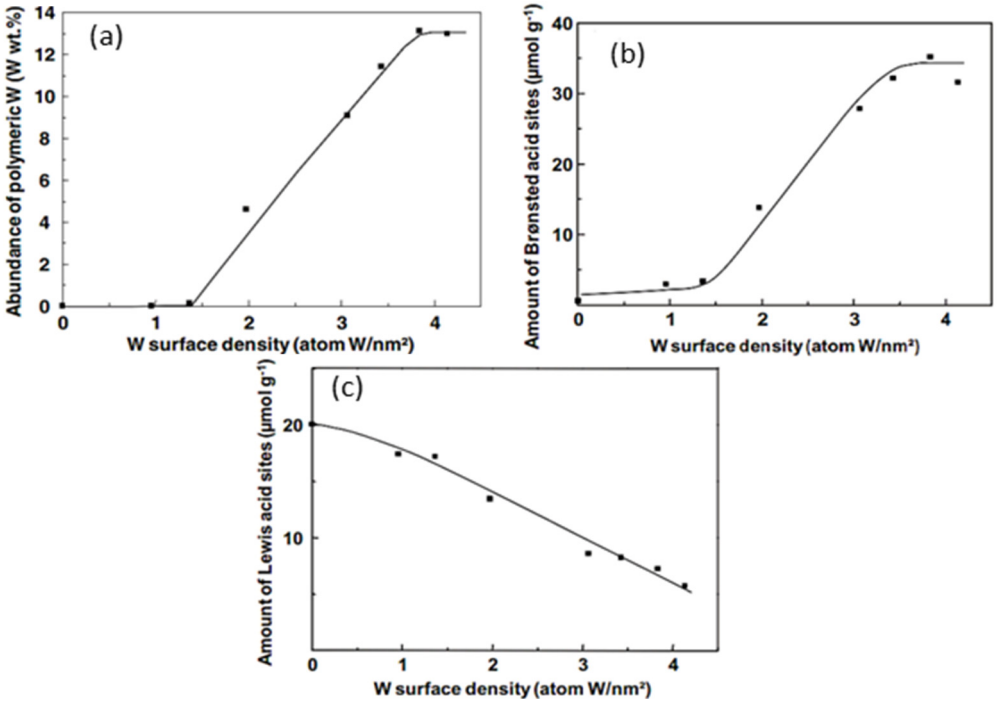

Figure 12. Correlation between amounts of (**a**) polymeric species, (**b**) Brønsted acid sites and (**c**) Lewis acid sites and the tungsten density on WO_x/Al_2O_3 catalysts. Amounts of polymeric species were deduced from the integration of the Raman band at 1022 cm^{-1}. B and L concentrations were deduced from lutidine adsorption (FTIR). From Chen et al. [54] with permission from Elsevier.

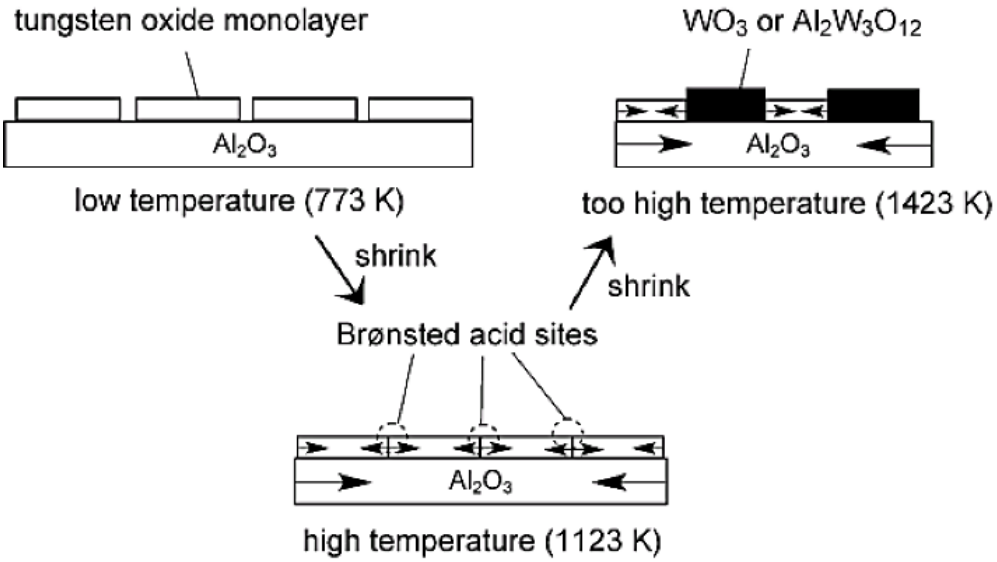

Figure 13. Effect of the temperature of calcination on the formation of Brønsted acid sites at the junction between WO_x monolayer and alumina. From Kitano et al. [98] with permission from John Wiley and Sons.

3.4. Zirconia-Supported Tungsten Oxides

The system WO_3-ZrO_2 was earlier reported to possess strong acid sites with $H_0 < -14.7$ [106]. This "super" acidity makes the catalyst able to replace concentrated sulfuric acid for alkylation and isomerization reactions of alkanes [62,106] or aromatics [61,107]. Acidic sites certainly play a great role in these reactions, even though redox properties of WO_3-ZrO_2 can be put forward for explaining the enhanced activity of reduced materi-

als [108]. The effect of the preparation method on the acidity of WO_3-ZrO_2 was studied by Santiesteban et al. [109]. Acid sites were titrated by adsorption of 2,6-dimethyl pyridine. Brønsted sites (0.054 meq g^{-1}) were more abundant than Lewis sites (0.013 meq g^{-1}), but only 20% of Brønsted sites were strong acid sites (0.011 meq g^{-1}) in proportion close to Lewis sites. The most efficient preparation consists of reflux/impregnation of $ZrO(OH)_2$ and H_2O with ammonium metatungstate. The acid site structure (Scheme 1) is similar to the model proposed by Afanasiev et al. in 1994 [110].

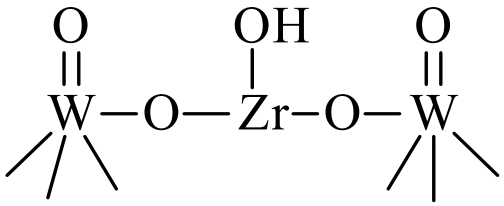

Scheme 1. Acid site model of WO_3-ZrO_2 with Lewis site born by tungsten oxo species and Brønsted site on zirconium in the vicinity of tungsten atoms. Adapted from Santiesteban et al. [109] and Afanasiev et al. [110].

Brønsted/Lewis (B/L) site ratio in WO_3-ZrO_2 catalysts was measured by Baertsch et al. for various tungsten loadings and in various conditions of pretreatment [111]. Acid sites were evaluated by adsorption/desorption of NH_3 or pyridine. Complementary information about the redox sites was obtained by adsorption of O_2 and H_2, while the number of hydroxyl groups was measured by D_2/OH isotopic exchange. Brønsted sites were virtually absent on low-loaded catalysts where tungsten was in the form of monomeric species. The B/L ratio gradually increased with the tungsten loading. The presence of H_2 during NH_3 adsorption led to the generation of strong Brønsted sites. Platinum nanoparticles used in bifunctional Pt/WO_3-ZrO_2 catalysts would also be a source of Brønsted site by H spillover between Pt and WO_3 [112]. The surface chemistry and acidity of WO_3-ZrO_2 catalysts for skeletal isomerization of alkanes were discussed by Di Gregorio and Keller, who suggested that a condensation phenomenon between Lewis and Brønsted sites can occur during the calcination treatment [113] (Figure 14).

A combined theoretical–experimental study on the acidity of tungstated zirconia was performed by Galano et al. [114]. They confirmed that the Lewis acidity (band at 1444 cm^{-1} for pyridine coordinated to L sites) and Brønsted acidity (band at 1539 cm^{-1} for protonated pyridine) is a function of the degree of WO_3 polymerization. The number of Brønsted sites increased while that of Lewis sites decreased as the W centers shifted from tetrahedral to octahedral coordination, i.e., when the degree of WO_x condensation increased. In parallel, the strength of the Brønsted acid sites tended to decrease. A maximum of Brønsted acidity was observed for a W loading of 7 W nm^{-2}. Recent investigations of tungstated zirconia designed for acid-driven catalytic reactions showed that active sites are three-dimensional distorted Zr-WO_x clusters of 0.8−1 nm size [59]. Optimum structure for a better activity is obtained when W is in a distorted octahedral environment in close contact with Zr cations. Calcination temperature (up to 800 °C) and nature of zirconium oxyhydroxide used as support play a major role in obtaining higher Brønsted acidity [115]. Though acid properties are generally characterized by adsorption of basic molecules (e.g., NH_3, pyridine) monitored by FTIR, other techniques are available. Li et al. showed that ^{31}P-NMR using TMPO (trimethyl phosphine oxide) as a probe molecule reveals the presence of Brønsted sites on WO_3-ZrO_2 prepared by a sol–gel method with $Zr(OBu)_4$ and WCl_6 as reagents [107]. TMPO gives a broad band from 40 to 90 ppm, while chemical shift above 57 ppm is characteristic of Brønsted sites.

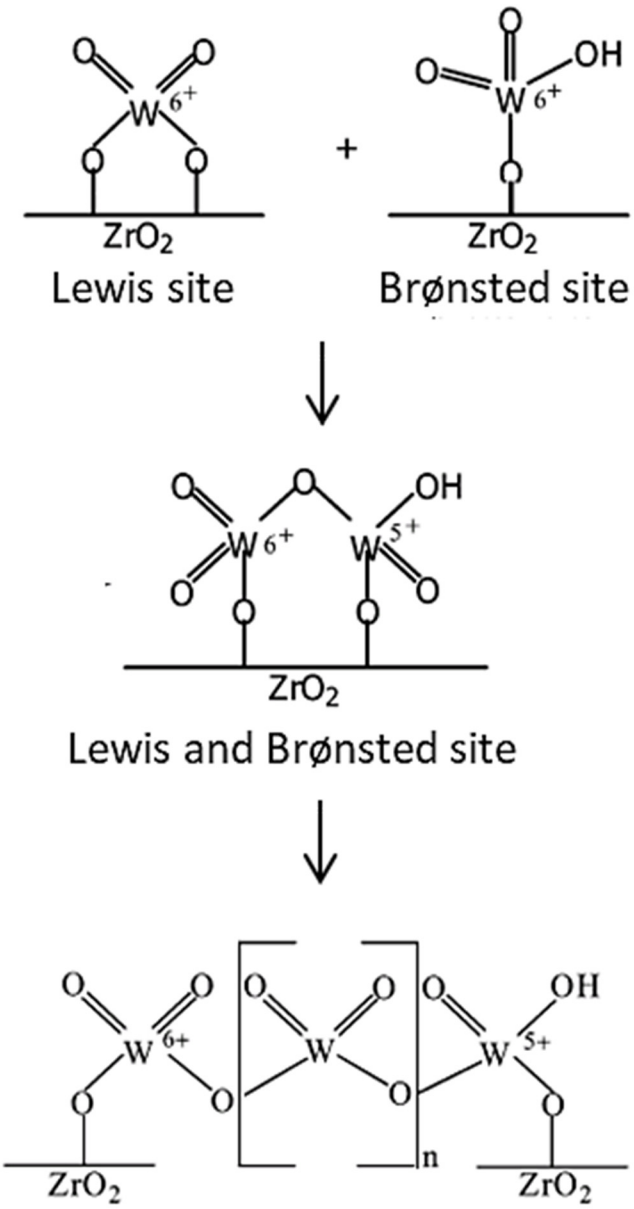

Figure 14. Condensation of Lewis and Brønsted sites to form new surface tungstate species on WO_3/ZrO_2 catalysts. Adapted from [113] with permission from Elsevier.

Yttrium doping of zirconia is often used to stabilize the tetragonal structure of ZrO_2. The effect of yttrium on the generation of acid sites on WO_3-ZrO_2 was investigated by Yamamoto et al. [116]. Acidity of the catalysts (15% WO_3) was characterized by means of model reactions: *n*-butane skeletal isomerization, alkylation of anisole with benzyl alcohol, and 2-butanol decomposition. Acidity increased with yttrium content up to 4% Y. In the meanwhile, the tetragonal-to-monoclinic ratio of zirconia increased to reach 85% of tetragonal phase for 4% Y. This proves that *t*-ZrO_2 is more suitable than *m*-ZrO_2 for stabilizing WO_x species with the highest acidity. Above 4% Y, the catalyst acidity decreased due to the excessive formation of inactive Y-W-O species. The beneficial role of tetragonal zirconia was demonstrated for different applications of WO_3-ZrO_2 catalysts, such as hydrolysis of cellobiose [117] or viscoreduction of heavy crude oil [118]. The mode of preparation of the zirconia support can greatly affect the acidity of the materials. Sol–gel synthesis and extraction of the solvent in supercritical conditions give the most active catalysts for organic reactions of industrial interest: acylation of veratrole with acetic anhydride and acylation of anisole with benzoic anhydride [119]. Doping zirconia

with phosphorus was extensively studied by Miao et al. [120,121]. WO_3 was deposited on mesoporous zirconium oxophosphate [120] or directly incorporated in the one-pot preparation of meso-ZrPOx to synthesize mesoporous WZrP materials [121]. The catalysts were tested in benzylation of anisole. Unfortunately, the effect of phosphorus could not be clearly established due to the absence of reference WO_3/ZrO_3 catalyst in these studies. However, the mode of preparation and the mesoporous texture give the WZrP materials a high activity and a high stability. The nature of acid sites is similar to the acidity spectrum characterized in WO_3/ZrO_2: W-free materials possess Lewis sites (83 μmol g^{-1}) and very few Brønsted sites (19 μmol g^{-1}). Brønsted site density increases up to 55 μmol g^{-1} for W/Zr ratio of 0.2.

3.5. Titania-Supported Tungsten Oxides

WO_3-TiO_2 is also an acid catalyst with activity for *n*-alkane isomerization [55]. These mixed oxides possess both Lewis sites ascribed to surface Ti^{4+} species and strong Brønsted sites generated by WO_3 nanoclusters. WO_3-TiO_2 was proven to have excellent performances in the reaction of sorbitol transformation into biofuels [122]. The reaction proceeds via successive steps of dehydration and hydrogenation, which requires metal–acid bifunctional catalysts. WO_3-TiO_2 (acid function) associated with Pt/ZrO_2 (metallic function) gave the best performance for the production of C5-C6 hydrocarbons. The main application of WO_3-TiO_2 (associated with V_2O_5) is for the NO_x abatement by the NH_3-SCR process [123–125]. While the chemical state of vanadium and tungsten seems to be crucial for a good $DeNO_x$ activity [126], acid properties could also play a primary role in the reaction [123,127]. The characterization of V_2O_5-WO_3/TiO_2 is examined in Section 4.

3.6. Conclusions

Evaluation of the acidity of supported WO_x obviously depends on the used probe molecule because of its own basic strength. For instance, NH_3, lutidine and pyridine, the most popular probe molecules for acidity evaluation, display pKa values of 9.23, 6.65 and 5.23, respectively. Consequently, they do not all exhibit the same sensibility toward the Brønsted (or acidic hydroxyl group) and Lewis acid sites (coordinatively unsaturated sites).

In addition, the acidity of WO_x species clearly depends on the W surface coverage. Indeed, dispersed phase surface sites (WO_4, WO_5), poorly crystalline WO_3 nanoparticles and bulklike crystalline WO_3 all show unique acidity. For instance, crystalline WO_3 exhibits Brønsted acidity, not encountered on dispersed WO_4 sites. Consequently, the acidity of catalysts strongly depends on the obtained WO_x surface species, which depend on the preparation protocol and the tungsten loading. Brønsted acid sites are reported to be mostly dependent on the presence of polytungstate polymeric species. Lewis acid sites are associated with coordinatively unsaturated W^{6+} sites or isolated W ions centers. The B/L ratio depends on the support. Lewis sites are the most abundant acid sites on WO_3/SiO_2 catalysts. Addition of tungsten oxide on alumina generates both Brønsted and Lewis sites, and the proportion of Brønsted sites increases with the tungsten loading. The stronger acid sites are encountered on the WO_3-ZrO_2 system, where a condensation phenomenon between Lewis and Brønsted sites can occur during the calcination treatment. New surface tungstate species appear with various degrees of WO_3 polymerization, leading to octahedral coordination that promotes an increase in the amount of Brønsted acid sites.

4. WO_3 Catalysts for $DeNO_x$ Applications: WO_3-V_2O_5/TiO_2 and Other Tungsten-Based Materials

Nitric oxide abatement in nitric acid plants was initially carried out by NH_3-SCR over V_2O_5-TiO_2 catalysts. Very soon, it was proven that adding WO_3 (or MoO_3) to the catalyst formulation led to a dramatic improvement of the performance. These V-W/TiO_2 catalysts were also implemented in $DeNO_x$ autocatalyst processes, especially for heavy-duty engines, working with NO_2/NO_x inlet ratio of 0 or 0.5, related to the standard and fast SCR stoichiometry, respectively. The role of WO_3 was summarized by Chen and Yang in 1992 [123]: (i) it increases the activity and widens the temperature window; (ii) it increases

the resistance to various poisons (alkalis, arsenic); (iii) it reduces ammonia oxidation by O_2, which is a nondesired reaction (especially possible at elevated temperature, T > 400 °C). Kompio et al. also showed by different techniques (e.g., Raman spectroscopy, EPR, H_2-TPR) that tungsten allowed an increase in V-O-V species by confining vanadia in small clusters [128]. Most of these effects were confirmed and detailed in a recent review by Lai and Wachs [129], who stressed three important features of the reaction: (i) the role of V^{5+} surface species as active sites: WO_3 is not active *per se* but promotes the reaction by vanadia by formation of oligomeric vanadia (V_2O_5) sites or crowding; (ii) the specific role of Brønsted acid sites in NH_3 activation: most of the Lewis sites are converted to Brønsted sites in the presence of moisture at 250 °C; (iii) the detailed mechanisms reported by Topsoe and Dumesic et al. in the 1990s for V_2O_5-TiO_2 [130,131] (see Figure 15) seemed to be still valid in the 2010s for V_2O_5-WO_3/TiO_2, as also recently summarized by Han et al. [132].

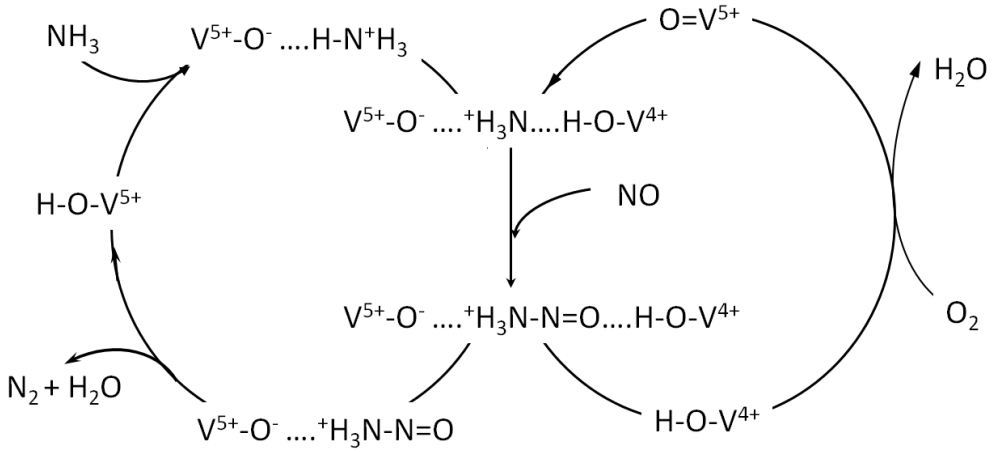

Figure 15. Mechanism of NH_3-SCR over V_2O_5-TiO_2. It combines NH_3 activation over Brønsted acid sites and a reoxidation of V^{4+} to V^{5+} (Brønsted V^{4+}-OH to vanadyl V^{5+} = O species). Insertion of NO into ammonium ion would be a key step of the mechanism. Reprinted from [130] with permission from Elsevier.

This mechanism, however, contrasts with the amide–nitrosamide mechanism proposed by Lietti et al. [133] in which NH_3 is predominantly activated on Lewis sites as amide species (Equation (2)). The main steps of this mechanism lead to the formation of NH_2NO (nitrosamide) (Equation (3)), which further decomposes into N_2 + H_2O.

$$H_3N{:}\rightarrow V^{5+} - O^{2-} \Rightarrow V^{4+} - NH_2 + OH^- \quad (2)$$

$$V^{4+} - NH_2 + NO \Rightarrow V^{4+} - NH_2NO \quad (3)$$

Another important feature to consider is the formation of N_2O. Nitrous oxide is a potent greenhouse gas with a global warming potential of 295–300 times that of CO_2 [134,135]. Its concentration in exhaust gases should be controlled. Djerad et al. reported that N_2O is formed at high temperature (T > 300 °C) in the NH_3-SCR process over V_2O_5-WO_3/TiO_2 [136]. Nitrous oxide concentration increases with the vanadium loading in the catalyst and is formed via NH_3 oxidation (Equation (4)).

$$2NH_3 + 2O_2 \rightarrow N_2O + 3H_2O \quad (4)$$

Liu et al. showed that the use of titania supports with high surface area would be a key to reduce N_2O formation [137]. Vanadium being more dispersed on these supports, ammonia oxidation to N_2O could be favored on polymerized vanadyl species.

4.1. Mechanisms and Surface Intermediates

The nature of active sites and the surface intermediates were investigated by Zhu et al. by in situ IR spectroscopy [138]. The first step of the mechanism would be the adsorption of ammonia on acid sites either as NH_{3ads} (on Lewis (L) sites) or NH_4^+ (on Brønsted (B) sites). The surface VO_x sites ($V^{5+}{}_L$ and $V^{5+}{}_B$) are the active sites for the reaction, tungsta sites ($W^{6+}{}_L$ and $W^{6+}{}_B$) being significantly less active. Both B and L sites participate in the reaction. However, if Brønsted sites are more abundant, Lewis sites possess the highest turnover frequency. Overall, ammonia adsorption is part of a complex NO_x removal mechanism and results in hydrogen abstraction to provide $–NH_2$ amide-type species. Hydrogen migration is involved in both acidity conversion for Lewis to Brønsted acid site transformation at T > 300 °C and reoxidation for the redox loop of the $DeNO_x$ reaction [139]. In addition, coordination of ammonia on Lewis acid sites does not prevent the dissociative H_2O chemisorption and the formation of Brønsted acid sites, leading to adsorbed NH_4^+ species [140].

Surface acidity and redox properties, as well as their effect on SCR activity, were investigated by Zhao et al. on a series of V_nW-TiO_2 with various vanadium loadings (1–13 wt.%), while keeping the tungsten loading constant (8 wt.% WO_3) [141]. The main characteristics of the series are reported in Table 3. The highest activity observed for the V9W-TiO_2 sample is correlated with both higher V^{4+}/V^{5+} ratio and higher Brønsted concentration sites. Redox properties do not seem to play a major role. Additional conclusions resulting from experimental analyses and DFT calculations show that the structure of vanadyl species plays a crucial role in $DeNO_x$ performances; polymeric species demonstrate higher NH_3-SCR activity than monomeric vanadyl compounds [142]. Besides, based on XPS results, low-valence vanadium species (V^{4+} and V^{3+}) were recently claimed to enhance SCR activity compared to the V^{5+} form [143]. Both low-valence vanadium species and polymeric surface VO_x species drive the NH_3-SCR activity at low temperature (T < 350 °C), as previously mentioned in [142].

Table 3. Vanadium state and acid and redox properties of a series of VnW-TiO_2 catalysts (n: vanadium loading (%), $1 \leq n \leq 13$; [WO_3] = 8%). TiO_2 (120 $m^2\ g^{-1}$) mainly as anatase. Acid site concentrations were measured by pyridine adsorption monitored by FTIR (bands at 1580 and 1633 cm^{-1} for Brønsted sites; bands at 1597 and 1438 cm^{-1} for Lewis sites). H_2-TPR peaks are between 535 and 569 °C, while O_2-TPO gives peaks around 450–460 °C. The mean rate of reduction (νTPR) and oxidation (νTPO) are given in the table. SCR activity was measured between 150 and 420 °C in a flow of 1000 ppm NO + 1000 ppm NH_3 in 5% O_2 (WHSV: 20,000 h^{-1}). NO conversion at 200 °C is representative of the activity order. From Zhao et al. [141].

Catalyst	V^{4+}/V^{5+}	B Sites	L Sites	νTPR	νTPO	SCR Activity: NO Conv. at 200 °C
	(XPS)	(μmol m^{-2})	(μmol m^{-2})	(nmol $m^{-2}\ s^{-1}$)	(nmol $m^{-2}\ s^{-1}$)	(%)
V1W/TiO_2	0.45	28	131	2.4	0.95	19.5
V5W/TiO_2	0.99	57	153	4.6	1.4	38.0
V7W/TiO_2	1.47	149	292	7.5	2.1	41.5
V9W/TiO_2	1.73	164	318	8.6	2.9	60.5
V11W/TiO_2	0.88	140	325	8.8	7.6	51.5
V13W/TiO_2	0.50	98	485	1.1	1.0	44.0

The crystallinity of WO_3 has a significant effect on vanadia dispersion [127]. Two-dimension VO_x moieties have a tendency to anchor onto the titania surface in the vicinity of WO_x. Small WO_3 crystallites are preferable to WO_x amorphous layer occupying a large surface of titania. Nevertheless, a compromise should be found because bulk tungsten oxide is less acidic than the dispersed oxide.

Interactions between tungsten oxide and vanadia were reinvestigated by Kompio et al. to better understand the promoter effect of tungsten on SCR activity during heat treatments and thermal stress [144]. The study was carried out on a V1.5-W10/TiO_2 catalyst (anatase, 140 $m^2\ g^{-1}$ after low-temperature calcination at 350 °C). Heat treatments generally provoke catalyst deactivation. However, several maxima of activity were observed during the

global decrease in activity when the support BET area reached 42 $m^2\ g^{-1}$ and 20 $m^2\ g^{-1}$. New surface sites were then created because isolated vanadia species, less active, were replaced by more active bridged V-O-V sites. Similar active species were proposed by Kwon et al. for non-tungstated V/TiO_2 catalysts calcined at 600 °C [145]. Marberger et al. underlined the fact that the presence of water is required to judge the thermal stability of the catalysts [146]. Water accelerates sulfate group removal (generally present in commercial titania), which changes the acidity of the catalysts. Water also accelerates the loss of BET surface area and V volatility. However, curiously, it tends to increase the vanadium dispersion (Table 4). Authors recently confirmed the mobility of the VO_x and WO_x species of the catalyst exposed to hydrothermal aging together with various structural changes of surface acidity [146]. Additionally, Liang et al. [147] observed that gas flow containing SO_2 and H_2O decreased the number of NH_3 adsorption sites, active component content, specific surface area and pore volume over F-containing V_2O_5-WO_3/TiO_2 catalysts.

Table 4. Comparison of dry (10% O_2 in N_2) and wet (10% O_2 + 10% H_2O in N_2) aging of a commercial V_2O_5 (2%)-WO_3(10%)/TiO_2 catalyst. Vanadium emissions and VO_x surface coverage (based on 7.9 $VO_x\ nm^{-2}$ for one monolayer). From Marberger et al. [146].

	Gas Feed	550 °C	600 °C	650 °C
V release (μg m^{-3})	dry	1.0	1.4	34.2
	wet	2.1	49.3	201
VO_x coverage (%)	dry	24	32	42
	wet	27	37	44

Another possible cause of deactivation is the transformation of anatase to rutile, a poorer support of vanadia and tungsta for the SCR reaction. Promotion of titania by silica can prevent rutile formation above 600 °C and give more stable catalysts [148,149]. A commercial catalyst named VSCR1 has been compared to a catalyst doped with 4–5% SiO_2, named VSCR2. Figure 16 shows the global behavior of the two catalysts when they are calcined at 600, 700 and 800 °C.

A dramatic improvement of the catalyst stability is obtained by Si doping. Maintaining the anatase phase is correlated with a decrease in the WO_3 and V_2O_5 phase segregation into monoclinic tungsten oxide and vanadia crystallites. It seems that SiO_2 tends to segregate as bulky silica crystallite at high temperature (>600 °C) [149]. Only small polymeric entities formed by a minute amount of silica can prevent catalyst deactivation. Deactivation is often observed after hydrothermal treatments at high temperature. However, this is not the case in all circumstances. Chen et al. prepared V-W/TiO_2 catalysts in two steps: (i) WO_3/TiO_2 was first prepared by mixing metatitanic acid and ammonium paratungstate; (ii) the solid, dried and calcined at 550 °C, was then impregnated with 1% V_2O_5 using metavanadate dissolved in monoethanolamine [143]. The resulting catalyst was finally hydrothermally treated at 750 °C. This treatment induced a decrease in surface area but resulted in considerably higher SCR activity. In fact, more V^{4+} and V^{3+} species were found on the catalyst treated at 750 °C, which explains its better SCR performances.

WO_3-TiO_2 catalysts, without vanadia addition, were investigated by Shin et al. [150]. Tungsten oxide was well dispersed in the interlayer between the grains of titania, avoiding TiO_2 sintering. It created surface acid sites (mainly Brønsted), giving the material a good SCR activity.

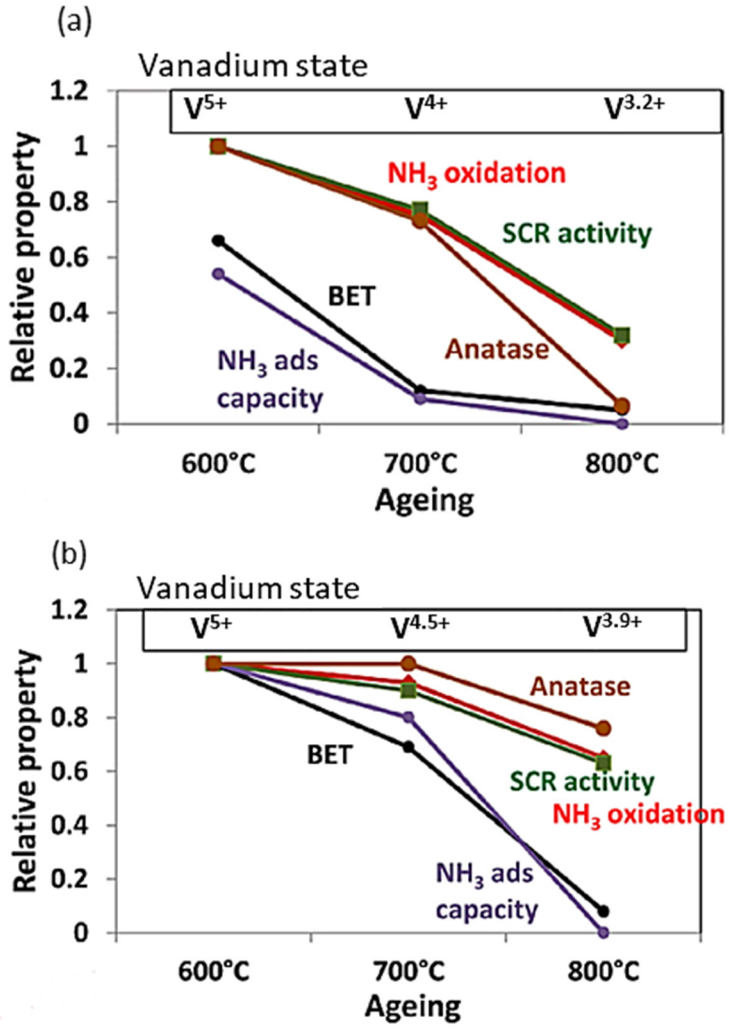

Figure 16. Changes of the catalyst characteristics upon temperature aging: reference V-W/TiO_2 catalyst (**a**) and Si-doped catalyst (**b**). From Beale et al. [148].

4.2. Influence of the Preparation Method: Powder and Monolithic Catalysts

Powder V-W/TiO_2 catalysts are commonly prepared by impregnation of anatase with aqueous solutions of ammonium metavanadate (NH_4VO_3) and ammonium metatungstate hydrate $(NH_4)_6(H_2W_{12}O_{40})\cdot xH_2O$ or paratungstate hydrate $(NH_4)_{10}(H_2W_{12}O_{42})\cdot 4H_2O$ precursors. He et al. evaluated the role of the synthesis method and showed that co-precipitation of the three elements—V, W and Ti—gave the best results in terms of SCR activity [151]. Coprecipitated catalysts possess new O-VO_3 and O-WO_4 sites that enhance the ammonia adsorption capacity. The origin of the best results obtained with coprecipitated catalysts is not clear. Titania is present as poorly ordered anatase with many defects, while acidity is not strengthened with respect to impregnated catalysts. Tungsten–titanium pillared clays were shown to be excellent supports of vanadia for the NH_3-SCR reaction [152]. A great advantage of this preparation method is the better control of the intimacy of contact between W and Ti, which are both inserted in clay pillars. The addition of S or N compounds during the preparation of TiO_2 clearly enhanced the performances.

SCR catalysts should be deposited on monoliths before practical use in $DeNO_x$ processes. Differences in color, structure and local activity of the V-W/TiO_2 deposit depending on its location (center, monolith periphery) were studied by Wang et al. on commercial honeycomb catalysts [153]. As these catalysts were designed for denitrification of flue gases, NH_3-SCR was tested in presence of SO_2. In the monolith, initially yellow, some grey areas may appear in used catalysts. This due to changes of the vanadium valence state

from +5 (V_2O_5 is bright yellow) to +4 (VO_2 is yellow darker, almost brown) and +3 (V_2O_3 is brown). This study confirms that the V-W/TiO_2 is tolerant to a certain amount of SO_x.

Monoliths pretreated in an acidic medium seem to give good impregnation characteristics [154]. The fabrication process is illustrated in Figure 17. Best results in NH_3-SCR were obtained with the monolith impregnated three times with 3% V + 10% W.

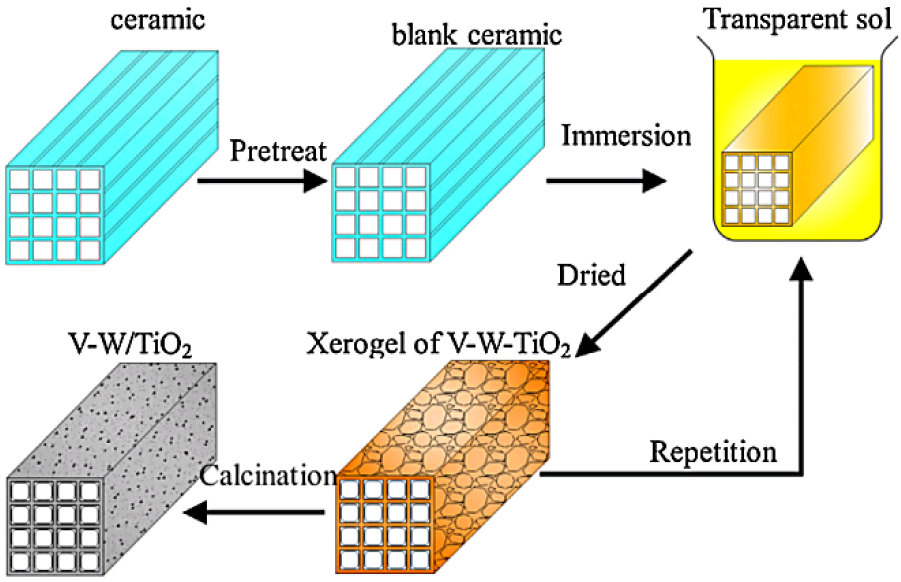

Figure 17. Preparation of V-W/TiO_2 monolithic catalysts. The ceramic is pretreated in nitric acid and calcined at 500 °C. It is then immersed in a mixture of solutions A and B consisting of butyl titanate in ethanol (sol. A) and metavanadate + ammonium tungstate in ethanol/nitric acid (sol. B). It is dried at 80 °C and calcined at 500 °C. From Zhao et al. [154] with permission from Elsevier.

In the NH_3-SCR technology dedicated to automotive applications, ammonia is generally provided by urea decomposition/hydrolysis, even though some applications using liquid ammonia have been envisaged [155]. Combining WO_3-V_2O_5/TiO_2 (upstream) and Cu-zeolite (downstream) catalysts was proven to give excellent performances in urea-SCR technology [156]. Deterioration of activity of the W-V/TiO_2 catalyst above 270 °C was compensated by the high performance of the zeolite catalyst. Lower N_2O selectivity was observed in the dual catalyst. Similar results were obtained by combining WO_3-V_2O_5/TiO_2 and Fe-zeolite catalysts [157].

4.3. Poisoning of V_2O_5-WO_3/TiO_2 Catalysts

Apart from the physical deactivation of WO_3-based catalysts due to its working time (e.g., sintering, volatilization of active elements), the system can suffer from chemical poisoning [158]. In 2008, Kröcher et al. reported a detailed study on the deactivation of V_2O_5-WO_3/TiO_2 catalysts by inorganic impurities of lubricants, biodiesel or urea solutions [159,160]. Among all the poisons tested, potassium had the strongest effect on both catalytic activity and N_2O selectivity (at 500 °C). The poisons can be ranked as follows: K >> Ca >> Mg > Zn > P. These results prompted researchers to focus their investigations on K and Ca poisoning (Section 4.3.1). Another poison present in exhaust gases or flue gases is sulfur dioxide. The effect of SO_2 was also investigated by several authors, as presented in Section 4.3.2; poisoning by arsenic is presented in Section 4.3.3.

4.3.1. Potassium and Calcium Poisoning

Potassium is a poison of acid sites and inhibits NH_3 adsorption. Xie et al. investigated the poisoning of a W-V/TiO_2 catalyst exposed to the flue gas of a coal-fired power plant [161]. They showed that alkali contaminants (mainly K) contained in the flue gas preferentially poison the vanadium sites (V^{5+}–OH and/or V^{5+}=O) rather than the sites

associated with tungsten oxide or TiO_2. A detailed kinetic analysis reveals that NH_3 adsorption/desorption, NH_3 oxidation and $DeNO_x$ activity are all affected by K poisoning. Similar tendencies were demonstrated by Siaka et al. [162], who claim that potassium preferentially neutralizes strong acid sites and alters V=O redox sites, leading to stabilization of well-dispersed VO_x species. Contrasting with the results of Xie et al., Chen et al. concluded that tungsten oxide can serve as a sacrificial agent protecting vanadia from severe K poisoning [163]. The combined effect of potassium and chloride ions showed that KCl is a more severe poison than KOH [164]. A higher amount of potassium was fixed by the catalyst when KCl was used as a potassium precursor. Better performance and especially higher potassium tolerance were obtained by doping the V_2O_5/TiO_2 catalyst with 15% HPA ($H_3PW_{12}O_{40}$, $H_4SiW_{12}O_{40}$ or $H_3PMo_{12}O_{40}$) instead of 10% WO_3 [165]. HPA does alter vanadium dispersion and does not increase N_2O formation. A higher concentration of acid sites could explain the higher K tolerance. By studying multielement poisoning systems, Mia et al. [166] found that phosphorous–potassium combination results in lower deactivation than single potassium poisoning. The advanced explanation is that new active sites generated by phosphorous react with potassium to liberate V-OH acidic sites. Concomitantly, alkali species may provide additional basic sites for NO_2 adsorption, enabling gaseous ammonia to react with adsorbed NO_x compounds for fast SCR stoichiometry [167]. Finally, potassium resistance may be strengthened by Ce and Cu addition over V_2O_5-WO_3/TiO_2 SCR materials due to an enhancement of V^{5+} amount and active oxygen species [168].

Calcium poisoning was investigated in detail by Li et al. [169,170]. The degree of poisoning follows the order $CaCO_3$ > CaO > $CaSO_4$. It is linked to the ability of the precursor to form calcium tungstate [170]. $CaCO_3$ decreases oxygen availability, vanadium reducibility and acid site concentration. If calcium sulfate is a less severe poison than CaO and $CaCO_3$, it tends to increase the N_2O selectivity. The catalysts can be regenerated by using specific treatment based on 1-hydroxy ethylidene-1,1-diphosphonic acid (HEDP) liquid under weak acid environment [169]. Odenbrand investigated the effect of $CaSO_4$ on kinetic parameters of NH_3-SCR over W-V-TiO_2 catalysts [171]. He concluded that Ca introduced into the pore system by impregnation strongly poisons the catalyst, but in a different way from that when it is coming from the engine during operation. $CaSO_4$ affects both activation energy and NH_3 heat of adsorption. A moderate effect on N_2O selectivity was observed.

4.3.2. Sulfur Poisoning

Tungsten-promoted V_2O_5/TiO_2 catalysts are not resistant to SO_2 for the NH_3-SCR reaction. Antimony oxide [172], molybdenum oxide [173] or iron oxide [174] are better promoters of these catalysts for sulfur resistance. Xu et al. confirmed the superiority of V_2O_5-Sb_2O_3/TiO_2 compared with the commercial V_2O_5-WO_3/TiO_2 catalyst for SO_2 resistance [175]. Sulfur deactivation is due to the formation of a surface layer of NH_4HSO_4 [176]. Compared to tungsten, Sb-doped catalysts have a lower activity for SO_2 oxidation to SO_3, which leads to weaker deposit of ammonium sulfate. Moreover, it seems that NH_4HSO_4 is more reactive with NO when it is deposited on V_2O_5-Sb_2O_3/TiO_2 [175]. The sulfur resistance of iron-promoted WO_3/TiO_2 is also reported in [177], where non-vanadium-based catalysts present thorough regeneration. Nobia-doped materials also exhibit significant sulfur resistance [178]. Nb_2O_3-CeO_2/WO_3-TiO_2 (NbCeWTi) catalyst presents mainly ammonium hydrogen sulfate species after H_2O and SO_2 exposition that protect Ce^{x+} active sites.

SO_2 resistance of V_2O_5-WO_3/TiO_2 catalysts can be improved by the addition of WO_3-graphene nanocomposite [179]. WO_3 remains well dispersed on graphene, which tends to decrease the SO_2 oxidation activity. Moreover, WO_3 acidity is preserved on graphene, essential for a good SCR activity. In another attempt, sulfur resistance was successfully increased by the addition of barium sulfate [180]. $BaSO_4$ contributed to reinforcing the acidity of the catalysts while blocking the SO_2 oxidation activity.

4.3.3. Arsenic Poisoning

Arsenic is present in the gas phase of power plants and may reach concentrations of up to thousands of micrograms of As_2O_3 per cubic meter [181]. Power plant gases can be treated with limestone to reduce arsenic concentration. The compound thus formed is ($Ca_3(AsO_4)_2$), and it may be condensed or adsorbed on ashes, decreasing the final As concentration to less than 100 μg m^{-3}. However, even at this concentration, As remains a severe poison for NH_3-SCR catalysts. Deactivation of V_2O_5-WO_3/TiO_2 catalysts was investigated by Peng et al. [182,183] and Kong et al. [184]. Arsenic oxides decrease Lewis acidity and tend to form very unstable As-OH Brønsted sites. At a certain concentration, As_2O_3 is oxidized to As_2O_5, much less active for NH_3-SCR but more active for NH_3 oxidation, leading to N_2O in significant amounts. As_2O_5 forms a dense layer at the catalyst surface, which reinforces the deactivation effect of arsenic. It was proven that catalysts promoted by Mo instead of W are more resistant to As poisoning.

Synergetic poisoning effect of arsenic with potassium was evaluated in [185,186]. Results indicated that the coeffect of As + K was more dramatic than the additive effect of a single poison. As previously discussed, arsenic loading leads to the formation of As-OH acid sites, which can be neutralized by potassium deposits. In addition, the effect of charge-compensating anions was also investigated, with the following enhancement ranking sequence: SO_4^{2-} < Cl^- << NO_3^-. Finally, catalysts poisoned by arsenic could be almost regenerated by sulfuric acid treatment, leading to the recovery of Lewis and Brønsted acid sites. However, the main drawback remains the formation of chelating bidentate sulfates and the loss of vanadium species [187]. Alkali solution treatment by single sodium carbonate [188] or with sodium hydroxide combined with sulfuric acid [189] also demonstrated interesting regeneration results.

4.3.4. Metal Release and Reuse of V-W-TiO_2 Catalysts

A cause of slow but irreversible deactivation of V_2O_5-WO_3/TiO_2 catalysts is the metal release at high temperature (T > 600 °C) [190,191]. Vanadium $VO(OH)_3$ and tungsten $WO_2(OH)_2$ oxo-hydroxides are responsible for the greatest part of the metal release. This effect is more important on agglomerated vanadium and tungsten particles, especially when the support undergoes severe sintering. Therefore, metal release is significantly reduced with catalysts supported on stabilized titania. Tungsten can be recovered from spent catalysts by a chemical treatment consisting of an alkaline leaching–ion exchange method [192].

Spent catalysts were also used to prepare new W-V catalysts. Huo et al. reported a feasible preparation method for a visible-light-sensitive $BiVO_4$/Bi_2WO_6 heterojunction photocatalyst from waste SCR catalysts [193].

4.4. Cerium-Promoted WO_3 Catalysts for NH_3-SCR

Promotion by ceria was studied in detail in the last decade. Redox properties [194,195] and oxygen mobility on ceria [196,197] could have a major impact on the NH_3-SCR reaction [198]. Ceria could be added to V_2O_5-WO_3/TiO_2 catalysts, WO_3/TiO_2 catalysts (without vanadia) or WO_3 catalysts (without vanadia and titania).

4.4.1. Ceria Added to V_2O_5-WO_3/TiO_2

The addition of ceria to V_2O_5-WO_3/TiO_2 for the NH_3-SCR reaction was investigated by Chen et al. [199]. The great merit of ceria is the enhancement of the $DeNO_x$ activity at low temperature (below 300 °C). For instance, with a catalyst having typical composition close to that of commercial materials (1% V_2O_5–9% WO_3), a NO_x conversion of 52% is obtained at 200 °C in the following conditions: 500 ppm NO, 500 ppm NH_3, 3% O_2 and 28,000 h^{-1}. Addition of 5% CeO_2 increases NO conversion up to 88%, while manganese oxide has virtually no effect (NO conversion = 50%), and iron oxide decreases NO conversion down to 15%. Vanadium oxide being responsible for the formation of N_2O at high temperature, attempts were made by Chen et al. to significantly reduce the vanadium loading down to 0.1% while maintaining a good activity by doping the $V_{0.1}W_6Ti$ with ceria [199]. Above

5% CeO_2, activity of $V_{0.1}W_6CexTi$ becomes equal or superior to that of V_1W_9Ti at 200 °C. In the meanwhile, N_2O formation is virtually suppressed on the low-loaded vanadium catalysts. This effect is still more marked on Ce-doped catalysts. Addition of ceria leads to complex features since the basicity of titania seems to be reinforced while there are stronger and more active Brønsted acid sites on VWTi.

Series of CeO_2-V_2O_5-ZrO_2/WO_3-TiO_2 catalysts with different loadings of ceria were prepared by Wang et al. [200]. They confirmed the specific role of ceria in improving both the low-temperature activity and the N_2 selectivity at high temperature (less N_2O). However, the zirconia-free catalyst (CexV1/W8Ti) has a poor hydrothermal stability (750 °C, 10% H_2O, 12 h). Addition of zirconia (10%) significantly reinforces the stability of the ceria-promoted catalyst. Ceria also has a great influence on the reaction mechanism. Ce-doped catalysts (CeVZr/WTi) are extremely sensitive to the presence of NO_2 in the reaction gases and are much more active in fast SCR conditions (Equation (5)) than in standard conditions (Equation (6)). The influence of NO_2 is limited on the cerium-free catalysts (VZr/WTi), suggesting that NO_2 does not readily react via the fast SCR reaction in absence of ceria.

$$NO + NO_2 + 2NH_3 \rightarrow 2N_2 + 3H_2O \quad (5)$$

$$NO + \frac{1}{2} O_2 + 2NH_3 \rightarrow 2N_2 + 3H_2O \quad (6)$$

The group of Tianjin University investigated the method of introduction of cerium and vanadium on the commercial 10% WO_3/TiO_2 support [201]. Ceria was introduced either by impregnation of cerium nitrate (IMP) or by deposition–precipitation of cerium nitrate in the presence of ammonia (DP). Characteristics and performances of the catalysts are reported in Table 5.

Table 5. Comparison of VCe/WTi DP, VCe/WTi IMP and cerium-free catalyst in NH_3-SCR. Vanadium was introduced by impregnation on the support (VWTi) or on the Ce-doped support using the $VO(CO_2)_2$ complex (prepared by reaction of V_2O_5 powder with oxalic acid). SCR conditions: 500 ppm NO, 500 ppm NH_3, 5% O_2 and 4% H_2O. From [201].

Catalyst	BET Area	Ce^{3+} (%)	NO Conv.	N_2O
	(m^2 g^{-1})	(from XPS Data)	at 250 °C (%)	at 550 °C (ppm)
VWTi	80	-	35	14
VCeWTi IMP	80	44	42	8
VCeWTi DP	83	53	67	5

The catalyst prepared by deposition–precipitation shows higher performances for the NH_3-SCR reaction. This is not due to changes in the textural properties but to specific properties of ceria, more reducible in VCeWTi DP. This catalyst also possesses more acidic sites (mainly Lewis sites) associated with surface wolframyl and ceria species. Youn et al. studied the role of the order of impregnation of vanadium and cerium–tungsten [202]. They showed that vanadium impregnated first (CeW/V/Ti) gave better performances. Similar topics were recently explored by Liu et al. [203], who demonstrated that the impregnation sequence of W and Ce influence the NH_3 adsorption capacity and the $Ce^{3+}/(Ce^{4+} + Ce^{3+})$ ratio in correlation with catalytic results. Addition of copper to ceria (Cu-Ce-W-V/Ti) reinforces the beneficial effect of ceria at low temperature [204].

The specific role of ceria on the sulfur resistance of V_2O_5-WO_3/TiO_2 catalysts was investigated by Liang et al. [205]. Ceria helps to improve $DeNO_x$ activity and sulfur resistance. A 3% loading of ceria is optimal for better performances. Higher loadings of ceria are detrimental: they provoke a decrease in surface area and partial covering of vanadia by ceria. Complex formulae combining Ce and Mn doping were described by Zhao et al. Ce and Mn coaddition confers excellent H_2O and SO_2 resistance on V_2O_5-WO_3/TiO_2 catalysts [206]. SO_2 is mainly adsorbed on Mn^{4+} and Ce^{4+} cations, making the

active surface of V_2O_5-WO_3 free. A multiplicity of valence states of the elements would be beneficial to a high NO conversion. Additionally, codoping of Ce^{4+} and Zr^{4+} enhances the tolerance to alkali metals of V_2O_5-WO_3/TiO_2 catalysts, as K-poisoning resistance occurs by blocking potassium in the form of Ce-O-K structure [207].

4.4.2. Ceria Added to WO_3/TiO_2 (Without Vanadium)

A number of works were carried out on vanadium-free catalysts to better study the interaction between ceria and tungsten and its role in the SCR reaction. Chen et al. prepared CeO_2/TiO_2 and CeO_2-WO_3/TiO_2 catalysts by an ultrasonic method and investigated the reactivity of adsorbed ammonia with NO + O_2 by DRIFT [208]. Comparison of CeO_2/TiO_2 and CeO_2/WO_3/TiO_2 catalysts shows that tungsten has a dramatic effect on the SCR reaction: (i) it allows conversion of NO at lower temperatures (50% conversion is reached at 165 °C on CeWTi instead of 225 °C on CeTi); (ii) it increases the selectivity for N_2 at high temperature (less N_2O). Tungsten increases the number of Brønsted sites (virtually absent on CeTi) and tends to accelerate the cerium reduction (more Ce^{3+} in CeWTi). Another report by Chen et al. confirmed the important role of tungsten by increasing the oxidation activity of NO to NO_2, allowing the catalyst to work in fast SCR conditions [209]. Interaction between ceria and tungsta seems to play a decisive role in SCR activity and selectivity. Geng et al. compared WTi and CeWTi catalysts and showed that ceria is effective for the inhibition of N_2O formation when it is added to WO_3-TiO_2 [210].

Great efforts were made in the last decade to improve the preparation of cerium-based tungsten catalysts. Michalow-Mauke et al. developed a preparation method based on flame-spray (FS) pyrolysis of Ce, W and Ti precursors in tetrahydrofuran [211,212]. Compared to catalysts prepared by impregnation, catalysts prepared by FS synthesis show superior performances. This is due to a better dispersion of ceria and tungsta and to a greater interaction of these elements with titania leading to highly active Ce–O–W (especially Ce^{3+}–O–W^{6+}) and Ce–O–Ti sites [212]. The fact that FS synthesis mainly produces rutile instead of anatase does not seem to hamper the performance of the catalysts prepared by this technique. Sol–gel techniques were also used by Jiang et al. to prepare CeO_2-WO_3/TiO_2 catalysts [213]. Butyl titanate was dissolved in a solution of ethanol/water/nitric acid and then mixed with cerium nitrate and ammonium metatungstate. Different catalysts were prepared with 10% WO_3 and various loadings of ceria (from 0 to 40%). DeNO_x activity of these materials is visualized in Figure 18.

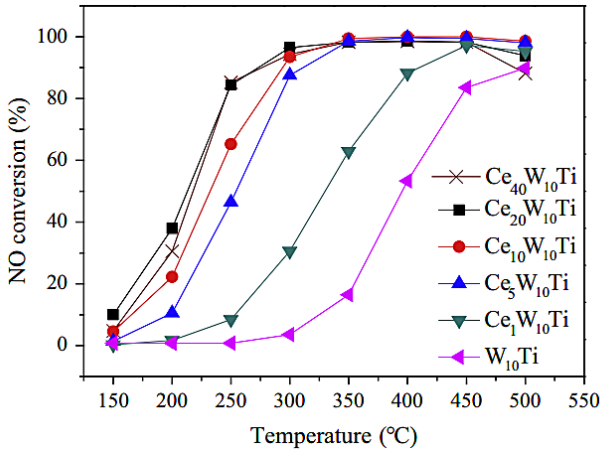

Figure 18. SCR activity of CexW10Ti catalysts prepared by a sol–gel method using butyl titanate as Ti precursor. Effect of cerium loading on NO conversion. Reaction conditions: 1000 ppm NO, 1000 ppm NH_3, 3% O_2. From Jiang et al. [213] with permission from Elsevier.

The catalyst with 20% CeO_2 shows the best performance in NH_3-SCR. It has also a good resistance to SO_2/H_2O when 500 ppm SO_2 and 10% H_2O are added to the reactant mixture. The same optimal composition (20% CeO_2) had already been observed on a

series of $Ce_xW_{20}TiO_2$ catalysts prepared by homogeneous precipitation with urea aqueous solution [214]. In every case, these CeO_2-WO_3-TiO_2 catalysts show exceptional resistance to SO_2.

Improved methods of preparation of CeO_2-WO_3/TiO_2 catalysts were recently reported, either using H_2O_2 as a promoter of active sites [215] or leading to 2D materials ($Ce_{0.184}W_{0.07}Ti_{0.748}O_{2-\delta}$ nanofibers prepared by electrospinning) [216]. H_2O_2 modification improves both the BET surface area and the number of Brønsted sites, while nanofibers seem ideal for a good performance at low temperature owing to the formation of a great number of oxygen vacancies. Salazar et al. investigated the method of impregnation of Ce and W on TiO_2 [217]. They showed that successive impregnation (with intermediary calcinations) of Ce on W/Ti led to higher performances than when catalysts were prepared by coimpregnation. Successive impregnation favors the formation of Ce-O-W bridges, which play an essential role in the SCR reaction. No clear correlation was observed between the SCR activity and the degree of Ce reduction or the number of Brønsted sites, even though these parameters are probably important for a good $DeNO_x$ activity.

Monolithic catalysts were prepared and tested by Cao et al. [218]. A TiO_2-SiO_2 powder was mixed with aqueous solutions of ammonium paratungstate and cerium nitrate. Ammonia was added up to pH = 10 to form a slurry which was extruded, dried and calcined at 550 °C. Silica was added to titania to increase its thermal stability. Excellent performances were obtained, superior to those of powder catalysts especially at high temperatures.

4.4.3. Ceria Added to WO_3 (Without Vanadia or Titania)

In order to avoid complex interactions between Ce, W, V and Ti, CeO_2-WO_3 catalysts were prepared and tested in NH_3-SCR. Zhang et al. compared the behavior of ceria doped with various acid promoters: phosphotungstic, silicotungstic and phosphomolybdic acids or ammonium sulfate [219]. Ceria doped with phosphotungstic (CeO_2-P-W) or silicotungstic acid (CeO_2-Si-W) showed the highest NO_x conversion (Figure 19). However, CeO_2-P-W exhibited the best N_2 selectivity over the whole temperature range, especially at T > 450 °C where N_2O could be formed.

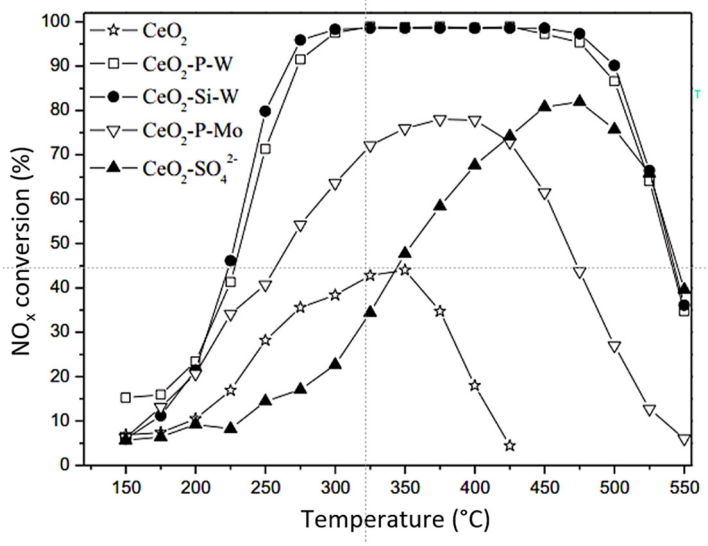

Figure 19. NO_x conversion over acid-promoted ceria catalyst. Ceria promoted by tungstic acids is much more active (800 ppm NH_3 + 800 ppm NO + 5% O_2, GHSV = 60,000 h^{-1}). From Zhang et al. [219] with permission from Elsevier.

The mode of preparation of ceria for the synthesis of P-W/CeO_2 catalysts was further investigated by Song et al. [220]. They compared hydrothermal (cerium nitrate + glucose + acrylic acid aged at 160 °C in autoclave), sol–gel (cerium nitrate in citric acid) and precipitation (cerium nitrate solution + ammonium carbonate) techniques. The P-W/CeO_2

catalyst with ceria prepared by hydrothermal technique gave the highest performances. It combined the highest BET area, the highest Ce^{3+} concentration and an adequate balance between Brønsted and Lewis acid sites. Wang et al. showed that the ceria morphology (cubes, particles, rods) would have a great impact on the performance of W-CeO_2 catalysts for the NH_3-SCR reaction [221]. Ceria supports were prepared by hydrothermal methods according to the synthesis procedures developed by Peng et al. [222]. Ceria nanorods were prepared from cerium acetate, while nanoparticles and nanocubes were synthesized using cerium nitrate. Nanocubes expose preferentially (100) planes while nanorods expose both (110) and (100) planes. Contrasting with these surface structures, (111) planes are essentially found with nanoparticles. Nanoparticles are more active than nanocubes and nanorods for the NH_3-SCR reaction, which tends to prove that WO_3 attached to (111) faces of ceria gives the best performances for NO_x abatement.

Modification of ceria by manganese shows that N_2O can be avoided by the incorporation of WO_3 into the catalyst. Better performances, with a good SO_2 and CO_2 resistance, were obtained with $W_{0.1}Mn_{0.4}Ce_{0.5}$ composition [223]. One of the roles of ceria is to promote redox properties by oxygen mobility improvement. As cerium–zirconium oxides have superior properties of reduction [194,224,225], it was logical to replace pure ceria with cerium–zirconium oxides in the preparation of supported WO_3 catalysts. These formulations were explored by Ning et al. [226]. Methods of preparation of CeO_2-ZrO_2-WO_3 (CZW) catalysts were similar to those developed by Song et al. for tungsten catalysts supported on ceria [220]. Catalysts prepared by hydrothermal methods show the best performance for the NH_3-SCR reaction. This is due to a higher tungsten dispersion and to the coexistence of Brønsted and Lewis acid sites, while CZW catalysts prepared by other techniques possess only Lewis sites. Acid properties of CeO_2-ZrO_2-WO_3 catalysts are greatly influenced by the state of tungsten oxide [227]. Moreover, the formation of amorphous W species resulted in the abundance of Ce^{3+} and oxygen vacancies with a correlative increase in the NO oxidation activity. Recently, great efforts were devoted to reinforcing the stability of SCR catalysts. Liu et al. showed that doping $WO_3/Ce_{0.68}Zr_{0.32}O_2$ with silica significantly improved the thermal stability of the catalyst (10% H_2O, 800 °C) [228]. Silica allows maintaining the acidity of the catalyst after thermal treatment. Moreover, it inhibits the formation of cerium tungstate $Ce_2(WO_4)_3$, which is detrimental to the catalyst performances. Similar effects were obtained by doping the CeZrOx support with alumina in monolithic catalysts [229]. The $Ce_xZr_{1-x}O_2$ composition also impacts the $WO_3/Ce_xZr_{1-x}O_2$ behaviors. The characterization of 9% $WO_3/Ce_xZr_{1-x}O_2$ catalysts with various ZrO_2 weight ratios in $Ce_xZr_{1-x}O_2$ (30%, 42%, 60% and 80%) indicated that the increase in the zirconium content enhanced the acidity (number and strength of acidic sites). Accordingly, the NH_3-SCR activity also increased [230]. Note that after WO_3 addition, the basic NO_x storage sites of $Ce_xZr_{1-x}O_2$ were fully altered while the oxygen storage capacities (OSC) were dramatically decreased for all samples.

4.5. Iron-Promoted WO_3 Catalysts for NH_3-SCR

Iron catalysts being promising SCR catalysts, especially when Fe is inserted in zeolites [231], it was logical that researchers attempt to associate Fe and W for the $DeNO_x$ reaction. Fe-W mixed oxides were studied for this application by Li et al. [232] and Wang et al. [233]. Catalysts were prepared by ammonia precipitation of ammonium paratungstate (APT) and iron nitrate [232], or by urea precipitation of ammonium metatungstate (AMT) and iron nitrate [233], which may explain some differences in performances for the two series of catalysts. Activity maximum was observed by Li et al. with the FeW5 sample (i.e., having a Fe/W molar ratio of 5), while the optimal performances were found by Wang et al. for a Fe/W ratio of 3 ($Fe_{0.75}W_{0.25}Ox$ sample). Location of acid sites would also be different: B sites on tungsten (W-OH) and L sites on iron (Li et al.), or B sites on $FeWO_4$ and L sites on Fe_2O_3, i.e., Fe oxide not associated with tungsten (Wang et al.). In fact, Wang et al. proposed that the good performances of $Fe_{0.75}W_{0.25}Ox$ would be due to a fine interaction between Fe_2O_3 and $FeWO_4$ with an easier electron transfer from W^{6+} sites to Fe^{3+} sites, which favors

the formation of NO_2. Wang et al. also reported that their mixed oxide catalysts were extremely resistant to SO_2 poisoning, especially at high temperature (T > 300 °C) [234]. Similar conclusions were reported for tungsten-free catalysts, where $Fe_{0.1}V_{0.1}TiO_x$ catalyst showed the optimal NH_3-SCR performance and excellent SO_2 resistance [174].

Direct impregnation of tungsten on hematite Fe_2O_3 was reported by Liu et al. [235]. Hematite was first prepared by urea precipitation of Fe nitrate. The solid (dried and calcined at 500 °C) was then impregnated with ammonium metatungstate solution in oxalic acid. Optimal performances were observed with the 5% WO_3/Fe_2O_3 sample. The reverse impregnation (iron on WO_3 nanorods) was studied by Li et al. [236]. It is difficult to compare the two methods of preparation. Nevertheless, both led to comparable $DeNO_x$ activity with a 50% NO conversion around 275 °C, even though the catalyst evaluation was carried out in somewhat different conditions.

Iron–tungsten was also supported on zirconia [237] or cerium–zirconium oxide for monolith preparation [238]. In absence of iron, supported tungsten shows a good ammonia oxidation activity but virtually no SCR activity. The presence of iron is required to create SCR catalysts whose activity is linked to the formation of Fe^{3+} Lewis sites. The main role of these sites would be to promote NO oxidation to NO_2, the first step in the SCR mechanism. These studies on ZrO_2 and $CeZrO_x$ were carried out with relatively high W loading (Fe/W molar ratio close to 1). Magnetic iron oxides doped with tungsten and cerium were also prepared as SCR catalysts [239]. In these materials, iron is mainly in the form of γ-Fe_2O_3 and α-Fe_2O_3, but other forms can be present since W and Ce tend to create highly dispersed iron species. Compared to previous catalysts synthesized over zirconia or $CeZrO_x$, higher iron loadings were used to prepare $FeCeWO_x$ catalyst (most active material: $Fe_{0.90}Ce_{0.05}W_{0.05}$ and $Fe_{0.85}Ce_{0.10}W_{0.05}$). Copper being an active component of SCR catalysts, it was tempting to promote iron catalysts with copper. Ma et al. reported a one-pot preparation of $Cu_{0.02}Fe_{0.2}W_xTiO_2$ materials (x varying from 0.01 to 0.03), which were tested in the SCR reaction [240]. A moderate amount of tungsten significantly improves stability and acid and redox properties, leading to superior performances for the SCR reaction, even in the presence of water and SO_2 (best formula: $Cu_{0.02}Fe_{0.2}W_{0.02}TiO_2$). Complex catalysts including several promoters (Fe, V, Mn, W, Ce) were also developed [241]. It appears that multiple redox pairs (Fe^{2+}/Fe^{3+}, V^{4+}/V^{5+}, Mn^{2+}-Mn^{3+}/Mn^{4+}) would play an important role in the reaction.

4.6. Manganese-Promoted WO_3 Catalysts for NH_3-SCR

Titania-supported manganese tungstate catalysts were prepared by Kong et al. in order to replace the standard V-W/TiO_2 catalyst for the NH_3-SCR reaction [242]. The solution combustion method with Mn, W and Ti precursors mixed with glycine is suitable for preparing high-surface-area materials (up to 280 $m^2\ g^{-1}$). Mn/TiO_2 without W showed a high activity at low temperature, which declined rapidly above 300 °C. Tungsten allowed enlarging the activity window up to 400 °C. The highest performance was obtained with the $Mn_{0.1}W_{0.05}Ti_{0.85}O_{2-\delta}$ catalyst. Similar materials were reported by Shin et al. [243] and Wang et al. [244]. In these studies, high tungsten contents were used (15% in [243] and 25% in [244]), which seems beneficial to improve the performance at low temperature. For instance, Wang et al. obtained a 50% NO conversion at 40–50 °C and 100% NO conversion from 80 to 280 °C over the $W_{0.25}Mn_{0.25}Ti_{0.5}O_2$ catalyst. The role of tungsten is to facilitate Mn redox capacity, leading to high concentration of Mn^{4+} and reactive oxygen species (Figure 20).

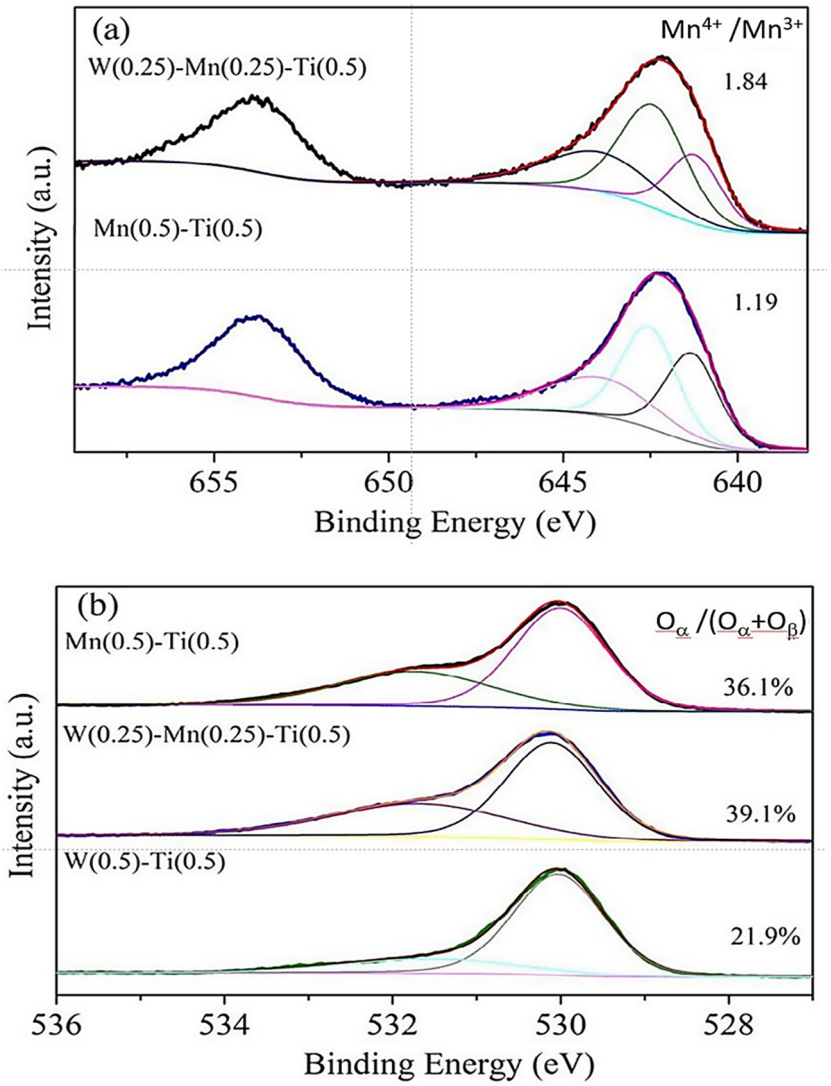

Figure 20. Characterization of Mn/TiO_2 and $W\text{-}Mn/TiO_2$ catalysts by XPS: Mn (**a**) and O (**b**) photopeaks. Presence of tungsten favors Mn oxidation to Mn^{4+} and formation of O reactive species (O_α). NO oxidation to NO_2 is improved on $W\text{-}Mn/TiO_2$ favoring the fast SCR reaction. From Wang et al. [244] with permission from Elsevier.

Additionally, a study investigating the vanadium loss from $V\text{-}W/TiO_2$ catalysts was conducted in [245] and reports that manganese is the best candidate to make up for the loss of SCR activity caused by the decrease in V_2O_5 loading (50%), in opposition to other transient metals as Nb, Co, Cr, Cu or Ce. Note that similar behaviors are denoted for tungsten-free catalysts: Mn-loaded catalyst ($Mn_5V_1Mo_3Ce_7/Ti$) exhibits the optimal SCR performance associated with a large number of acid sites and high redox properties [246].

Many studies were devoted to the promotion by cerium of manganese-based SCR catalysts. Nie et al. investigated the effect of several acidic oxides (Nb_2O_5, WO_3 and MoO_3) on the performance of $MnO_x\text{-}CeO_2$ catalysts [247]. NbCeTi and WCeTi are very active at 200 °C, while MoCeTi is active only at high temperature. WO_3-promoted catalyst has the broadest operation window with significant NO conversion above 300 °C. Ma et al. investigated the effect of WO_3 doping on the performances of $MnO_x\text{-}CeO_2$ catalysts for the SCR reaction [223]. The concentration of manganese in ceria was kept constant (Mn/Ce = 0.4) while the concentration of tungsten was varied from 0.03 to 0.2. Undoped $Mn_{0.4}Ce$ was active only at low temperature: its activity decreased sharply above 200 °C. WO_3-doped catalysts showed far better activity above 200 °C, with an optimum for the $W_{0.1}Mn_{0.4}Ce$ sample. $Mn_{0.4}Ce$ has only Lewis acid sites. Doping with tungsten generates

Brønsted sites allowing activity at high temperature. Moreover, High SO_2 resistance is also achieved on $W_{0.1}Mn_{0.4}Ce$ by suppression of SO_2 oxidation activity. Promotion by tin of MnO_x-CeO_2 support seems to favor low-temperature SCR activity [248]. High NO conversion is obtained on the $SnMnCeO_x$ support (50% at 60 °C but only 50% at 300 °C). Addition of tungsten shifts the conversion profile to higher temperatures with good activity and excellent N_2 selectivity up to 300 °C.

In several studies by the group of Hong (South Korea), WMnCe-based catalysts were supported on titania [249–251]. In the first two studies, WMnCeTi samples were prepared by wet impregnation without any control of the pH, while in the third study, a strict control of the pH between 2.8 and 1.7 was applied by addition of oxalic acid. Controlling the pH of the slurry around 1.7 leads to catalysts more active for the NH_3-SCR. This result is linked to the fact that an acidic pH increases the formation of surface Mn^{4+} and Ce^{3+}, while NO would be less strongly adsorbed. A good synergetic effect was observed with zirconia as support for manganese. Increasing the concentration of tungsten on $MnZrO_x$ allows obtaining catalysts more active and more selective for N_2 up to 400 °C [252]. XPS results and DRIFT studies on the most active catalyst (15%W/$MnZrO_x$) showed that the redox cycle (Equation (7)) would promote the electron transfer between W and Mn, contributing to NH_3 activation.

$$Mn^{4+} - O^{2-} - W^{5+} \Leftrightarrow Mn^{3+} - O^{2-} - W^{6+} \quad (7)$$

Developing active catalysts over a wide range of temperatures is a challenge for the NH_3-SCR reaction. Combining two catalysts (MnO_x-CeO_2/TiO_2 (MnCeTi) and V_2O_5-WO_3/TiO_2 (VWTi)), Zhang et al. were able to obtain high NO conversion from 150 to 400 °C [253]. The best configuration was obtained when VWTi was set at the fore part and MnCeTi at the rear part of the catalyst bed (Figure 21, CC-B curve). MnCeTi is much more active than VWTi for the NO oxidation reaction, allowing work in fast SCR conditions over a wide range of temperatures. MnCeTi is also more active for the NH_3 oxidation reaction, which has a less detrimental effect in CC-B configuration (VWTi + MnCeTi).

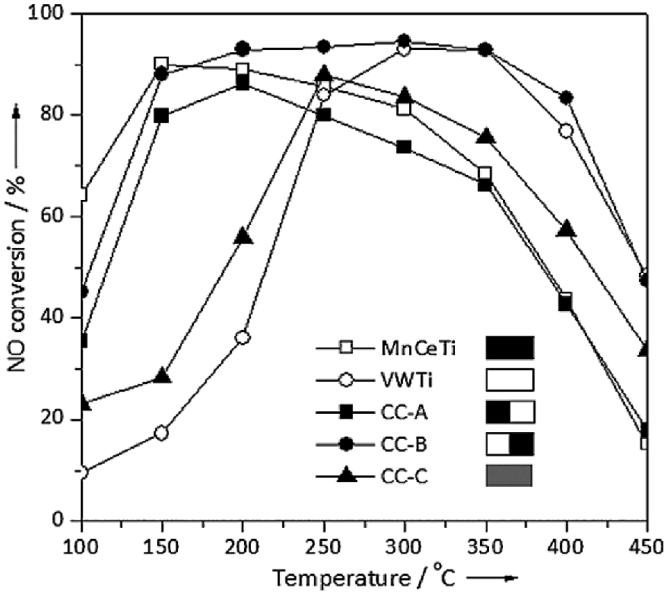

Figure 21. Combination of MnO_x-CeO_2/TiO_2 (MnCeTi) and V_2O_5-WO_3/TiO_2 (VWTi) catalysts for the NH_3-SCR reaction. Configuration CC-A: MnCeTi first and then VWTi; configuration CC-B: reverse position; configuration CC-C: physical mixture of the two catalysts. From Zhang et al. [253] with permission from John Wiley and Sons.

5. Other DeNO$_x$ Applications of WO$_3$-Doped Catalysts

5.1. Tungsten Catalysts for the NO$_x$ Trap–SCR Coupled System

One of the technologies for NO_x abatement in diesel engine exhausts is the NO_x trap system, also called NO_x storage reduction (NSR) or lean NO_x trap (LNT) [254]. The catalyst (typically Pt/BaO-Al_2O_3) works according to a sequential operation: (i) during one or two minutes, NO_x from the exhaust gases is stored on the catalyst as nitrate and nitrite species; (ii) during a few seconds, hydrocarbons are added to the exhaust gases for the reduction step, and adsorbed nitrates and nitrites are reduced to N_2. However, some ammonia may also be produced (ammonia slip), which should be eliminated on an ammonia oxidation catalyst. An alternative solution would be to use this in situ produced ammonia on an SCR catalyst to transform the residual NO_x not yet converted. This is the NO_x trap–SCR coupled system [255]. Several studies considered the coupling of Pt-BaO-Al_2O_3 (NSR catalyst) with Cu-zeolites (SCR catalyst) [256–259] or with Fe-zeolites [260,261]. Can et al. investigated the use of WO_3/CeZrOx (as SCR material) coupled to a usual Pt/BaO/Al_2O_3 catalyst [230]. The effect of adding an SCR catalyst ($WO_3/Ce_{0.58}Zr_{0.42}O_2$) downstream of the NSR catalyst is depicted in Figure 22. SiC being inert for all the reactions, NSR + SiC represents the performance of the NSR catalyst alone. The effect of adding an SCR catalyst to the NSR material is clearly visible in the figure: more NO_x is converted and more NH_3 produced on the first bed is consumed. N_2O is never produced on the NSR catalyst alone or on the coupled system NSR+SCR. In fact, a part of the ammonia produced on the NO_x-trap catalyst reacts with oxygen (NH_3 oxidation reaction or SCO). Fortunately, both SCR and SCO are selective for N_2 on these materials.

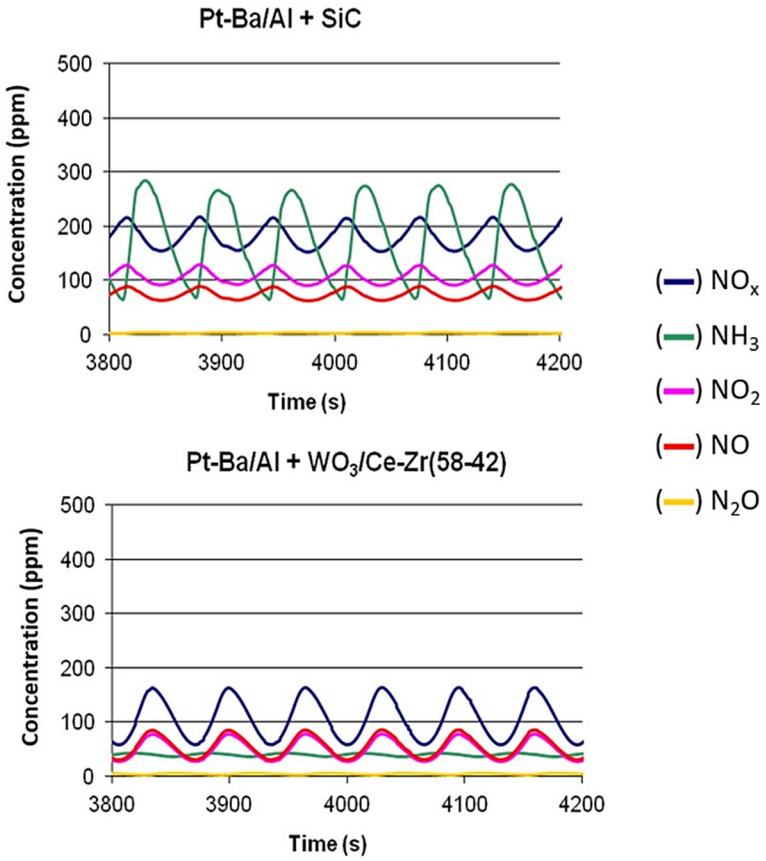

Figure 22. Analyses of nitrogen-containing gases during lean/rich oscillations. The catalysts were exposed to 500 ppm NO, 10% O_2, 10% H_2O and 10% CO_2 during the lean period (60 s) and to 3% H_2, 10% H_2O and 10% CO_2 during the rich period (3 s). From Can et al. [230] with permission from the American Chemical Society.

Other tungsten catalysts ($WO_3/Al_{0.2}Ce_{0.4}Ti_{0.4}$, $WO_3/Al_{0.2}Ce_{0.16}Zr_{0.32}Ti_{0.32}$ and $WO_3/Al_{0.1}Si_{0.1}Ce_{0.16}Zr_{0.32}Ti_{0.32}$, selected among 30 formulations) were also tested in the NO_x trap–SCR coupled process [262]. Ammonia release and its use in oxidation (SCO) or reduction (SCR) is shown in Figure 23 for four configurations of NO_x trap–SCR coupled systems. Configuration 4 with silica-containing SCR catalyst offers the best performances, especially at 300 °C. Presence of silica increases Lewis acidity and more strongly increases Brønsted acidity, which can explain the good behavior of the Si-doped catalyst.

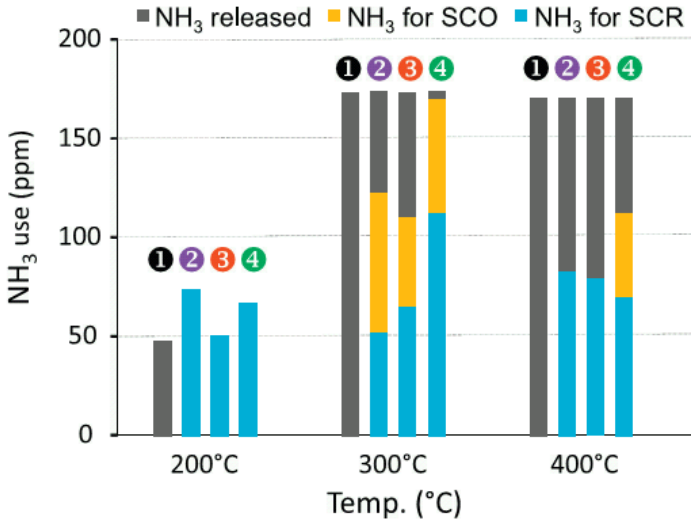

Figure 23. Ammonia release and use in SCO or SCR on different NO_x trap–SCR systems. In every case, 1%Pt/10%BaO-Al_2O_3 (Pt-BaAl) is used as NO_x trap catalyst. Configuration ❶ corresponds to Pt-BaAl + SiC (NO_x trap alone), ❷ to Pt-BaAl + $WO_3/Al_{0.2}Ce_{0.4}Ti_{0.4}$, ❸ to Pt-BaAl + $WO_3/Al_{0.2}Ce_{0.16}Zr_{0.32}Ti_{0.32}$ and ❹ to Pt-BaAl + $WO_3/Al_{0.1}Si_{0.1}Ce_{0.16}Zr_{0.32}Ti_{0.32}$. The catalysts were exposed to the same lean/rich oscillations as in Figure 22. From Can et al. [262] with permission from Elsevier.

5.2. Tungsten Catalysts for NO_x Reduction by Other Reductants

5.2.1. Reduction by Hydrogen (H_2-SCR)

NO_x reduction by hydrogen is well adapted to depollution of sites where hydrogen is available (e.g., refineries, H_2 plants) [263]. The authors of [263] investigated the H_2-SCR over WO_x-ZrCe (zirconium rich) and WO_x-CeZr (cerium rich) catalysts. Reaction conditions were 520 ppm NO + NO_2 (NO/NO_2 = 9), 5% O_2 and 10% CO_2. The reaction can be written as follows (Equation (8)):

$$NO + H_2 \rightarrow \frac{1}{2} N_2 + H_2O \quad (8)$$

However, formation of nitrous oxide (Equation (9)) and undesired hydrogen oxidation (Equation (10)) may be observed:

$$2NO + H_2 \rightarrow N_2O + H_2O \quad (9)$$

$$H_2 + \frac{1}{2} O_2 \rightarrow H_2O \quad (10)$$

Maximum activity is obtained at 250 °C over WO_x-CeZr and at 300 °C over WO_x-ZrCe. The Zr-rich catalyst WO_x-ZrCe shows better performances if the whole 150–600 °C temperature range is considered. This could be due to a higher concentration of acid sites on WO_x-ZrCe than on WO_x-CeZr (about twice). Selectivity for N_2 is close to 80–90%, with maximum formation of N_2O around 20 ppm over WO_x-CeZr and 15 ppm over WO_x-ZrCe. Addition of 7% water slightly decreases the NO_x conversion but improves the N_2 selectivity.

Platinum is one of the most active metals for the NO reduction by H_2 at low temperature [264–266]. Platinum activity and selectivity are extremely sensitive to the nature of support. For instance, Pt/ZrO_2 is superior to $Pt\text{-}Al_2O_3$ (more active and more selective for N_2), and promotion by WO_3 improves the performances of Pt/ZrO_2 [267]. NO_2 and nitrate species are thought to be essential intermediates in the reaction [265]. However, other authors found that NO adsorption and decomposition on Pt would be the most important step of the reaction [268,269]. Maximum NO conversion is observed between 90 and 130 °C. Zhang et al. reported a NO conversion of 91% at 110 °C over 0.1%Pt-1%W-HZSM-5 in the following reaction conditions: 910 ppm NO + 90 ppm NO_2 + 5000 ppm H_2 + 10% O_2. Tungsten oxide is thought to maintain Pt in the metallic state even in highly oxidizing conditions. It suppresses NO_2 adsorption on Pt and inhibits the formation of nitrate species. It accelerates the dissociation of NO and H_2 on Pt. The main drawback of H_2-SCR is the lack of N_2 selectivity due to ammonia formation. Platinum being a poor NH_3-SCR catalyst, this ammonia cannot be used for increasing the selective conversion of NO to N_2. By contrast, $Pt\text{-}WO_3$ is an excellent catalyst for selective oxidation of NH_3 (SCO), but only at higher temperatures (250–300 °C) [270]. Replacing Pt by Ru does not significantly improve the SCO reaction at lower temperatures [271], which does not allow selective conversion of ammonia formed in H_2-SCR.

5.2.2. Reduction by Ethanol (C_2H_5OH-SCR)

Alumina-supported silver catalysts are very active for the NO_x reduction by oxygenated compounds, especially ethanol or acetone [272]. It seems that the formation of isocyanate species (-NCO) is a key step of the ethanol-SCR reaction over Ag/Al_2O_3 [273,274] even though many other species may be detected [275,276]. This remarkable activity of silver catalysts for ethanol-SCR prompted Barreau et al. to imagine a combination between Ag/Al_2O_3 and a NH_3-SCR catalyst ($WO_3/CeZrO_2$) using $C_2H_5OH\text{-}NH_3$ mixture for NO_x reduction [277,278]. The effect of silver alone for the C_2H_5OH-SCR and for the $C_2H_5OH\text{-}NH_3$-SCR and finally the effect of adding $WO_3/CeZrO_2$ are illustrated in Figure 24.

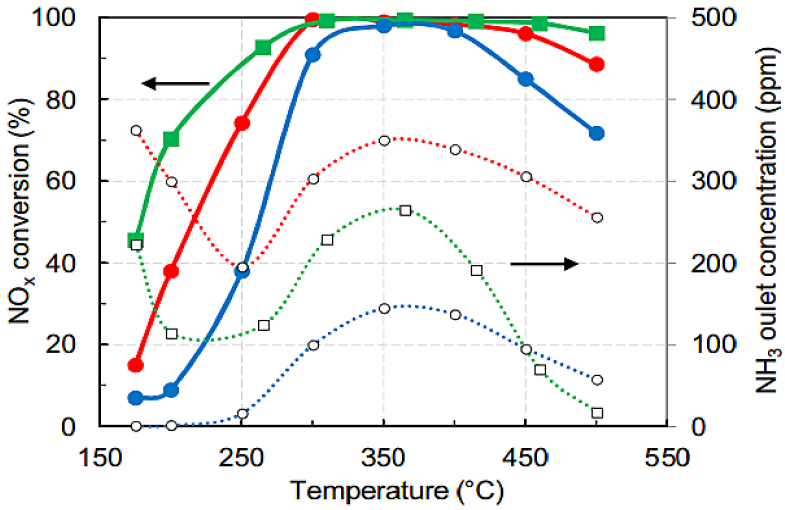

Figure 24. NO_x conversion and NH_3 outlet concentration in C_2H_5OH-SCR (blue) and C_2H_5OH + NH_3-SCR (red) on $2\%Ag/Al_2O_3$ and effect of adding $6\%WO_3/Ce_xZr_yO_2$ to Ag/Al_2O_3 in the C_2H_5OH + NH_3-SCR reaction (green). Mixture: 400 ppm NO + 1200 ppm C_2H_5OH + 400 ppm NH_3 (when present) + 10% O_2 + 10% CO_2 + 8% H_2O. From [277] with permission from Elsevier.

Silver alumina alone possesses a significant activity for the ethanol-SCR reaction (blue curve). The activity is enhanced by the presence of ammonia (red curve). In the dual bed (Ag + W) system (green curve), an increased conversion of NO_x is observed, and simultaneously the outlet concentration of ammonia is decreased.

The respective roles of Ag/Al_2O_3 and $WO_3/CeZrO_2$ in this complex reaction were summarized in the review by Barreau et al. [279]. Figure 25 illustrates the reaction pathway identified in the ethanol-NH_3 SCR reaction over the Ag/W dual bed. Note that $WO_3/CeZrO_2$ is then more suitable than a copper-exchanged zeolite (2.5% Cu–FER) as an SCR catalyst. Despite a significantly higher ammonia conversion rate using the zeolite, NO_x abatement is lower because ammonia and ethanol strongly interact together on Cu2.5–FER [278].

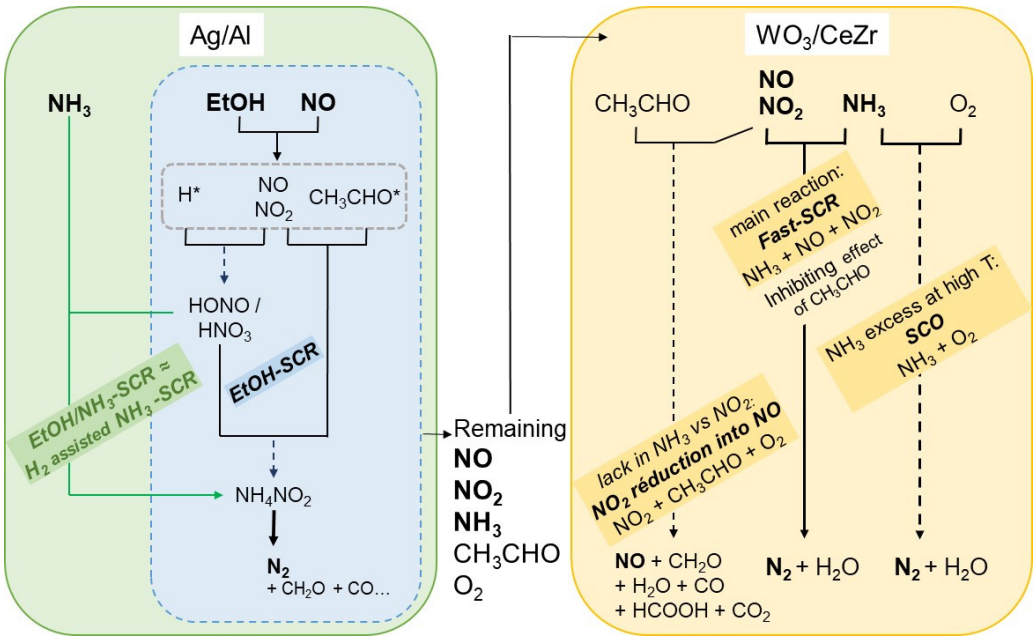

Figure 25. Reaction pathway identified in the ethanol-NH_3 SCR reaction over Ag/Al_2O_3 + $WO_3/CeZrO_x$ dual bed. Hydrogen species are key intermediates in the reduction of NO on Ag. The fast SCR is the main reaction over $WO_3/CeZrO_x$, but acetaldehyde formed over Ag tends to produce undesired reactions. Oxidation of NH_3 is observed at high temperature. Fortunately, this reaction is totally selective for N_2 over the tungsten catalyst. From Barreau et al. [279] with permission from Elsevier.

5.3. Conclusions

Tungsten-based catalysts are highly referenced as active samples in NO_x reduction abatement for a wide range of reducers or processes. Commonly used in V-W/TiO_2 catalysts for NH_3-SCR application, WO_3 is known to increase the activity, widen the temperature window, improve the resistance to various poisons and lower ammonia oxidation activity by O_2. Tungsten is also involved in V-O-V species formation by confining vanadia in small clusters leading to oligomeric vanadia (V_2O_5) sites, demonstrating higher NH_3-SCR activity than monomeric vanadyl compounds. WO_3 is also associated with ceria as redox support, with or without vanadia or titania, for low-temperature activity and N_2O limitation emission. Tungsten increases the number of Brønsted sites, favors the formation of Ce-O-W bridges and tends to accelerate the cerium reduction.

6. Total Oxidation of Volatile Organic Compounds in Gas Phase and Gas Sensors

Owing to the multiple oxidation states of tungsten and rapid diffusion of surface oxygen, WO_3 is also a candidate for oxidation reaction in gas phase [280], VOC oxidation (Section 6.1) and gas sensor application (Section 6.2).

6.1. VOC Oxidation in Gas Phase on Tungsten Catalysts

The first part of this section is focused on the non-photocatalyzed reactions. However, WO_3 is response-sensitive to light up to 480 nm, which also makes it a good candidate

for photoassisted VOC oxidation (Section 6.1.2). Note that WO_3-based photacatalysts for liquid phase applications are depicted in Section 7.

6.1.1. VOC Oxidation on Tungsten Catalysts (Non-Photocatalyzed Reactions)

Balzer et al. showed that WO_3 alone (7.5 m^2 g^{-1}) can efficiently catalyze BTX oxidation [281]. The reactivity of the different hydrocarbons is as follows: benzene (T_{50} = 250 °C) > toluene (T_{50} = 340 °C) > m-xylene (T_{50} = 420 °C) ≈ p-xylene (T_{50} = 430 °C). Oxidation activity of WO_3 is linked to the presence of W^{6+}, W^{5+} and W^{4+} surface species generating reactive oxygen species.

However, WO_3 is generally used in supported catalysts. Pansare et al. investigated NH_3 and toluene decomposition on tungsten carbide (WC) and tungstated zirconia (WZ) [282]. Both WC and WZ catalysts were active for the simultaneous decomposition of NH_3 and toluene at 700 °C in the presence of H_2, CO, CO_2 and H_2O. Benzene is formed by steam dealkylation of toluene. The WO_3-V_2O_5-TiO_2 catalyst usually employed for NH_3-SCR reaction (see Section 4) was proven to possess good oxidation activity for VOC abatement. Debecker et al. studied the total oxidation of benzene and chlorobenzene on a catalyst containing 3% WO_3 (or MoO_3) supported on titania variously loaded with vanadia (3 to 10% V_2O_5) [283]. The main results of this study are summarized in Table 6.

Table 6. Total oxidation of benzene and chlorobenzene (CB) at 300 °C on V_2O_5-TiO_2, 3%WO_3-V_2O_5-TiO_2 or 3%MoO_3-V_2O_5-TiO_2 catalysts. Reaction conditions: 100 ppm benzene or chlorobenzene, 20% O_2 in He. VVH = 37,000 h^{-1}. Adapted from [283].

	Benzene Conversion @ 300 °C (%)			**CB Conversion @ 300 °C (%)**
Vanadium Loading	**3% V_2O_5**	**5% V_2O_5**	**10% V_2O_5**	**10% V_2O_5**
No promoter	23	71	86	75
WO_3-promoted	34	77	98	93
MoO_3-promoted	43	83	95	93

Vanadium oxide was then the active phase for VOC oxidation. However, tungsten and molybdenum oxides significantly increased V_2O_5 activity. It is worth noting that promotion by WO_3 allowed reaching almost 100% conversion of benzene with the 10% V_2O_5 catalyst. WO_3 and MoO_3 promotion were also beneficial for chlorobenzene conversion, even though total oxidation cannot be reached at 300 °C. Benzene oxidation over WO_3-V_2O_5-TiO_2 catalysts was also investigated by Lu et al. [284]. Traces of benzene (1–10 ppm) were treated in a gas containing CO_2, CO, O_2 and H_2O, simulating a flue gas issued from a methane burner. HCl (50 ppm), SO_2 (400 ppm), NO (300 ppm) and NH_3 (360 ppm) were added to simulate a waste incineration flue gas atmosphere. Due to the very low concentration of benzene, its conversion was measured by resonance-enhanced multiphoton ionization time-of-flight MS (REMPI-TOFMS), a technique well adapted to analyze minute traces of hazardous air pollutants [285]. The most active catalyst was supported on a high-surface-area TiO_2 (166 m^2 g^{-1}, quasipure anatase) with a low loading of vanadia (0.8 wt.%) promoted by 6 wt.% WO_3. About 80% of benzene could be eliminated with little variation of efficiency when other pollutants (NO, NH_3, HCl, SO_2) were present.

Other tungsten-based catalysts were employed for VOC abatement. For instance, magnesium tungstate ($MgWO_4$)-based catalysts were evaluated by Gancheva et al. in CO and hydrocarbon oxidation [286]. Four catalysts were tested: pure $MgWO_4$ (5.2 m^2 g^{-1}), $MgWO_4$_3%WO_3 (4.0 m^2 g^{-1}) and these materials promoted by 0.5% Pd. Without palladium, pure $MgWO_4$ was more active than the same support enriched in WO_3. With Pd-promoted catalysts, two opposite behaviors were observed: $MgWO_4$/3%WO_3/0.5%Pd was the most active catalyst in hydrocarbon combustion (toluene, n-hexane) while $MgWO_4$/0.5%Pd (with no tungstate) was much more active for CO oxidation. Gancheva et al. proposed that CO and HC would be activated on $MgWO_4$ and WO_3 by two different mechanisms depending on

the nature of the reactant CO or HC. The role of palladium would be to favor O_2 adsorption and activation.

Catalytic abatement of trichloroethane (TCE) was performed on complex materials consisting of W-Mo bronzes (W-Mo/Nb/V/P) [287]. The best performances were obtained on the mixed W-Mo bronze with a W/Mo ratio close to 1. Complete composition (based on W + Mo = 1) was Mo(0.54)/W(0.46)/Nb(0.41)/V(0.20)/P(0.08). A 50% decomposition of TCE was achieved at 300 °C on this material, while a reference zeolite (HMOR) gave 50% conversion at 470 °C. The performance of this bronze catalyst was linked to its acidity (B sites only present on W-containing materials) and to its high oxygen mobility in the bulk, as revealed by $^{16}O/^{18}O$ exchange.

Tungsten oxide is also a good promoter of diesel oxidation catalyst (DOC) allowing increasing activity of noble meta—alumina catalyst: a gain of 20 °C on the light-off conversion of HCs was attained with 1% WO_3 on the reference $PtPd/Al_2O_3$ catalyst [288].

For ambient air purification, the very mild operating conditions require the development of fine structures/morphologies to improve the number of surface oxygen vacancies. With this aim, formaldehyde oxidation can be performed at room temperature by 1% Pt-doped WO_3 nanoflakes assembled into hollow microspheres (23 m^2 g^{-1}), in which the porous architecture promotes diffusion and adsorption of HCHO [289]. However, photoassisted catalysis appears more suitable for the very mild operating conditions.

6.1.2. WO_3-Based Photocatalysts for VOC Oxidation

WO_3-based materials as photocatalysts are mostly dedicated to reactions occurring in liquid phase (Section 7, in which general information about WO_3-based photocatalysts is provided). However, few recent studies reported that such catalysts also demonstrated intersecting behaviors in gas phase, especially for ambient air purification. To overcome drawbacks of bare WO_3, such as photocorrosion and unsuitable bandgap structure for the reduction of molecular oxygen, improvement can be obtained by structure/morphology control and/or doping. For instance, WO_3 nanoparticles obtained by gas phase method and annealing at 600 °C were reported to be much more active than commercial WO_3 in acetaldehyde oxidation. Oxidation rate can be further significantly improved by addition of ZrO_2, which acts as a sorbent for the acetic acid intermediate species to release the WO_3 surface. Moreover, Pt or Ru addition allowed the total mineralization into CO_2 and H_2O [290,291]. A physical mixture of WO_3 and CeO_2 also exhibited excellent photocatalytic activity in acetaldehyde oxidation, which was attributed to the electron scavenging property of CeO_2 aiding charge carrier separation [292]. WO_3 can be also associated with the other usual photocatalyst, namely TiO_2. To improve the visible light sensitivity of WO_3 nanoparticles impregnated into a commercial TiO_2 powder, Balayeva et al. successfully added Fe(III) nanoclusters. The observed enhancement in acetaldehyde photooxidation was then attributed to the promotion of multielectron reduction processes [293]. However, Caudillo-Flores et al. pointed out that a cautious approach must be adopted when interpreting the results. They prepared TiO_2/WO_3 samples with various W/Ti atomic ratios from 0 to 0.5, leading to various structures ranging from truly doped samples in which tungsten was exclusively located in lattice positions of the anatase structure to composite catalysts where nanosized tungsten species were supported over TiO_2. The authors highlighted that both the reaction rate (in toluene and styrene photo-oxidation) and the apparent quantum efficiency can lead to misleading results in terms of the most active TiO_2/WO_3 sample(s) as well as the (positive/negative) magnitude in comparison with bare titania reference [294].

Implementation of photocatalysts in building windows is of major interest in air purification. Li et al. proposed a g-C_3N_4@Cs_xWO_3 heterostructure as a coating for a multifunctional smart window for UV-isolating, Vis-penetrating, NIR-shielding and photocatalytic activity. These composites display excellent formaldehyde and toluene decomposition properties. The shielded NIR light is used instead of wasted as heat, while the C_3N_4@Cs_xWO_3 structure promotes the separation of charge carriers and then enhances photocatalytic oxidation. Moreover, the small polaron can jump from localized states to

the conduction band of Cs_xWO_3 under NIR irradiation (730–1100 nm), resulting in an NIR-catalytic reduction [295]. Note that this kind of structure was also proposed as a photocatalyst for water purification (see Sections 7.6.3 and 7.6.4).

6.2. Gas Sensors Using Tungsten-Based Catalytic Materials

Since the mid-1950s, gas sensors have experienced great development for environmental and safety applications. Gas sensors are based on the measurement of electrical behaviors caused by chemical changes. Expected properties are sensibility, selectivity, stability, repeatability and response time. To build low-cost sensors, the measurement of the resistivity of heated semiconductor oxides is suitable thanks to the cost of raw materials and the convenience of microelectronic integration. Details of the internal structure of the sensors, including the heater, electrodes and external circuit, are out of the scope of this review.

The sensing is related to changes in the electrical conductivity, which are mainly attributable to changes in the oxygen concentration at the oxide surface. Many oxides exhibit conductivity changes in presence of gases, but most of the commercialized sensors are based on SnO_2, WO_3 or ZnO. As reported in the recent review by Dong et al., a huge number of works have been devoted to tungsten oxide based sensors [296]. Tungsten oxide is sensitive to many gases such as O_2, O_3, CH_4, CO, H_2, NH_3, C_3H_8, NO, NO_2 and H_2S, with operating temperature in the 250–450 °C range [297,298]. WO_3 is an n-type oxide; i.e., the adsorption of surface oxygen atoms form an electron depletion region (Equations (11)–(13)), depending on the temperature of the material, leading to a potential barrier. Consequently, the adsorption of an oxidizing gas increases the resistivity of WO_3 [299,300].

$$O_2 + e^- \rightarrow {O_2}^- \text{ (low temperature)} \quad (11)$$

$${O_2}^- + e^- \rightarrow 2O^- \text{ (medium temperature)} \quad (12)$$

$$O^- + e^- \rightarrow O^{2-} \text{ (high temperature)} \quad (13)$$

The formation of oxygen anions (Equation (13)) should be avoided (*via* the temperature control of the sensor) because of their tendency to be incorporated in the bulk of the material.

Recent studies about WO_3-based sensors are mainly dedicated to NO_2 detection (Section 6.2.1), but other gases are also considered (Section 6.2.2).

6.2.1. WO_3-Based Sensor for NO_2 Detection

Since WO_3 is an n-type semiconductor, NO_2 adsorption leads to anionic adsorbates on the surface of WO_3 according to reaction (14):

$$NO_2 \text{ (gas)} + e^- \text{ (from surface)} \rightleftharpoons NO_2^- \quad (14)$$

Han and Yin performed density functional theory (DFT) calculations to study the adsorption characteristics and electron transfer of nitrogen dioxide on O- and WO-terminated WO_3 (001) surfaces with oxygen vacancies [301]. It was found that NO_2 is (i) oxidized into nitrate on the bridging oxygen atom from an oxygen defect of the O-terminated WO_3 (001) surface and (ii) dissociated on a WO-terminated (001) surface: one oxygen atom from NO_2 fills the oxygen vacancy, and the resulting NO fragment is adsorbed onto a W atom. Both of these adsorption models are responsible for an increase in the electrical resistance of WO_3. In a very recent study, Yang et al. showed by in situ DRIFT spectroscopy that NO_2 and NO exhibit similar interaction with the surface of tungsten oxide; both nitrogen oxides were detected as oxidizing gases [302].

The structure/morphology of WO_3 is a key factor in the sensor response, and this topic is particularly developed in the recent literature. For instance, comparison of Ni-doped WO_3 nanowires and nanosheets shows that nanowires exhibited a rapid response time (66 s) but a slow recovery time (204 s) due to a low NO_2 desorption rate from the internal

porous structure of nanowires. On the contrary, the recovery time over nanosheets was shorter (126 s), thanks to a lower surface area and a less porous structure [303].

The effect of the structure on the sensor response for undoped WO_3 was also evidenced by Li et al. [304]. An enhancement of the gas sensing properties was obtained by the formation of self-assembled hierarchical hollow spheres. Such structure enhances the sensitivity to NO_2. At 140 °C, a response was recorded for NO_2 concentration of 18 ppb. This was attributed to a high specific surface area (7 m^2 g^{-1}) and to a wide range of pore size distribution (from 3 to 60 nm) that promotes the gas diffusion. Table 7 summarizes the latest developments in the synthesis of controlled undoped WO_3 structures for high-sensitivity NO_2 gas sensors (papers published in 2019–2020).

Table 7. Latest developments in the synthesis of controlled undoped WO_3 structures for high-sensitivity NO_2 gas sensors (papers published in 2019–2020).

WO_3 Structure/ Morphology	Detection Limit @ Optimal T	Remarks	Ref.
Nanoparticles (~40 nm)	100 ppb @ 25–50 °C	Ionic liquid-assisted synthesis, samples calcined at 500 °C for 2 h.	[305]
Microflowers assembled from nanoplates	125 ppb @ 105 °C	Outer diameters of ~2 µm, composed of nanoplates with the average pore size of 10.9 nm	[306]
Nanowire-assembled WO_3 nanomesh	50 ppb @ 160 °C	WO_3 nanomesh, assembled from single-crystalline WO_3 nanowires	[307]
Nanowires (2 nm)	930 ppb @ 100 °C		[308]
Nanosheets	300 ppb @ 100 °C	Comparison of monoclinic, triclinic and hexagonal WO_3 nanosheets; best performances obtained with triclinic WO_3	[309]
Mesoporous WO_3	60 ppb @ 500 °C	Diameter: 7 nm; specific surface area: 209 m^2 g^{-1}, prepared from SBA-15 as the hard template	[310]

Improvement in NO_2 detection can also be obtained by both tuning the tungsten morphology and creating interactions with a support. For instance, Ma et al. showed that tungsten oxide nanorods (diameters of 50–150 nm and lengths of 5–20 mm) supported on porous silicon (PS) had a good response to NO_2 and good recovery characteristics at room temperature. The lowest detected NO_2 concentration was 250 ppb [311]. The same authors also synthesized nanowires with diameters of 20–30 nm and lengths of 1–2 µm which were grown directly on the porous silicon through thermal annealing of tungsten film. The sensor responded well to NO_2 compared to other gases since the NO_2 response was three times higher for 2 ppm NO_2 than for 50 ppm NH_3, 100 ppm ethanol or 100 ppm acetone at 150 °C [312]. Modulations of the potential barriers at both homo- and heterojunctions between porous silicon and tungsten oxide were proposed to be responsible for the good sensibility at a low operating temperature (100 °C) [313]. Excellent gas-sensing behaviors were obtained with n-WO_{3-x}/n-PS nanocomposite prepared by sputtering tungsten oxide films on a high specific surface area porous silicon substrate [314]. This sensor exhibited an anomalistic p-type semiconducting behavior, which was supposed to improve the amplification effect of the heterojunction between WO_3 nanowires and the PS composites (PS forms p–n heterointerface with n-type WO_3 nanowires). The XPS analysis indicated the presence of large amounts of surface oxygen vacancies that directly contributed to the sensor response. NO_2 concentration as low as 30 ppb was then detected, and Figure 26 illustrates that the NO_2 selectivity vs. other gases was especially interesting. To improve the control of the WO_3 nanowire synthesis on silicon microelectromechanical systems (MEMS), Lee et al. recently developed a fabrication process by stress-induced method, in

which the growth position of the WO_3 nanowires can be controlled by patterning of the WO_3 seed film [315]. Finally, note that competition between different gases may influence the recovery time. For instance, WO_3 film demonstrated a longer recovery time towards NO_2 compared to NH_3 [316].

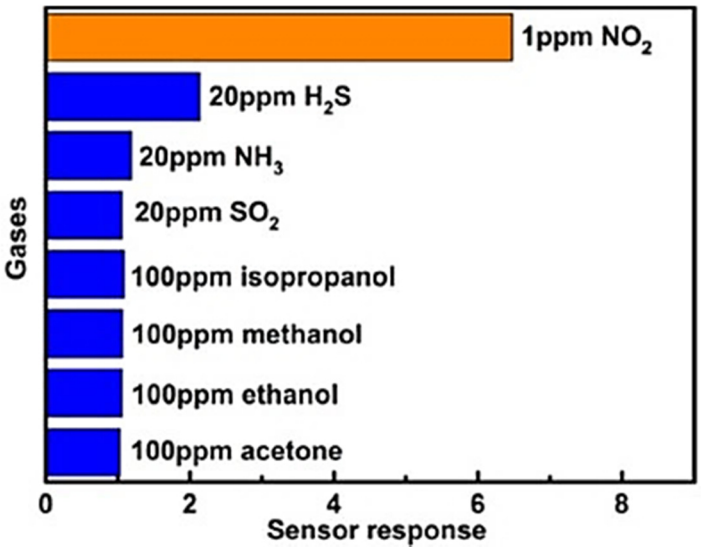

Figure 26. n-WO_{3-x}/n-porous silicon sensor responses to various gases at RT. From Li et al. [314] with permission from Elsevier.

Doped WO_3 sensors: Sensor improvement can also be obtained by WO_3 doping. The addition of precious metals to WO_3 is performed to improve the gas–sensor interaction, as well as the response and recovery times, and decrease the operating temperature. Gold is the most represented metal in the recently reported works, probably because Au-doped WO_3-based sensors exhibit overall enhancement in NO_2 sensing performances (response, detection limit and response/recovery times) [317,318] but also because they are only slightly affected by humidity. In fact, measurement in a humid atmosphere is one drawback of the semiconductor oxide-based sensors, and WO_3 is no exception [319]. Water adsorption leads to the oxidation of the WO_3 lattice because water fills the oxygen vacancies (*operando* DRIFT experiments), and consequently the resistance of the WO_3-based sensor increases [320]. The selectivity of the sensor is then affected, with lower signals toward NO_2 and higher sensor signals to CO. Sevastyanov et al. showed that water dependency can be virtually avoided by gold addition in the bulk and on the surface of WO_3. The conductivity in pure air of such Au/WO_3:Au material increased only 1.1–1.2 times when the absolute humidity raised from 2 to 16 g m^3 (it increases 6–7 times for Pt/SnO_2:Sb films in the same humidity range). Measurements with 0.45–10 ppm NO_2 showed that the Au/WO_3:Au sensor response did not depend on humidity [321]. This behavior toward humidity was confirmed on Au-WO_3 core–shell-structured nanospheres, associated with excellent NO_2 selectivity and long-term stability [322]. The significant performance improvement in NO_2 detection of Au/WO_3 compared to bare WO_3 was attributed by Hang et al. to a combined sensing mechanism: the surface Au nanoparticles dominated chemical sensitization while interbedded Au nanoparticles induced electronic sensitization [323]. An activation of Au/WO_3:Au thin films by laser diode radiation instead of constant heating was proposed by Almaev et al. [324] to reduce the response time to NO_2 by photodesorption. Moreover, holes generated in the near-surface region of WO_3 film by optical transitions were supposed to favor the photodesorption of chemisorbed O_2^- species, leading to the absence of response to reducing gases and change in oxygen concentration.

Results obtained with platinum-doped WO_3 appear possibly contradictory. Chmela et al. reported that platinum addition to WO_3 nanowires (<100 nm) caused detrimental effects, with lower sensitivity and selectivity toward NO_2 compared with the unfunction-

alized systems, associated with better sensing properties toward C_2H_5OH [325]. On the opposite, with nitrided WO_3 (WO_xN_y nanofibers), platinum addition enhanced the gas sensing characteristics by (i) lowering the operating temperature; (ii) enhancing the sensor reversibility at 50 °C; and (iii) exhibiting an exceptional selectivity toward NO_2 against interfering molecules such as C_2H_5OH, C_7H_8, CH_4, CO, NH_3 and NO [326].

Silver was also recently reported as a promising dopant. The optimal calcination temperature was found at 500 °C to obtain the larger response, better selectivity, faster response/recovery time and better long-term stability for NO_2 [327]. With 0.5%Ag-WO_3 [328], the sensor shows higher NO_2 sensing response at 200 °C and higher selectivity for NO_2 in the presence of different interfering gases (NH_3, acetone, SO_2, methanol, CO_2, NO). Significant decreases in gas responses were observed with high silver loading (5 and 10 mol%) because the silver crystallite size became too large and hindered their catalytic effects [329].

Comparing Ag-, Pd- and Pt-doped WO_3 nanoplates, Li et al. showed that Pd-WO_3 exhibited the highest response to NO_2 while Ag-WO_3 exhibited the fastest response speed [330]. The promotional effect of palladium was attributed by Liu et al. to the Schottky barrier between Pd and WO_3 [331].

WO_3-based sensors doped with other oxides have attracted little attention in the recent literature. Only a few recent studies report improvements of WO_3-based sensors by doping with oxides such as Sn, Sb and Fe. The main characteristics of these studies are summarized in Table 8. The observed improvements were generally attributed to an increase in the oxygen vacancies on the sensing surface.

Table 8. Oxide-doped WO_3-based sensors for NO_2 detection.

Sensor Material	Detection Limit @ Optimal T	Remarks	Ref.
RuO_2/WO_3 nanowires		Improved selectivity by enhancement of the electron depletion layer due to the formation of RuO_2/WO_3 Schottky junctions	[332] (2014)
Fe-doped WO_3 hollow nanospheres.	10 ppb @ 120 °C	The light distortion in the WO_3 crystal lattice by Fe doping produced interesting defects for gas sensing, with more oxygen vacancies	[333] (2018)
WO_3-In_2O_3 nanocomposites	@ 140 °C	Sol–gel preparation method; also active for CO detection at 240 °C	[334] (2019)
3D hierarchical structured Sb-doped WO_3	@ 30 °C	Improvement in NO_2 detection attributed to abundant structural defects derived from Sb doping, reduced bandgap and the 3D hierarchical microstructure	[335] (2018)
Sn-doped WO_3 nanoplates	5 ppb NO_2 @ 100 °C	Optimal loading: 2 wt.% Sn; introduction of Sn ions resulted in shorter response and recovery times, attributed to the increased number of oxygen vacancies on the sensing surface	[336] (2018)

6.2.2. WO_3-Based Sensors for Detection of Gasses Other Than NO_2

WO_3-based sensors were also investigated for the detection of gases other than NO_2. With this aim, only a few studies have dealt with undoped WO_3. Nanostructured WO_3 was evaluated for H_2S [337] or Cl_2 [338] detection, while thin film was found to be sensitive to acetone [339]. However, for this latest gas, a comparative study showed that SnO_2 is the best thin film compared to tungsten oxide or tin-doped tungsten oxide [340].

As described in Section 6.2.1, water adsorption on semiconductor oxides usually affects the measurements. However, this behavior can be used to develop sensors for relative humidity measurement. With this aim, WO_3 is usually associated with TiO_2 in the recently published studies. Zanettia et al. examined the influence of the WO_3 loading (0–10 mol%) on nanopowdered samples prepared by the polymeric precursor

method [341]. Best results in humidity measurements (in the 15–85% relative humidity range) were obtained with 2 mol% WO_3. This was attributed to the best compromise between the increase in acid sites and the mean pore size and pore size distribution. Faia et al. studied the influence of V_2O_5 doping for TiO_2-WO_3 sensors [342]. A p- to n-type transition still occurred for the doped sensors with the lower V_2O_5 content, while the sensor with the higher V_2O_5 content exhibited a typical n-type behavior with humidity increase. In addition, the electrical response to the relative humidity (10–100%) depended on the changes in the fabrication route (sintering temperature), which influences the final structure.

Section 6.2.1 also shows that NO_2 detection can be improved by the addition of precious metals to WO_3-based sensors. Nevertheless, these modifications are rather dedicated to the detection of reductant gases such as NH_3, H_2, H_2S and CO.

Palladium–WO_3 samples were prepared by spray pyrolysis by Gobole et al. The optimal palladium loading was found to be 3 wt.% Pd in WO_3 for the detection of NO_2, SO_2 and NH_3 at 100, 200 and 225 °C, respectively. For all of the studied gases, the response and recovery times for concentrations up to 750 ppm were fast, in the ranges of 0.5–1.25 s and 1–6.7 s respectively [343]. Tungsten trioxide nanowires decorated with iridium oxide nanoparticles resulted in remarkable changes in the morphology and defects of tungsten oxide nanowires. Such a sensor was found to be sensitive towards ethanol, NH_3, H_2, H_2S and NO_2 [344]. Tungsten oxide functionalized with gold or platinum nanoparticles was synthesized by Vallejos et al. using a single-step method via aerosol-assisted chemical vapor deposition. The metal additions allow the discrimination of C_2H_5OH, H_2 and CO gases, which are present in proton-exchange fuel cells. Particularly, Pt-functionalized tungsten oxide films allow H_2 detection at 250 °C, whereas nonfunctionalized tungsten oxide films detected low CO concentration (100 ppm) at a lower temperature (150 °C) [345]. Platinum–tungsten oxide can also be used to improve the CO electro-oxidation activity employed in the electrochemical sensor [346]. The interaction between platinum and tungsten oxide was enhanced by a reductive heat treatment, leading to a significant negative shift in CO oxidation potential. A portable CO sensor device built with $Pt/WO_x/C$ exhibited a higher sensitivity, faster response time and good linearity within 50 ppm CO, compared with a usual Pt/C-based sensor.

Xu et al. showed that triethylamine vapor is efficiently detected by $Ag/Pt/W_{18}O_{49}$ hybrid nanowire sensor, with a detection limit of 71 ppb. The ternary hybrid showed better behavior in detecting triethylamine than the binary $Ag/W_{18}O_{49}$ and $Pt/W_{18}O_{49}$ nanowires [347]. This excellent performance was attributed to the dual sensitization mechanism, i.e., a synergy of both electronic and chemical interactions.

Pt-catalyst-loaded tungsten oxide is also a good candidate for optical hydrogen gas sensor applications due to its gasochromic behavior (Pt/WO_3 turns blue in H_2 atmosphere while its electrical conductivity also changes). Yamaguchi et al. investigated the influence of partial pressures of hydrogen and oxygen gases on a Pt/WO_3-based sensor prepared by a sol–gel method [348]. Unfortunately, the optical absorbance of the film exhibited a nonlinear relationship with the H_2 concentration in absence of oxygen. However, the absorbance and electrical conductivity increased proportionally with the H_2 concentration in presence of oxygen, but both parameters strongly depended on the oxygen partial pressure. According to the relationship between the gasochromism and the oxygen concentration, the authors demonstrated that Pt/WO_3 is able to detect hydrogen gas concentrations in a low oxygen gas concentration atmosphere.

6.3. Conclusions

In summary, WO_3 is active in catalytic or photocatalytic oxidation of volatile organic compounds. Catalytic oxidation activity of WO_3 is linked to the presence of W^{6+}, W^{5+} and W^{4+} surface species generating reactive oxygen compounds. In supported catalysts, tungsten oxides promote the activity of the V_2O_5 active phase. Many pollutants are reported in studies considering the catalytic abatement of VOCs, such as formaldehyde, hexane,

trichloroethane, chlorobenzene, benzene, toluene and xylene. W-based samples are also largely studied for gas sensors, mainly in NO_2 detection. WO_3 is an n-type semiconductor, and its electrical conductivity varies with the oxygen concentration at the oxide surface. In addition, great recent efforts have been made in the development of the synthesis of controlled WO_3 structure/morphology for high-sensitivity gas sensors.

7. Pollutant Remediation in Liquid Phase (Photocatalysis)

The use of WO_3-based catalyst for pollutant remediation in liquid phase mainly concerns the oxidation of organic compounds via photocatalytic processes. Only a few recent studies have dealt with WO_3-based catalysts for non-photocatalytic application, such as H_2O_2 electrogeneration over $WO_{2.72}$/Vulcan XC72 gas diffusion electrode [349], hydrolysis of waste bottle PET in supercritical CO_2 assisted by acidic catalysis over WO_3-TiO_2 [350] or heavy metal ion adsorption on inorganic–organic hybrid WO_x–ethylenediamine nanowires [351]. However, this section is focused on the main use of tungsten-based catalysts in liquid phase, namely photocatalysis.

Compared to TiO_2, which responds only to UV light, WO_3 is visible-light-responsive. The bandgap between the valence band (VB) and the conduction band (CB) is 2.6–2.8 eV. However, bare WO_3 is not very active due to the fast recombination of photogenerated electrons and holes. Fortunately, the photocatalytic activity of WO_3 can be improved in five main ways: (i) the control of the WO_3 structure/morphology to obtain nanoporous structures with large surface area and fast pollutant diffusion; (ii) surface hybridization with graphene to obtain large specific surface areas and improvement in the charge transfer; (iii) coupling with other semiconductors (TiO_2) to enhance the photoinduced charge separation efficiency; (iv) doping by noble metal, which works as an electron pool and catalyzes O_2 activation.

WO_3 as a photocatalyst has been the subject of three recent reviews ("WO_3-based photocatalysts: morphology control, activity enhancement and multifunctional applications" by Dong et al. (2017) [352]; "Adsorptive removal and photocatalytic degradation of organic pollutants using metal oxides and their composites: A comprehensive review" by Gusain et al. (2019) [353]; "Tungsten oxide-based visible light-driven photocatalysts: crystal and electronic structures and strategies for photocatalytic efficiency enhancement" by Quan et al. (2020) [354]). Consequently, the section is mainly focused on the more recent studies. Evaluated molecules are mainly dyes, but other organics that are of major interest for water treatment are also considered, such as active molecules (medicinal and plant protection products) or pathogens.

7.1. Undoped WO_3 Photocatalysts

As previously introduced, bare WO_3 is poorly active as a photocatalyst, but structured/hierarchized WO_3 exhibits interesting behaviors. Monoclinic WO_3 phase was often reported as a suitable structure for photocatalysis. Noticeably, Xie et al. showed in 2012 that monoclinic WO_3 exhibits preferentially the suitable high-surface-energy {002} facet [355]. Indeed, the simple thermodecomposition of H_2WO_4 leads first to the cubic phase, but the monoclinic structure is formed with increasing time and/or temperature. After 30 min at 450 °C, the resulting WO_3 oxide shows 90% monoclinic phase [356]. The phase transformation is associated with a decrease in the specific surface area and an increase in oxygen vacancies. The electron transport is then improved, favoring the photocatalytic activity (ibuprofen removal by ozonation under visible-light radiation).

Various preparation methods have been developed to improve the WO_3 photocatalyst. Chen et al. evaluated different fuels (glycine, urea, urea and citric acid) to synthesize nanoscale tungsten oxides (nanoparticles, nanorods and nanoneedles) by the solution combustion synthesis method. Monoclinic WO_3 was obtained with urea, while a mixture of monoclinic $W_{18}O_{49}$ and WO_3 structures was obtained with glycine when the molar ratio glycine/ammonium paratungstate was 10 or higher. Such $W_{18}O_{49}$ + WO_3 mixture was also obtained with improved porosity using a mixture of urea and citric acid because the

reactants generated more gases and the combustion reaction was more vigorous (production of larger holes). Accordingly, this sample exhibited the best activity in methylene blue degradation [357]. Nanoparticles of monoclinic WO_3 can be also synthesized from Na_2WO_4 and PVP 70,000 (polyvinylpyrrolidone) as surfactant and template [358]. The synthesis was carried out at 180 °C in a Teflon autoclave. The best morphology for the photocatalytic efficiency in degradation of rhodamine B (RhB) under visible light was the block-shaped morphology. The authors proposed that the high photocatalytic efficiency could be attributable to the reducing activity of PVP which led to the formation of oxygen vacancies, beneficial for the capture of photoelectrons and the generation of superoxide radicals.

Monoclinic WO_3 nanoplates (100–170 nm in side length and 30–50 nm in thickness) can be also obtained by a one-step template-free hydrothermal route, from a mixture of aqueous solutions of $Na_2WO_4\cdot$ and HCl maintained at 180 °C for 12 h in an autoclave [359]. The optimal calcination set-up was found to be 600 °C for 2 h. The resulting catalyst allowed the degradation of rhodamine B with an activity 5 times higher than that of a commercial WO_3 powder. It was proposed that the high concentration of -OH species was responsible for the enhancement of photocatalysis.

However, the superiority of the monoclinic phase has been questioned very recently by Zhang et al. [360]. They studied the photocatalyzed degradation of rhodamine B (RhB) over monoclinic (m-WO_3) and hexagonal (h-WO_3) tungsten oxide. Samples were synthesized via acid precipitation process and decomposition of H_2WO_4 at different temperatures in air or N_2 to obtain oxidized or partially reduced oxidation states. After irradiation, the RhB removal efficiency classification was as follows: m-WO_3 (22%) < m-WO_{3-x} (48%) < h-WO_{3-x} (76%) $\leq$ h-WO_3 (80%). It is important to note that the specific surface areas of the hexagonal samples (52–55 $m^2\ g^{-1}$) were approximately twice those of m-WO_3. It also appeared that the impact of the oxidation state of tungsten was more significant for the monoclinic phase than for the hexagonal one. In fact, the impact of the hexagonal/monoclinic-WO_3 ratio (h/m) in the photocatalytic activity was clearly pointed out by Lu et al. [361]. To tune the h/m ratio, they used a sol–gel preparation method with K_2SO_4 as stabilizing agent and controlled calcination time and temperature. The observed optimal h/m ratio was close to 70/30, for which the activity in rhodamine B degradation was multiplied by a factor of 7.4 compared to pure m-WO_3. This improvement was attributed to the formation of a phase junction between h-WO_3 and m-WO_3, which exhibits high efficiency for the separation and transfer of photoexcited electron–hole pairs (electrochemical impedance measurements).

New innovative designs are also a way to produce efficient WO_3 photocatalysts. For instance, monoclinic nanocuboids, synthesized by hydrothermal treatment of commercial WO_3 with H_2O_2, showed high amounts of coordinative unsaturated W sites suitable for the photocatalytic degradation of methylene blue [362]. Other morphologies such as disk-shaped WO_3 (D-WO_3, monoclinic phase) were recently reported as attractive for acetic acid mineralization (after 0.1% Pt addition). To obtain such samples, aqueous solution of $(NH_4)_{10}W_{12}O_{41}\cdot$ was mixed with HNO_3 at 75 °C. After maturation, the resulting powder was calcined 3 h at various temperatures to vary the physical properties. As expected, the crystallinity of D-WO_3 increased with the calcination temperature while the specific surface area decreased. The highest photocatalytic activity was obtained with the sample calcined at 600 °C [363]. Another recent approach was to design a single tungsten atom oxide photocatalyst, supported on poly(ethylene oxide), as shown in Figure 27a [364]. In this case, the photogenerated electron transfer process is enabled by an electron in the spin-up channel excited from the highest occupied molecular orbital to the lowest unoccupied molecular orbital +1 state, which can only occur with single tungsten atom oxide with W^{5+} (Figure 27b). The resulting catalyst exhibited a degradation rate of 0.24 s^{-1} for dyes (methyl orange, methyl red, dimethyl yellow; mechanism illustrated in Figure 27c for methyl orange), which is two orders of magnitude higher than those of available photocatalysts. Additionally, the reactions between oxygen with photogenerated electrons ($e^- + O_{2ads} \rightarrow O_2{}^-\bullet$) and between adsorbed water and photogenerated holes ($h^+ + H_2O_{ads} \rightarrow H^+ + OH_{ads}\bullet$) produce reactive oxidizing species such as superoxide anions ($O_2{}^-\bullet$), hydrogen

peroxide (H_2O_2) and hydroxyl radicals (OH•). Reactive oxidizing species are responsible for the degradation of aqueous organic compounds, besides the direct decomposition of organic compounds with photogenerated holes.

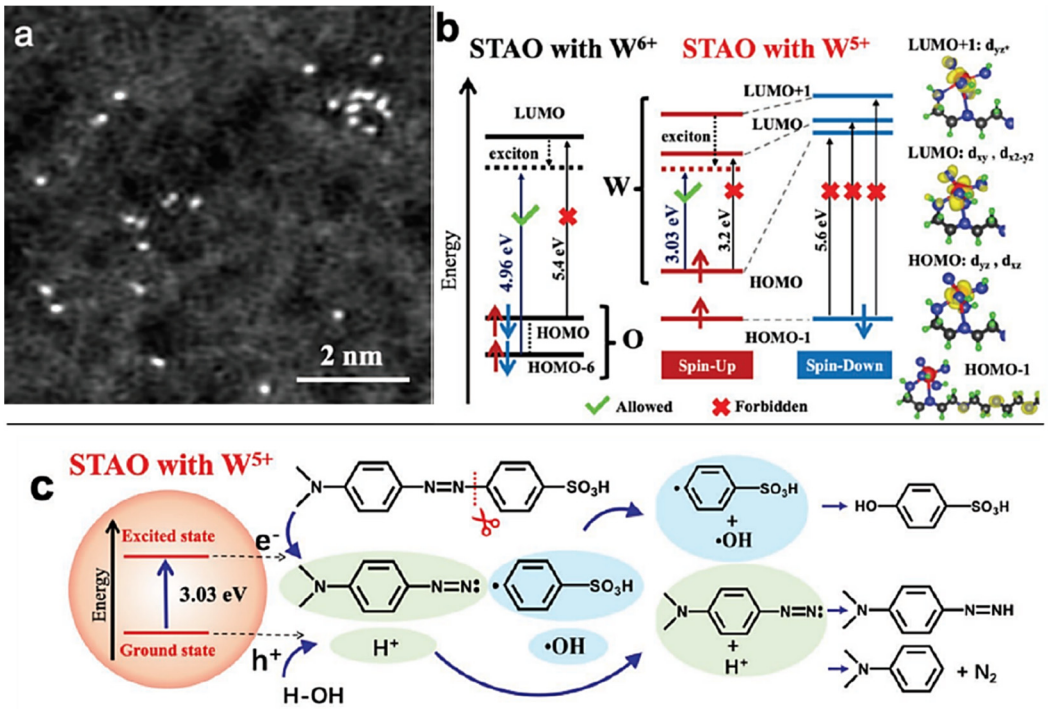

Figure 27. (**a**) A Cs-corrected STEM-HAADF image showing monodispersed single tungsten atoms. (**b**) TD-DFT calculated the occupations and transitions between states in W^{6+} (left part) and separately in W^{5+} (middle part). Arrows ↑ and ↓ denote spins. Dashed lines connect spin-up and -down channels in the same band. The HOMO, LUMO and LUMO+1 bands for W^{5+} have been decomposed (right part) according to the tungsten atomic orbitals. (**c**) Photocatalytic degradation reaction (methyl orange): upon photoexcitation, the hole dissociates an H_2O into H^+ and ·OH. The electron cleaves a C-N bond in the azo-benzenesulfonic group. The resulting H^+ then reacts with 4-(2λ2-diazenyl)-N,N-dimethylaniline (green) to form N,N-dimethylaniline, while the ·OH reacts with benzenesulfonic acid radical (blue) to form p-hydroxy benzene sulfonic acid. From [364] with permission from John Wiley and Sons.

It is important to note here that dye decolorization and mineralization have to be distinguished. This point is highlighted for instance in the paper of Cheng et al. about the treatment of effluent from oil palm agroindustry with tungsten oxide photocatalysts [365]. With the optimum catalyst loading (at 0.5 g/L), the decolorization reached 96.2% but the mineralization reached only 51.1%.

To improve the efficiency of treatment by photocatalysis, tungsten oxide can be also used as a photoelectrocatalyst, i.e., implemented at the surface of a photoanode. The idea is to promote the photoelectron transfer to dissolved oxygen, which is a drawback of WO_3 photocatalysis. To enhance charge separation, electrochemical and photocatalytic techniques can be used together. Zheng et al. synthetized nanoporous, monoclinic WO_3 photoanodes from a tungsten foil (0.1 mm thickness) that was anodized at 50 V in 0.25 wt.% HF electrolyte and subsequently annealed at 500 °C. It was showed that methyl orange mineralization rate was higher in photoelectrocatalysis (at E = 1 V vs. SCE in NaH_2PO_4 electrolyte) than in photocatalysis or electrocatalysis [366], as illustrated in Figure 28. The high efficiency of the WO_3 photoelectrocatalyst was also demonstrated for the abatement of pathogens such as *Escherichia coli* [367].

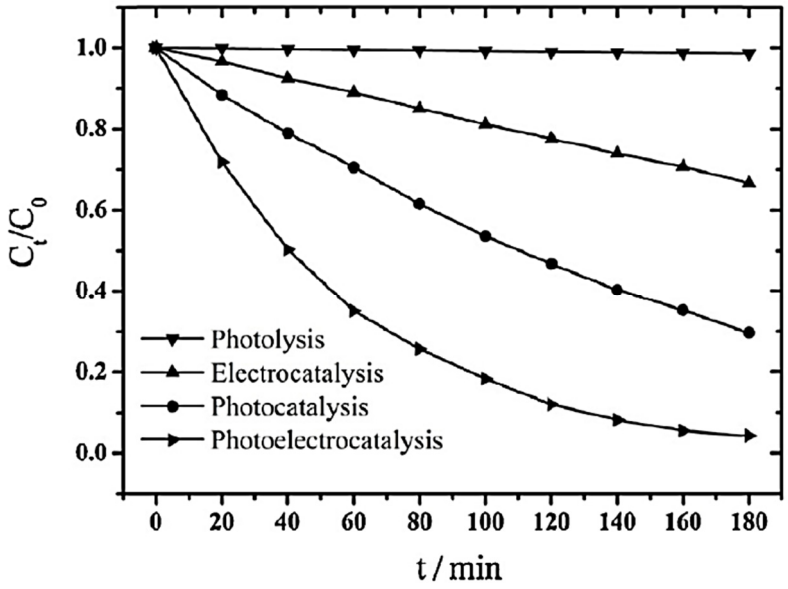

Figure 28. Methyl orange degradation rate by different processes. Experimental set-up: nanoporous monoclinic WO_3 anode, irradiating intensity of 0.1 W cm^{-2} (xenon lamp), oxidation potential of 1 V vs. SCE (NaH_2PO_4 electrolyte). From Zheng et al. [366] with permission from Elsevier.

7.2. WO_3–Carbon Photocatalysts

As previously mentioned, the fast electron–hole recombination is a major drawback of WO_3 for photocatalysis application. In addition to the synthesis of structured WO_3 with controlled morphology, another way to improve the photocatalysis efficiency is to associate WO_3 with carbon-based materials that exhibit interesting high specific surface areas. Among the various possible structures of carbon-based materials, graphene appears the most popular. Preparation of WO_3–graphene composite can be performed by different methods. Recent studies reported techniques such as the electrospinning technique to obtain a porous tungsten oxide nanoframework with graphene film [368]; a one-pot synthesis, first mixing sodium tungstate and nitric acid and then adding tetraphenylporphyrinn, graphene and citric acid (final calcination in the 350–550 °C temperature range) [369]; or a method based on pulsed laser ablation in liquid phase: WO_3 nanoparticles suspended in water were mixed with a suspension of monolayer graphene and irradiated for 30 min by the pulsed laser beam of 355 nm. During the laser irradiation, the photoinduced electrons in the WO_3 reduced graphene, and WO_3 nanoparticles were anchored on the graphene sheets [370].

The synthesized film reported in [368] showed the ability to adsorb aromatic molecules, extensive light absorption range, significant light trapping and efficient charge carrier separation properties. Consequently, this sample allowed a high activity in the photodegradation of rhodamine B compared to bare WO_3 and TiO_2 nanomaterials.

The in situ prepared nanocomposites made of tetraphenylporphyrin/WO_3/reduced graphene [369] showed specific surface areas around 450 m^2g^{-1} and spherically shaped nanoparticles of monoclinic WO_3 when the appropriate tetraphenylporphyrin loading and calcination temperature of 350 °C were used. The visible radiation absorption was confirmed with a bandgap energy of 2.14 eV. The photocatalytic degradation rate of 20 ppm Acid Blue 25 was 85% in 3 h at pH = 4 (UV–Vis and TOC analyses). This behavior was attributed to the visible-light absorption properties and to the high separation rate of photogenerated charge carriers. Similar conclusions were obtained with the samples prepared by the pulsed laser ablation evaluated in methyl blue degradation [370]: WO_3-reduced graphene samples showed much better visible-light absorption and less photogenerated charge recombination than pure WO_3.

Other carbon-based materials were also recently developed. Amorphous carbon-coated tungsten oxide was obtained via pyrolysis of hybrid polyoxometalates (hybrid POMs) in nitrogen atmosphere [371]. Compositions, microstructures and concentrations of oxygen vacancies were closely related to the species of organic amines in the hybrid POMs. The presence of defects (oxygen vacancy) was responsible for the improvement in the degradation of dyes (methylene blue, methyl orange and rhodamine B) compared with WO_3 or TiO_2 photocatalysts.

WO_3/carbon nanotube (CNT) nanocomposites were proposed by Isari et al. for the abatement of tetracycline (antibiotic) and other pharmaceutical wastes in water [372]. Samples were synthesized via a sol–gel method (aqueous sodium tungstate + lactic acid + CNT+ HCl; the obtained gel was then transferred in an autoclave for 30 h at 190 °C). The characterization techniques demonstrated the incorporation of CNTs into the WO_3 framework and an efficient reduction in charge carrier recombination rate compared to the corresponding WO_3 catalyst without CNT. The pollutant remediation was performed coupling visible light and ultrasound (US) irradiations (sono-photocatalysis). Ultrasonic irradiation favors HO• formation, mainly via water decomposition. It was found that 60 mg/L tetracycline could be perfectly degraded with the following set-up: WO_3/CNT: 0.7 g L^{-1}; pH = 9; US power: 250 W m^{-2}; light intensity: 120 W m^{-2}; duration: 60 min. Trapping experiment results verified that HO• radicals and h(+) were the main oxidative species.

7.3. WO_3 Photocatalysts Doped by Precious Metals or Silver

As previously mentioned, the restricted application of tungsten oxide (WO_3) is due to its low conduction band. Tungsten trioxide (WO_3) is an n-type semiconductor with a small bandgap (Eg 2.6–2.8 eV). Consequently, WO_3 has a limited ability to react with electron acceptors such as oxygen and has a high recombination rate of the photogenerated electron–hole pairs. Therefore, great attention has been paid to develop novel visible-light-driven WO_3-based photocatalysts, and special attention has been paid to the crystal facet engineering of WO_3 nanocrystals (Section 7.1). Additionally, doping with noble metal (Section 7.3.1) or silver (Section 7.3.2) is an effective way to enhance the absorption of sunlight and improve the photocatalytic efficiency together with material phase/morphology design to generate oxygen vacancies.

7.3.1. WO_3 Photocatalysts Doped by Precious Metals

Abe et al. [373] proposed the enhancement of photocatalytic properties of WO_3 by loading Pt, which can trap electrons photogenerated from WO_3. The use of Pt as an electron scavenger on WO_3 nanorods was also investigated in [374]. Platinum nanoparticles were loaded on WO_3 nanorods with various mass ratios (0.1, 0.2 and 0.3) via a photoreduction process (PRP). The photocatalytic activity in aerobic oxidation of alcohols reached up to 98% for Pt/WO_3 and 69% for WO_3, while no oxidation was observed in the absence of light. The highest photocatalytic performance was obtained for the mass ratio of 0.2. This enhancement in the photocatalytic activity after platinum loading was attributed to an extended lifetime of the generated electron–hole pairs compared to WO_3 support. Additionally, Gunji et al. [375] reported the importance of controlling the metal deposition site on the photocatalyst surfaces to optimize the use of the photoexcited electrons and holes without the recombination of photogenerated carriers during the photochemical decomposition of organic pollutants. The authors proposed a cocatalyst based on the site-selective deposition of PtPb nanoparticles on oxidation sites and deposition of Pt nanoparticles on reduction sites. The synthesized PtPb/Pt/WO_3 exhibited higher photocatalytic performance for the decomposition of acetic acid under visible-light irradiation ($\lambda > 420$ nm) than that observed using the conventional photodeposited Pt/WO_3 or chemically deposited PtPb/WO_3.

Platinum doping was also evaluated on tungsten trioxide for catalyzed oxidation reaction [289] or as an electrode for direct methanol fuel cells (DMFCs) [376]. Pt/WO_3 catalyst layers were prepared by electrosynthesis of WO_3 on a graphite (Gr) support. It was reported that the corresponding Pt/WO_3/Gr electrode has higher catalytic activity for

methanol oxidation than a commercial Pt/C catalyst. Interestingly, methanol oxidation is enhanced under visible-light illumination, which is attributed to both a synergy between Pt and WO_3 active sites and the simultaneous occurrence of methanol photooxidation at WO_3 sites.

7.3.2. WO_3 Photocatalysts Doped by Silver

The surface plasmon resonance (SPR) effect greatly contributes to enhancing the visible-light absorbance of catalysts by allowing resonant photons at the metal–dielectric interface to resist the restoring force of positive nuclei [377]. The SPR effect of silver was investigated by Ding et al. [378]. By studying the relationships between the locations of silver nanoparticles on different facets of hexagonal WO_3 nanorods and the photocatalytic performance of the photocatalyst, Ding et al. reported that both the intrinsic nature of charge separation on the {001} facets of WO_3-110 nanorods and the SPR effect contribute to the enhancement of visible-light absorption and the decrease in the recombination of the photogenerated electron−hole pairs. The highest efficiency in the degradation of methyl orange (MO) was obtained with 4.5 wt.% Ag/WO_3 photocatalyst presenting dominant exposed {001} facets compared to {100} or {010} ones. A mechanism was proposed where photons are absorbed under visible-light irradiation and photogenerated electrons and holes are subsequently produced by a facet surface transfer, as summarized in Figure 29.

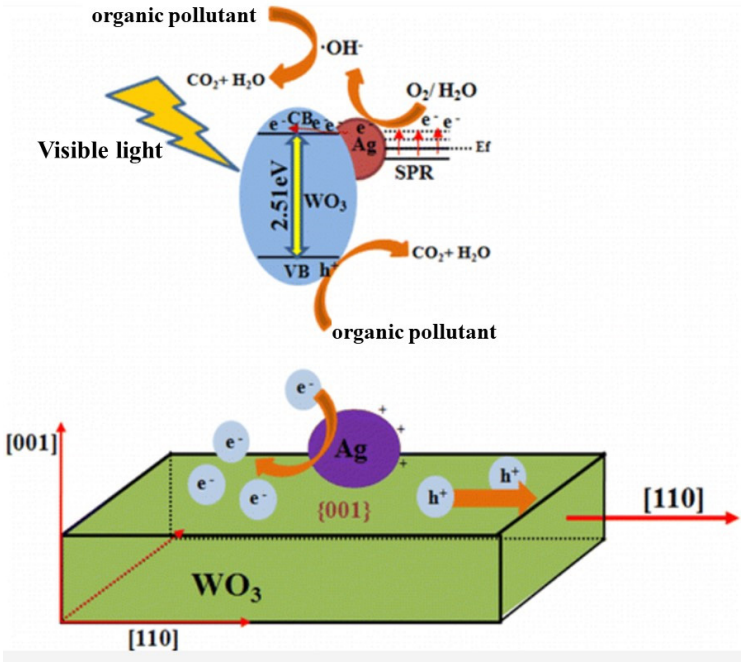

Figure 29. Possible degradation mechanism of MO over 4.5 wt.% Ag/WO_3 photocatalyst under visible-light irradiation. From [378] with permission from the American Chemical Society.

The crucial role of oxygen defects was investigated by Wei et al. [379]. Tungsten oxide (WO_{3-X}) is a transition metal oxide that has rich substoichiometric compositions and possesses oxygen defects involved in photon–electron interactions. In combination with silver nanowires (Ag NWs) presenting surface plasmon resonance properties, the incident photon-to-electron conversion efficiency is enhanced together with the methylene blue (MB) photodegradation performance. In fact, the electron concentration in WO_{3-X} depends mainly on the stoichiometric defect concentration. This means that oxygen deficiencies play a critical role in the decay of localized SPR phenomena.

Morphology and properties of Ag-WO_3 hierarchical materials were also investigated by Capeli et al. [380] for the degradation of rhodamine B (RhB) dye under 467 nm LED light irradiation. Three-dimensional WO_3 catalysts decorated with silver nanoparticles (Ag NPs)

were prepared by a one-step hydrothermal method in the absence of surfactant (WO_3•Ag). The amount of Ag NPs is an important factor in the formation of various novel and complex WO_3 3D hierarchical architectures, from 3D irregular-platelet-like building blocks, which evolve into 3D hexagonal building blocks, to three-dimensional hexagonal-football-like and finally to 3D multibranched spiky ball-like microcrystals. The WO_3•0.20Ag 3D hierarchical structure presented higher photodegradation of RhB dye solution compared to the individual WO_3 3D material. This result was assigned to an engineering heterojunction between Ag NPs and WO_3 semiconductor, which could enhance the light absorption (more photoexcited electrons) and suppress the photogenerated electron–hole pair recombination. Ag NPs act as an electron reservoir. Under light, photogenerated electrons (e^-) in the valence band (VB) are excited to the conduction band (CB), and electrons from the reservoir on the Ag NPs could be trapped by O_2 molecules to generate superoxide radical ($•O_2^-$) species. Concurrently, a similar number of holes (h^+) are generated in the valence band (VB), which are able to react with H_2O or OH^- molecules to generate OH• radicals. Similar results were achieved by Gao et al. [381], who used silver to improve the properties of the WO_3. Ag nanoparticles (Ag NPs) were reported to enhance the production of negative oxygen ions ($•O_2^-$ radicals) under visible light by the prepared Ag/WO_3 catalysts supported on wood. More precisely, Ag NPs redistribute the charge carriers, which could trap the photogenerated electrons and inhibit the recombination of excited electrons and holes (Figure 30).

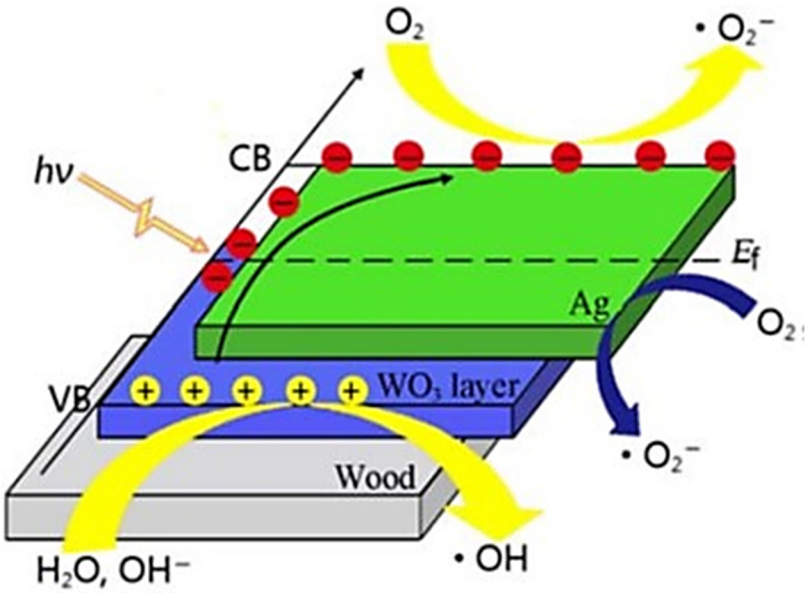

Figure 30. Schematic illustration of the mechanism of negative oxygen ion production upon the Ag/WO_3–wood. From [381] with permission from Elsevier.

Promising plasmonic Ag/AgCl photocatalysts have been recently investigated. The SPR effect of silver is responsible for the broadened absorption in the visible-light region, and these properties were expanded to WO_3. For instance, Ma et al. [382] prepared Ag–AgCl/WO_3 hollow spheres with a flowerlike structure that had superior visible photocatalytic activity because of their unique morphology. Adhikari et al. [383] also observed a photocatalytic activity enhancement of Ag/AgCl/WO_3 powder prepared by a microwave-assisted hydrothermal method. However, most WO_3/Ag/AgCl photocatalysts reported were in powder form, thus having limited use in practical applications because tedious regeneration is required. Consequently, Fang et al. [384] prepared WO_3/Ag/AgCl films on a conventional glass substrate to reduce the regeneration cost. The WO_3 film was prepared on a glass substrate by calcination of spin-coated W precursor. Ag/AgCl particles were then deposited on WO_3 film by an impregnation–precipitation–photoreduction method. Excellent photocatalytic performances were obtained in the degradation of methyl orange

(MO) and rhodamine B (RhB) under visible light. It is proposed that Ag and AgCl greatly promoted the separation of photogenerated electron–hole pairs and improved the charge transfer efficiency of WO_3. Based on the photoelectrochemical test and radical trapping measurement, a Z-scheme mechanism for $WO_3/Ag/AgCl$ is proposed where $\bullet O_2^-$ and h^+ play the major roles in photodegradation, while the effect of OH• could be neglected (Figure 31a). Consequently, Z-scheme composite photocatalysts have to be considered as an effective way to enhance the photocatalytic performance of catalysts. Li et al. [385] proposed plasmonic $Ag/Ag_2WO_4/WO_3$ Z-scheme visible-light composite photocatalyst for the degradation of rhodamine B, methylene blue and methyl orange. A possible Z-scheme mechanism of the ternary composite was proposed under visible light where Ag particles produce SPR effect but also work as the charge transmission bridge (Figure 31b).

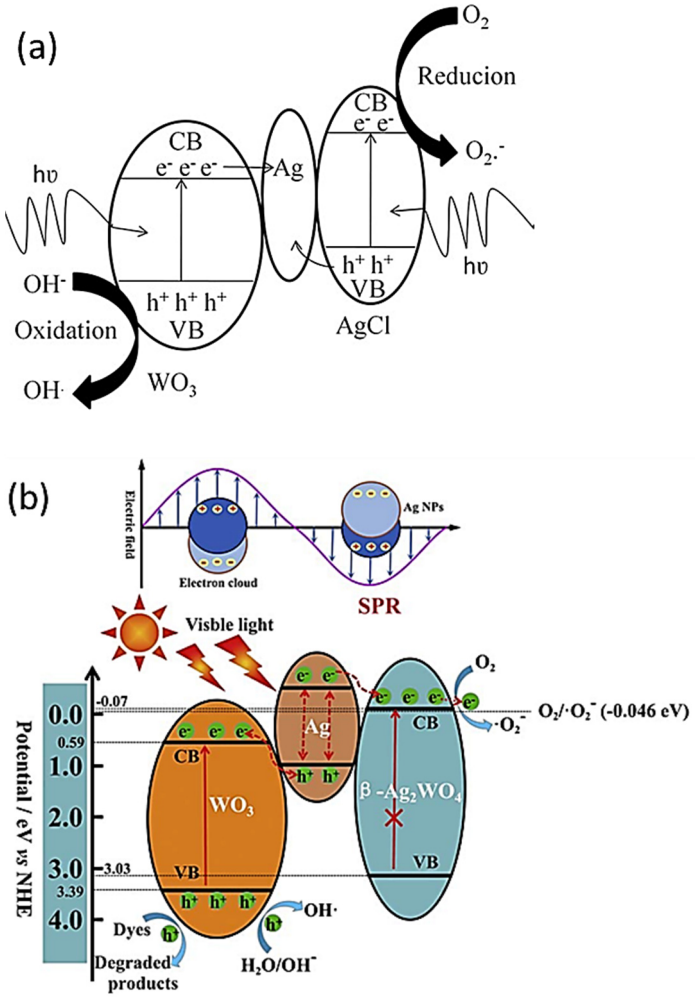

Figure 31. (**a**) The possible photocatalytic mechanism of organic pollutant degradation on $WO_3/Ag/AgCl$ film under visible-light illumination. From [383] with permission from Elsevier. (**b**) Schematic illustrating the proposed photocatalytic mechanism over the $Ag/\beta\text{-}Ag_2WO_4/WO_3$ photocatalyst. From [385] with permission from Elsevier.

Sahoo et al. [386] designed a Z-scheme WO_{3-X}-Ag-ZnCr layered double hydroxide (LDH) photocatalyst for tetracycline degradation, based on the SPR effect of metallic Ag as redox electron mediator. The defects created by surface oxygen vacancy in WO_{3-X} and the existence of Ag as electron transfer conductor facilitate the charge pair separation efficiency and enhance the photocatalytic activity.

7.4. WO_3–TiO_2-Based Photocatalysts

Because of the poor activity of WO_3 due to its rapid electron–hole recombination, coupling with other semiconductors to use the sunlight as a free light source is an attractive research area. Concomitantly, titanium dioxide (TiO_2) is an interesting material for applications in the purification of air and water by removal of recalcitrant organic and inorganic pollutants such as synthetic dyes, phenols and chlorophenols, volatile organic compounds, detergents, solvents, heavy metals or pharmaceutical antibiotics.

Unfortunately, due to the size of TiO_2 bandgap (Eg 3.0–3.2 eV), bare TiO_2 only works in conjunction with irradiation of limited wavelength (λ_{irr} < 385 nm) corresponding to ultraviolet (UV) light that accounts for only 6.8% of the solar spectrum, thus limiting its photocatalytic activity. The visible (Vis) range (400–760 nm) accounts for about 38.9%, and infrared radiation (IR, 760–3000 nm) makes up most of the remaining 54.3% [387]. In addition to the ability of materials to absorb solar spectrum, the effectiveness of photocatalytic systems also depends on the sample capacity to separately collect photogenerated electrons and holes. The high electron–hole recombination rate limits the photocatalytic performance of bare TiO_2. Consequently, several approaches were devoted to improving the photocatalytic performance of titania, especially by coupling with other semiconductors. The objective is to increase the separation of charge carriers by doping titania with metal oxide presenting both conducting band (CB) and valance band (VB) of higher or equal energy compared to TiO_2. Among the many possibilities, the addition of crystalline tungsten oxide (WO_3) has interesting advantages. Its shorter bandgap (Eg 2.6–2.8 eV) compared to TiO_2 (Eg 3.0–3.2 eV) requires longer wavelengths for the excitation and extends the photoresponse of TiO_2 to the visible light region. The coupling with WO_3 also induces energy levels enabling the electrons photogenerated in the conducting band of TiO_2 to transfer into the CB of WO_3. Consequently, the photopromoted holes can diffuse from the CB of WO_3 into the valence band of TiO_2. The surface acidity of the TiO_2 catalyst can also be increased by adding WO_3, which facilitates the adsorption of OH^- or H_2O molecules and targeted molecules on TiO_2 and thereby improves the photocatalytic activity of TiO_2. WO_3–TiO_2 combination also induces dark activity due to the energy storage ability of tungsten oxide.

WO_3–TiO_2-based systems exist as (i) tungsten oxide doping of supported or hybrid materials (Section 7.4.1) and (ii) metal doping of WO_3–TiO_2 materials (Section 7.4.2).

7.4.1. WO_3–TiO_2-Based Systems as Supported and Composite Photocatalysts

The photocatalytic activity of a WO_3–TiO_2 system is largely determined by its structure, which is significantly influenced by the preparation method of the catalyst. Consequently, both WO_3 supported (WO_3/TiO_2) and composite (TiO_2/WO_3) materials are described.

Supported photocatalysts. Dyes such as methylene blue, rhodamine B or methyl orange are often chosen as model pollutants, but the degradation of several other contaminants has also been evaluated. For instance, Gao et al. [388] obtained WO_3/TiO_2 material with high surface area and unique morphology by synthesizing heterostructured photocatalysts from wood fibers through a two-step hydrothermal method and a calcination process. The wood fibers acted as carbon substrates, allowing the recombination probability of photoexcited charge carriers to be reduced, and also increased the transport of charges. It results in high performance of the WO_3/TiO_2–wood fibers as a UV-light or a visible-light photocatalyst for degradation of rhodamine B, methylene blue, methyl orange or phenol. Ding et al. [389] also observed a photoinduced electron–hole separation effect over tungsten oxide (WO_3)/TiO_2 core–shell nanowires for the degradation of rhodamine B. The degradation of RhB was also undertaken over WO_3/TiO_2 and MoO_3/TiO_2 composites [390]. The reduction of the electron–hole recombination rate by coupling TiO_2 with tungsten oxide or molybdenum oxide led to high photocatalytic activity. The 5 wt.% WO_3/TiO_2 composite was the more efficient sample due to the more efficient separation of charge carriers. The electron migration from the conduction band (CB) of TiO_2 to the WO_3 CB can

be offset by O_2 and produces superoxide radical (O_2•) and hydrogen peroxide (H_2O_2) and finally hydroxyl radical (OH•) to decompose RhB (Figure 32).

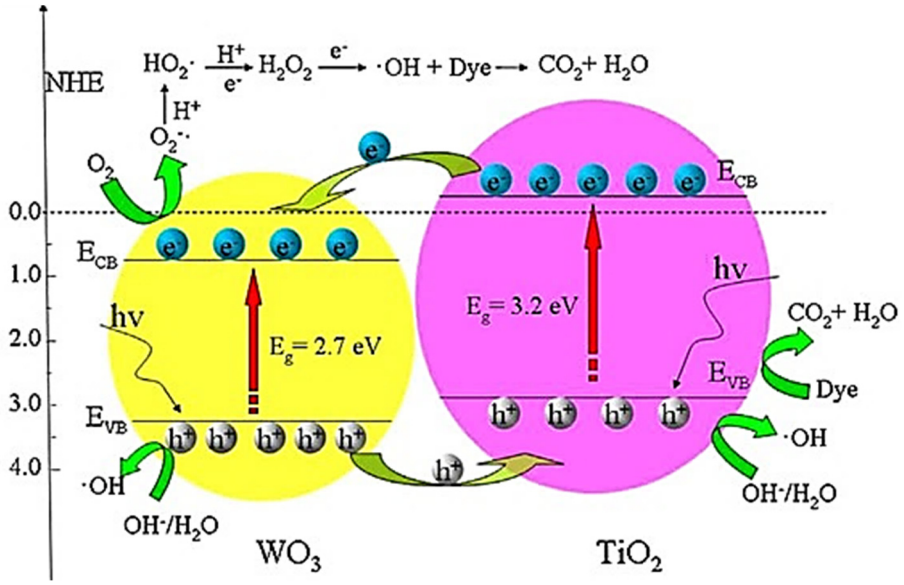

Figure 32. Proposed mechanism of dye degradation in visible light by WO_3/TiO_2 composite. From [390] with permission from Elsevier.

Yang et al. [391] synthesized porous WO_3/TiO_2 hollow microspheres by a spray drying method. The authors observed that the tungsten oxides mainly existed in a highly dispersed amorphous form on anatase when the loading amount of tungsten oxide was below 3 mol%. The improved photocatalytic activity in methylene blue and phenol photodegradation under UV-light irradiation over the WO_3/TiO_2 catalyst mainly arises from the enhanced charge separation efficiency provided by the acidity induced by WO_3 addition, rather than the improved light absorbance by highly dispersed amorphous tungsten oxides.

WO_3/TiO_2 materials, designed as nanocomposites, mixed oxides or supported photocatalysts, were also used to degrade malathion pesticide [392], imazapyr [393], sulfamethoxazole [394] or formic acid [395]. For instance, 2% WO_3/TiO_2 prepared by sol–gel method showed excellent photocatalytic performance, achieving complete malathion degradation after 2 h [392]. Synthesis of mesoporous WO_3–TiO_2 nanocomposites presented interesting behavior for imazapyr herbicide degradation under visible light and UV illumination. The overall photocatalytic efficiency of the 3% WO_3–TiO_2 nanocomposite was 3.5 higher than for mesoporous TiO_2 [393]. The WO_3–TiO_2 nanocomposite showed both monoclinic and triclinic WO_3 structures. Tungsten-promoted composite catalysts were also envisaged by Ioannidou et al. [394]. Experiments showed that the 4% W-TiO_2 catalyst calcined at 700 °C was the most active for sulfamethoxazole degradation (350 μg/L) under simulated solar irradiation, enhancing the rate of pristine TiO_2 by 50%. Tungsten is believed to act as a trap of electrons, thus reducing the rate of electron–hole recombination and, consequently, increasing degradation rates. The addition of electron acceptors, such as hydrogen peroxide and sodium persulfate, in the reaction mixture also improved the catalyst activity. Photoactivity of WO_3–TiO_2 mixed oxides prepared by a sol–gel method was tested under UV–visible irradiation in both the mineralization of formic acid in aqueous suspension and the gas phase oxidation of acetaldehyde [395]. The catalyst containing a 3% W/Ti molar ratio gave the best results, due to the formation of an intimately mixed oxide resulting in a better charge separation due to the migration of photoproduced holes from WO_3 to TiO_2. WO_3 supported samples were also synthesized using liquid phase plasma process for degradation of diethyl phthalate [396]. The best degradation performance was observed for bare TiO_2 photocatalyst under UV light source, but modified TiO_2 photocatalysts showed a 1.7–6.2 times higher degradation rate under blue light.

Composite photocatalysts. Composite (or hybrid) TiO_2/WO_3 materials are another strategy to obtain an enhancement in the photon absorption and a dark activity due to both the storage of photogenerated electrons and a redox process. Khan et al. [397] prepared microsized hybrid TiO_2/WO_3 samples (TWx; x is 0.025, 0.5, 0.075, 0.1 molar ratio of W precursor) by sol–gel and crash precipitation methods followed by spray drying. Evaluated in the photocatalytic degradation of methylene blue (MB), the hybrid $TW_{0.075}$ was reported as the most active material, with 90% of dye degradation reached in 100 min with dark runs. It was reported that TiO_2 and WO_3 acted in synergy to increase the lifetime of electron–hole pairs and to decrease the recombination rate by electron diffusion from CB of TiO_2 to WO_3. The authors proposed a mechanism for the transfer pathways of the photogenerated charge carriers in the hybrid powders (TWx) (Figure 33) where both hydroxyl radicals (OH•) and superoxide anions (O_2^-) play a major role.

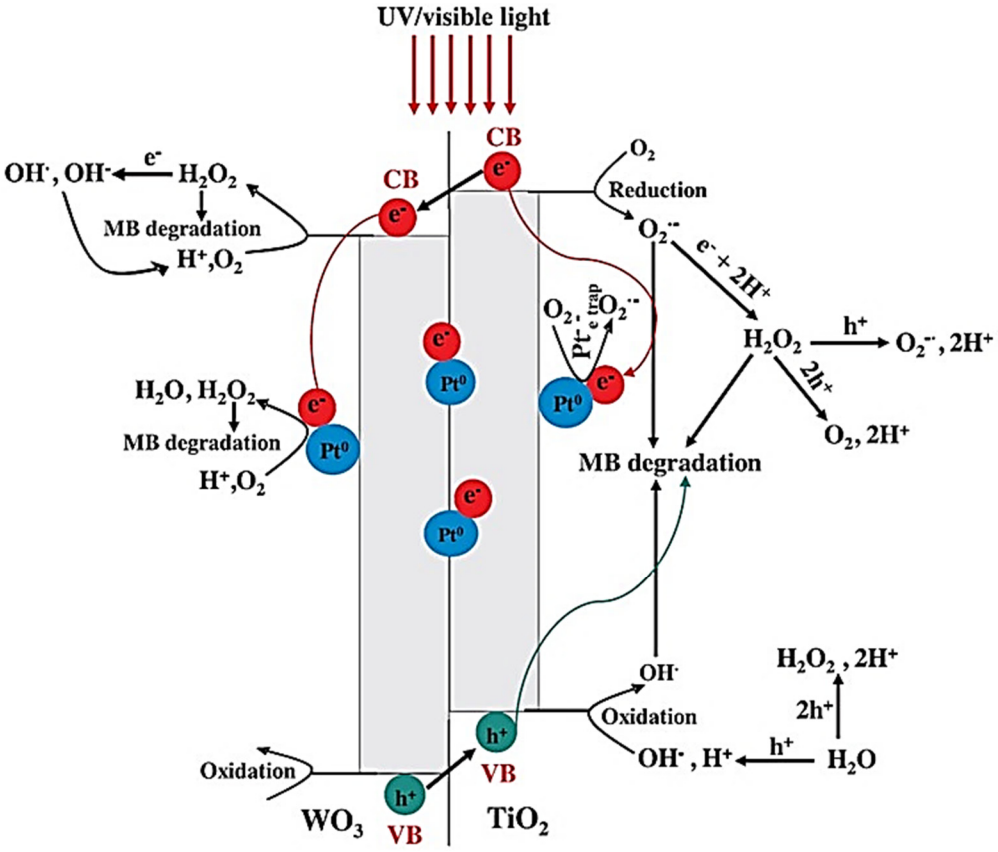

Figure 33. Proposed mechanism illustrating the transfer pathways of the produced charge carriers and various oxidizing species contributing to the degradation of MB. From [397] with permission from Elsevier.

TiO_2/WO_3 systems (TW) were also studied by Rimaldi et al. for ethanol and tetracycline (TC) degradation [398]. Analyses supported the parallel occurrence of several TC degradation pathways in the case of TW samples in which OH• radicals are involved, as previously mentioned in [397] for MB conversion. TiO_2-WO_3 composites were also evaluated for bisphenol A (BPA) oxidation under simulated solar light [399]. A core–shell system composed of a layer of TiO_2 nanoparticles on the surface of WO_3 nanowires was also evaluated as an effective photocatalyst in the degradation of RhB [389]. Again, the photoinduced electron–hole separation effect between WO_3 and TiO_2 contributed to the improvement of the photocatalytic activity.

WO_3-TiO_2 photocatalytic systems can be also associated with other processes to obtain overall improvements. With the aim to associate photocatalysis with electrochemistry, WO_3

was associated with a TiO_2 nanotube array to obtain a photoanode designed to improve photoelectrocatalytic (PEC) performance for the degradation of methylene blue [400]. A synergistic vacancy-induced self-doping effect and localized surface plasmon resonance (LSPR) effect were observed, confirming the importance of oxygen vacancies in improving PEC performance.

WO_3–TiO_2-based catalysts were also evaluated for photocatalytic-assisted ozonation of pollutants. A 4% WO_3/titanate nanotube composite catalyst allowed the complete removal of emerging contaminants such as caffeine, metoprolol and ibuprofen in municipal wastewater in less than 40 min with TOC removal up to 64% after 2 h. Compared to bare TiO_2, WO_3 addition induced a higher activity under visible-light radiation and an increase in the adsorption capacity of organic compounds [401].

7.4.2. Metal-Doped WO_3–TiO_2-Doped Systems

To decrease the fast electron–hole recombination and improve the interfacial charge transfer process of WO_3–TiO_2 materials, the addition of noble metals or heteropolyoxometallates (POMs) has been successfully explored.

Noble metals act as a sink of conduction band photoinduced electrons, avoiding their recombination and enhancing the photocatalytic process. Thus, TiO_2–WO_3–Au systems were evaluated by several authors. X-ray diffraction (XRD) data and Raman spectroscopy measurements usually indicated that TiO_2 is mainly in anatase structure, while the WO_3 can be amorphous or crystallized. Gold nanoparticles improve the material's response in the visible domain [402]. Kovács et al. [403,404] studied the structural peculiarities of TiO_2/WO_3/Au materials. It was shown that each minor structural change in bulk or surface has a significant impact on the photocatalytic activity and intermediate formation dynamics, using phenol as a model pollutant. However, the gold deposition mode was found crucial over structural peculiarities, especially for W species. The resulting sample presented three WO_3 forms in different proportions: amorphous, crystalline and doped. These forms manifested in different species (W^{6+}, W^{4+}, $W_{defects}$), which critically influenced the activity and the intermediate formation during the photodegradation. Consequently, gold-containing samples resulted in a modification of structural particularities, but the correlation between structural features and PCA or intermediate formation was strongly dependant on the synthesis pathway [404].

Platinum addition is reported to enhance the electron storage ability, the visible activity and the electron–hole separation of photocatalysts by the creation of Schottky-type junctions, thus facilitating the charge transfer at the catalyst–environment interface [405]. By varying the platinum amount from 0.2 to 1 wt.% in Pt/TiO_2-WO_3 materials prepared through the spray drying method, the optimum amount for the degradation of methylene blue (MB) was found at 0.8 wt.% Pt. Hydrogen peroxide (H_2O_2) and hydroxyl radicals (OH•) were found as the main species responsible for the aqueous degradation of the model pollutant. TiO_2 maintained its tetragonal anatase phase and WO_3 maintained its monoclinic structure. The corresponding $Pt_{0.8}$TW sample presented the lowest electron–hole recombination rate (photoluminescence measurements) and the highest amount of surface hydroxyl groups (FTIR experiments).

The use of heteropolyoxometallates (POMs) is another interesting way to decrease the fast electron–hole recombination on TiO_2. POMs act as effective traps of photoinduced electrons, leading to visible-light-absorbing materials with high photocatalytic activity. Tungstosilicic acid (TSA; $H_4SiW_{12}O_{40}$) was successfully used by Rengifo-Herrera et al. [406] to obtain the formation of a surface complex between the Keggin structure of TSA and the TiO_2 surface, or the formation of Keggin–TSA/TiO_2 composites. It resulted in visible-light absorption of modified catalysts. The photocatalytic activity in the degradation of 4-chlorophenol depends on the TSA amount. FT-IR and FT-Raman characterizations indicated that the main heteropolyoxometallate species presented in the composites was the $[SiW_{12}O_{40}]^{4-}$ anion, which exhibited a strong interaction with the TiO_2 surface.

7.5. WO_3 Associated with Transition Metal Oxides Other Than TiO_2 (Zn, Fe, Sn, Mn, Ni, Mo, Co, Nb)

In view of photocatalytic activity enhancement of WO_3 catalysts, doped materials have attracted much attention, and the present section focuses on the modification of tungsten(VI) oxide by transition metal oxides (MOs). In fact, by coupling WO_3 with another semiconductor, an improvement of charge separation in photoinduced charge transfer processes of *n*-type semiconductor is expected, leading to a drop in electron–hole (e^-/h^+) pair recombination and an increase in photocatalytic activities.

7.5.1. ZnO–WO_3

Among the multitude of oxides considered, zinc receives great attention owing to its high light sensitivity and wide bandgap energy (3.37 eV). However, the photocatalytic activity of zinc oxide is limited to the ultraviolet light range of the solar energy spectrum, representing only 5–7% of the total sunlight energy. Another limitation is the rapid recombination of the electron–hole (e^-/h^+) cavity. To overcome these issues, surface modification of the structures of the ZnO nanoparticles has been proposed. The aim is to alter the bandgap energy, thus shifting the absorption band to the visible region in semiconductor systems. Doping ZnO by WO_3 enables the electrons produced from ZnO to be trapped, thus preventing the fast recombination of electron–hole pairs and increasing the photocatalytic activity. WO_3 has the advantage of narrow bandgap energy (2.2–2.8 eV), which could activate the zinc oxide. Such ZnO-WO_3 materials can act as good candidates for the degradation of Direct Blue 15 (DB15) or methylene blue (MB) dye, organophosphorus pesticides such as diazinon, diclofenac and bacterial or fungal strains.

Zinc oxide nanoparticles doped with 0.5% to 2% WO_3 were synthesized by hydrothermal method to obtain samples where W was added into ZnO structure [407]. Photocatalytic activity for diazinon removal was reported to reach 99% for 2% WO_3-doped ZnO catalyst after 180 min of contact time. This result was attributed to a reduction in the network constant. Similar tungsten oxide doped ZnO nanoparticles were evaluated in the photocatalytic degradation of Direct Blue 15 [408]. Numerous parameters, namely pH, light intensity, dopant percentage, dye concentration and contact time, affect the process. It appeared that acidic pH resulted in higher efficiencies of the photocatalytic process. In addition, increasing the concentration of the WO_3 dopant percentage from 1 to 5% *w*/*v* increased the degradation rate from 30.7 to 73.1%. Tungsten acted as a recombinant mediator of interfacial charge transfer, which resulted in a change in the photocatalytic efficiency of the doped ZnO. Sajjad et al. [409] revealed that the formation of Zn-O-W linkage was responsible for a redshift of the absorption peak to the visible region, resulting in a lower bandgap and a promotion of the separation of photogenerated carriers. In fact, the proposed energy state configuration showed dissimilar locations of conduction and valence bands of both semiconductor oxides in ZnO/WO_3 composites. Due to a narrowing of the bandgap, the charge separation is facilitated and the rate of recombination is significantly reduced, resulting in improved photodegradation efficiency. In addition, the transfer of charge carriers due to the narrow bandgap can be confirmed by OH• radical measurement as proposed by Mugunthan et al. [410] for the degradation of diclofenac with ZnO-WO_3 mixed oxide catalysts. Authors observed higher hydroxyl radical (OH•) generation when coupling ZnO and WO_3 compared to bare ZnO. The benefit of the coupled system is mainly due to optimal loading of WO_3 since good dispersion of WO_3 in coupled oxides promotes the formation of heterojunction structures between the two coupled oxides. The optimal molar ratio of Zn:W = 10:1 was found for the degradation of diclofenac.

Photocatalytic activity of Zn-doped WO_3 (Zn-d-WO_3) nanoparticles for antifungal and antibacterial degradation was studied by Arshad et al. [411]. Zn loading from 0.1 to 0.3% had a significant impact on both antibacterial/antifungal photocatalytic degradation and structural/morphological properties. Characterizations showed that the Zn-d-WO_3 structure was triclinic, the particle shape was a mix of spheres and rods and the particle size was decreased as the Zn concentration increased from 0.1 to 0.3%. Photocatalytic activity of Zn-WO_3 was evaluated in methylene blue (MB) dye degradation. Again, Zn

loading impacted the activity. The maximum dye degradation rate was achieved with Zn(0.3%)-WO_3 sample, at 78% and 92% with 120 min of contact time for visible and UV irradiation, respectively. Again, it was proposed that after the generation of electron–hole pairs (e^-/h^+), the electronic vacancies or holes in the valence band are promoted due to the migration of electrons from the valence band to the conduction band. As a consequence, electron–hole pairs generate hydroxyl radicals (OH•) and superoxide ions ($•O_2^-$) that act as powerful oxidizing agents to mineralize the dye into CO_2 and H_2O.

Novel Pd/$ZnWO_4$ nanocomposite materials for photocatalytic degradation of atrazine were evaluated by Al-Amshany et al. [412]. Photocatalytic activity of $ZnWO_4$ was highly affected by the insertion of Pd into the composition. Palladium was reported to replace W in the $ZnWO_4$ lattice leading to a sample presenting low bandgap, low electron–hole pair (e^-/h^+) recombination rate and high BET surface area. Consequently, high photocatalytic activity for atrazine degradation was obtained for 1.65 wt.% Pd/$ZnWO_4$ nanocomposite, with 100% of degradation after 60 min of reaction time.

7.5.2. MO–WO_3 (MO: Metal Oxides = Fe, Sn, Mn, Ni, Mo, Co)

Other transition metal oxides such as Fe, Sn, Mn, Ni, Mo and Co were evaluated in the past few years to improve the photocatalytic activity of WO_3. Metal oxides act as electron sinks to capture the photoinduced electrons through their low energy trapping sites; they then reduce the electron–hole recombination and enhance charge separation.

Fe_2O_3 is a visible-light-driven material with a bandgap energy of 2.0–2.3 eV and a CB of 0.46–0.77 eV. Wang et al. [413] proposed a new active $FeWO_4/Fe_2O_3$ di-modified WO_3 for the degradation of methylene blue (MB), toluidine blue (TB), azure I (AI) and acridine orange (AO) under visible-light irradiation. Beneficially, Fe^{2+}, which is classically involved in the Fenton reaction favors the generation of OH• radicals and subsequent organic dye degradation. Over $FeWO_4/Fe_2O_3$-modified WO_3 sample, $FeWO_4$ and Fe_2O_3 acted as electron traps. Consequently, a valence decrease of Fe^{3+} to Fe^{2+} led to the capture of photoexcited electrons of WO_3 and enabled the Fenton reaction in the presence of trace H_2O_2. Consequently, di-modified WO_3 samples showed high photocatalytic activity compared to bare WO_3. This assisted Fenton process was also described by Mwangl Ngigi et al. [414] for photocatalytic degradation of Methylparaben (MeP) over Fe-doped WO_3 nanoparticles in presence of H_2O_2. The best formulation was 5 wt.% Fe-WO_3, with 50.8% MeP degradation in the presence of H_2O_2. A hydroxyl radical mechanism was advanced to explain the efficiency and enhancement of iron-doped WO_3 on visible-light activity of the organic pollutant removal.

SnO_2 is also used for bandgap tuning of nanomaterials to transform UV-light-active catalysts into visible-light-driven catalysts. Nevertheless, tin dioxide has a wider bandgap of 3.6 eV (UV-light-driven catalyst) with a high recombination rate of its photogenerated electron–hole pairs, which limits its use. These drawbacks can be overcome by tungsten doping to serve as a photogenerated charge trap, thus decreasing the recombination rate of e^-/h^+ pairs by the reduction of the bandgap. In this way, Ullah et al. [415] reported that tungsten-doped SnO_2 (W@SnO_2) nanospheres can be a preferred choice for visible light photocatalytic degradation compared to standard TiO_2 (Degussa-P25). With the increase in the W content from 0 to 6 $_{mol}$%, the bandgap of SnO_2 was tuned from 3.6 to 2.8 eV, and the degradation of crystal violet dye reached 100% after 40 min of contact time.

The formation of a nanocomposite of WO_3 with manganese oxides is also a way to reduce the bandgap of tungsten oxide. The constitution of composite with Mn, indigo dye and reduced graphene oxide (RGO) was investigated by Ahmad et al. [416] as visible light photocatalyst for methylene blue (MB) dye removal. A synergetic association between WO_3 and RGO was observed which increased the rate of charge transfer and limited the recombination of electron–hole pairs in the nanosized composite. As a consequence, the so-called Mn/indigo/RGO/WO_3 presented improved photocatalytic performance compared to Mn/indigo/WO_3.

Well-crystalline NiO-WO_3 nanoparticles were synthesized by Rosaline et al. [417] for the photocatalytic degradation of eosin yellow (EY) dye. A photocatalytic degradation rate of 95% was obtained after 180 min under visible-light irradiation. The authors proposed that photogenerated electrons of NiO possibly migrate into the conduction band of WO_3. Simultaneously, the holes move in the opposite direction, which greatly decreases the recombination of electron–hole pairs.

Mo-doped WO_3 nanowires for adsorbing methylene blue (MB) dye from wastewater were evaluated by Silveira et al. [418]. Samples presented hexagonal structure (h-WO_3), and the Mo doping led to a change in morphology of h-WO_3 nanowires from large bundles to narrow bundles when Mo loading increased from 4 to 15 $_{at}$%. In fact, Mo^{6+} and W^{6+} have similar ionic radii and electron structures, which enables Mo to directly incorporate the crystalline lattice of WO_3 to form a $Mo_xW_{1-x}O_3$ structure. As a consequence, the bandgap of WO_3 can be reduced by substituting W by Mo in order to improve the photocatalytic activity with visible light, as demonstrated in [419]. In addition, Mo-doped WO_3 samples also exhibited a considerable improvement in MB adsorption capacity [418].

The reduction in electron and hole recombination of WO_3 can also occur with nanocomposites of cobalt(II, III) oxide and tungsten(VI) oxide. The synthesis of p–n heterojunction catalysts, such as Co_3O_4/WO_3, was claimed to enhance the photoactivity under UV- or visible-light radiation [420]. The strong reduction in photoexcited electrons and holes resulted in the enhancement in diclofenac sodium degradation. The highest degradation efficiency was obtained for 0.02 M of cobalt acetate (CW2), with 98.7% achieved for the degradation of 15 ppm diclofenac sodium at pH 10.7. Higher generation of hydroxyl radicals (OH•) associated with the enhancement of effective charge separation was still advanced to explain the high photocatalytic activity of the CW2 sample. Figure 34 shows the charge transfer proposed by Malefane et al. [420] and the p–n heterojunction formed to minimize photoexcited electron and hole recombination in CW2 nanocomposite.

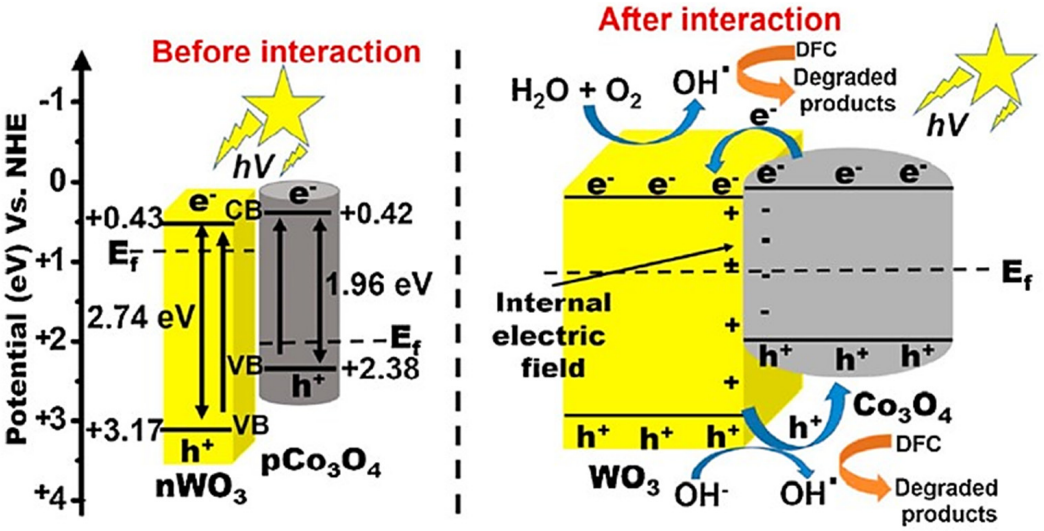

Figure 34. Proposed degradation mechanism in Co_3O_4/WO_3 p–n heterojunction. From [420] with permission from Elsevier.

7.6. WO_3 Associated with Other Systems (Post-Transition Metal Oxides and Metalloids, Rare Earths, Nitrides)

7.6.1. Post-Transition Metal or Metalloid–WO_3 Systems

Among the post-transition metals, bismuth and gallium were evaluated in recently published works.

Bi_2WO_6/perylene diimide (PDI) composite photocatalyst was prepared and evaluated in phenol oxidation (and water decomposition to produce oxygen) under visible light [421]. Compared to the self-assembled perylene diimide and Bi_2WO_6, the composite showed an enhancement in the phenol degradation because the positions of conduction and valence

bands between Bi_2WO_6 and perylene diimide favored the separation of the photogenerated carriers. The Bi_2WO_6/PDI composite exhibited an n–n-type heterojunction.

$BiFeWO_6/WO_3$ nanocomposites were studied by Priya et al. [422]. Various $BiFeWO_6$ loadings from 1 to 3 wt.% deposited on WO_3 nanorods were prepared by simple coprecipitation and hydrothermal treatment. Pure $BiFeWO_6$ bandgap was measured at 2.0 eV, and the best photodegradation of rhodamine B under visible-light illumination was obtained with 1% $BiFeWO_6/WO_3$ This sample exhibited a bandgap of 2.3 eV, while the bandgap increased to 2.9 eV for 3% $BiFeWO_6/WO_3$.

The influence of the partial substitution of gallium by tungsten in a $Ga_2Zr_2O_7$ fluorite-type nanosized material was recently examined in crystal violet degradation [423]. $Ga_2Zr_{2-x}W_xO_7$ samples with x = 0, 0.05, 0.1, 0.15 and 0.2 were prepared using the citrate technique. $W_{0.15}$ substitution (optimal loading) allowed the shift of the absorption range to the visible-light range by decreasing the bandgap from 4.95 eV for $Ga_2Zr_2O_7$ to 1.7 eV for $Ga_2Zr_{0.85}W_{0.15}O_7$. The crystal violet photocatalytic degradation rate was then multiplied by 20 (optimum operating conditions: pH = 9, 1 g L^{-1} catalyst, reaction duration of 300 min). Complete degradation was obtained with the addition of 25 mmol L^{-1} hydrogen peroxide. O_2 center dot and holes were found to have a more important role in $Ga_2Zr_{2-x}W_xO7$ systems compared with HO center dot.

The excellent semiconductor tungsten selenide WSe_2 was recently used as quantum dots (particle size: 7–8 nm) and associated with nitrogen-doped graphene oxide to prepare a composite photocatalyst by the mechanical stripping method [424]. The degradation of methylene blue under visible light with the composite (optimal WSe_2 loading: 4.7 wt.%) was better than WSe_2 and nitrogen-doped graphene oxide (N-GO) alone. The photocatalytic degradation rate of 50 mL at 1×10^{-4} mol·L^{-1} dye with only 0.01 g catalyst reached 93% after 1 h light exposure (300 W Xe lamp with a cutoff wavelength of 420 nm; reaction was monitored by a total organic carbon analysis).

7.6.2. Rare Earth–WO_3 Systems

Cerium is a very popular component in redox catalysis thanks to its ability to vary between Ce^{III} and Ce^{IV}. Impregnation of 1 to 25 wt.% of Ce^{3+} ions onto WO_3 led to a better absorption cross-section and a redshift in the band edges [425]. The decrease in the photoluminescence emission intensity and the suppression of the Raman active bands of WO_3 indicated the recombination quenching ability of Ce surface states. For low cerium loading ($\leq$5%), cerium was mainly found as Ce^{III}, while Ce^{IV} was predominant for higher loadings. An enhancement in the charge retention ability was observed with the Ce loading increase. In comparison to pure WO_3, Ce-doped catalysts exhibited superior activity for 2-nitrophenol and 2-chlorophenol removal in natural sunlight exposure. For low cerium loadings, the surface oxygen bonded with Ce^{III} serves as electron trapping and transfer centers, while the synergic composite mechanism is the dominating mode for high Ce loading [425].

Tahir et al. evaluated various other rare earths (REs) by doping WO_3 with La, Gd and Er (RE molar contents of 2, 4 and 6%). Samples were obtained by coprecipitation at 80 °C in acidified aqueous solution. Photocatalytic activity was measured in degradation of dyes (methyl orange, methyl blue, crystal violet), antibiotic (tetracycline) and antimetabolite (methotrexate) and compared to a 10% carbon nanodots–WO_3 reference sample [426]. La, Gd and Er did not enter into the crystal lattice of WO_3 (monoclinic and hexagonal phases) but were positioned in the interstitial sites, with La-O-W, Gd-O-W and Er-O-W bonds. The photocatalytic activity order was as follows: 2% Gd-WO_3 > carbon nanodots–WO_3 > 4% Er-W > 4% La-W > undoped WO_3. The best photocatalytic performance achieved with 2% Gd-WO_3 could be attributed to its higher surface area, the inhibition of the charge-carrier recombination, the high surface hydroxyl content and the extended visible-light absorption region.

7.6.3. Nitride–WO_3 Systems

The graphite-like carbon nitride (g-C_3N_4) is a metal-free polymer that is an n-type semiconductor. Its structural and physiochemical behaviors give it interesting properties in electrical and optical fields. The g-C_3N_4-based nanostructures are emerging materials for energy and environmental photocatalytic applications (e.g., photocatalytic water reduction and oxidation, degradation of pollutants, carbon dioxide reduction) [427].

Xiao et al. prepared Z-scheme WO_3/g-C_3N_4 composite hollow microspheres by controlled in situ hydrolysis and a polymerization process (Na_2WO_4 in deionized water with the addition of dicyandiamide $C_2H_4N_4$ and glucose; the homogenized solution was then transferred into an autoclave and heated 200 °C; for 20 h; after centrifugation and washing, the product was finally annealed at 550 °C; for 3 h in air (Figure 35)) [428]. The shell of the hollow microspheres consisted of well-distributed WO_3 and g-C_3N_4 nanoparticles, favoring heterojunctions with numerous interfaces and highly exposed oxidation–reduction active sites. Various contents of g-C_3N_4 were evaluated, and the best results were obtained with a molar loading of 4% dicyandiamide with respect to W. The lifetime of the charge carriers reached 2.23 ns, which is obviously prolonged compared to WO_3. This optimized Z-scheme system maintained the redox potential of the components. Combined with the long lifetime of holes and electrons, this photocatalyst showed enhanced degradation rates towards tetracycline hydrochloride (antibiotic agent) and ceftiofur sodium (antibacterial agent).

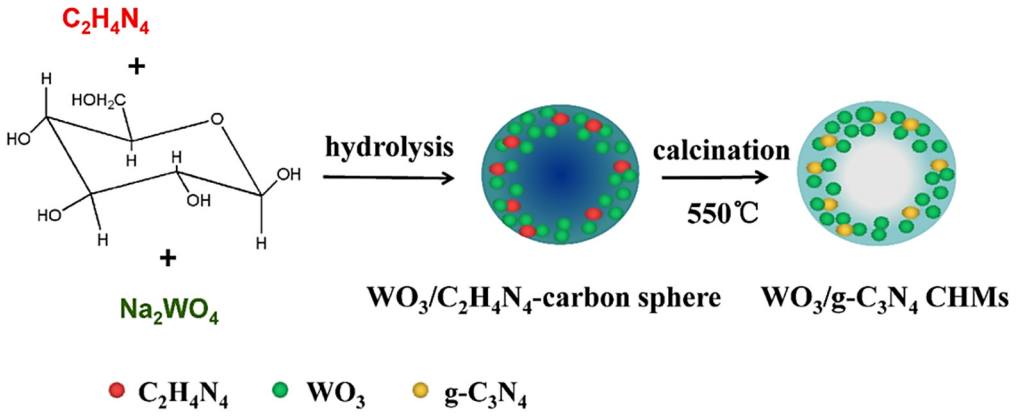

Figure 35. Scheme of the in situ construction of WO_3/g-C_3N_4 composite hollow microspheres (CHMs). From [428] with permission from Elsevier.

g-C_3N_4/WO_3 materials can be also shaped as thin films for water purification [429]. A bilayered structure has to be formed to ensure an enhanced charge carriers' separation. Trapping experiments performed under UV illumination revealed that the activation of the photocatalytic oxidation of methylene blue (MB) came from both holes and superoxide radicals.

Other nitrides such as tantalum nitride (Ta_3N_5) were also recently evaluated in dye degradation. Ta_3N_5 is one of the few visible-light-absorbing photocatalysts capable of overall water splitting (OWS). Ta_3N_5/$W_{18}O_{49}$ nanocomposite fibers were prepared by the solvothermal technique to obtain a catalyst made of orthorhombic Ta_3N_5 nanoparticles and monoclinic $W_{18}O_{49}$ nanowires. This sample showed a doubled degradation rate of rhodamine B under white light compared to Ta_3N_5 nanoparticles alone [430]. In fact, $W_{18}O_{49}$ allowed dye adsorption before illumination. Using tert-butanol and p-benzoquinone as scavenger agents, it was demonstrated both hydroxyl and superoxide radicals contributed to the cleavage of rhodamine B. The superoxide species were involved in N-deethylation of the dye. The generation of both radical species on $W_{18}O_{49}$ was due to the electronic transfer between $W_{18}O_{49}$ and Ta_3N_5. Taking into account the recycling ability of the catalyst and

the simplicity of the synthesis process, the authors propose that this catalyst is a good candidate for the scale-up.

7.6.4. Photoreduction over WO_3 Based Systems

Photocatalytic water treatment is mainly focused on the oxidation of organic pollutants. However, due to its high toxicity, Cr^{VI} species reduction into Cr^{III} is also a major concern. g-C_3N_4/WO_3 thin-film materials presented in the previous section also exhibited Cr^{6+} elimination behavior under UV illumination [429]. The Cr^{6+} reduction rate was 6% and 93% after 120 min illumination for WO_3 and g-C_3N_4/WO_3, respectively. In opposition with photocatalytic oxidation of methylene blue for which active species came from both holes and superoxide radicals, the main active species for chromium reduction are electrons.

For the same chromium reduction, Thwala et al. evaluated the doping of WO_3 by 1, 3 and 5 $_{mol}$% of magnesium (one-pot preparation method) [431]. A slight increase (0.0069 nm) of d spacing was observed by HRTEM imagery after Mg addition, according to a decrease in the bandgap energy and a shift in the edge positions, also confirmed by XPS analysis (0.08 eV). The rate of recombination was greatly reduced upon doping (photoluminescence analysis). DFT calculations supported the recombination reduction rate due to the introduction of the Mg orbital. With 500 mL at 9.5 ppm Cr^{VI} maintained at pH = 1 and a catalyst weight of 0.1 g, 97% Cr^{VI} reduction rate was reached with 3 $_{mol}$% Mg-WO_3 after one hour under visible-light irradiation (990 W Xe lamp).

7.7. Conclusions

WO_3-based photocatalysts benefit from a visible-light response due to a 2.6–2.8 eV bandgap between the valence band (VB) and the conduction band (CB). The challenge is to avoid the fast recombination of the photogenerated electrons and holes of bare WO_3 by doping or promotion (with carbon, metal(s), TiO_2, etc.). Depending on the reaction conditions, the formation of reactive oxidizing species such as superoxide anions (O_2^{-}•), hydrogen peroxide (H_2O_2) and hydroxyl radicals (OH•) is reported. The WO_3-TiO_2 system is of great interest for extending the photoresponse of TiO_2 (Eg 3.0–3.2 eV) to the visible light region since the electrons photogenerated in the conducting band of TiO_2 can transfer into the CB of WO_3. The photopromoted holes can thereafter diffuse from the CB of WO_3 into the valence band of TiO_2.

8. Conclusions

Tungsten oxide materials exhibit suitable behaviors for surface reactions and catalysis such as acidic properties (mainly Brønsted sites), redox and adsorption properties (due to the presence of oxygen vacancies) and a photostimulation response under visible light. The bandgap of WO_x is commonly stressed to 2.6–2.8 eV for crystallized WO_3 3D structures but grows up to 5.5 eV for isolated WO_4 species (such as bi-grafted, di-oxo WO_4 surface sites) or supported WO_x catalysts depending on the loading. From the operating conditions of the catalytic process, each of these behaviors is tunable by (i) controlling structure and morphology (nanoplates, nanosheets, nanorods, nanowires, nanomesh, microflowers, hollow nanospheres, etc.), (ii) thermal treatment under controlled atmosphere and (iii) interactions with other compounds (such as conductors (carbon), semiconductors (e.g., TiO_2) and precious metals); WO_x particles can be also dispersed on high specific surface area support. Based on these behaviors, WO_3-based catalysts were developed for environmental applications. One of the major advantages of the acidic and redox behaviors of WO_{3-x} is their suitability for the abatement of NO_x from stationary sources, associated mainly with TiO_2 and V_2O_5 (nitric acid plants first; treatment of incinerator and other combustion gases nowadays). WO_3-based catalysts also promote the abatement of some VOCs. Moreover, surface oxygen vacancies are also useful in the development of gas sensors, especially for NO_2 detection. Modifications are suitable to improve sensibility, selectivity, stability, repeatability and response time. Besides, the recent literature shows a high interest in WO_3-based materials for photocatalysis applications. Bare WO_3 is not very active due

to the fast recombination of photogenerated electrons and holes, but the photocatalytic activity of WO_3 can be significantly improved by numerous associations to obtain suitable reactivity. Generally evaluated in dye degradation, WO_3-based photocatalysts are also valuable for the treatment of wastewater polluted with medicinal molecules and plant protection products. This topic should continue to retain considerable attention in the near future.

Author Contributions: Conceptualization, D.D. and X.C.; resources, D.D., F.C. and X.C.; writing—review and editing, D.D., F.C. and X.C. All authors have read and agreed to the published version of the manuscript.

Funding: This research was funded by the Regional Council of Nouvelle Aquitaine, the French Ministry of Research and the European Regional Development Fund (ERDF).

Data Availability Statement: Not applicable.

Conflicts of Interest: The authors declare no conflict of interest.

References

1. Lassner, E.; Schubert, W.D. *Tungsten, Properties, Chemistry, Technology of the Element, Alloys, and Chemical Compounds*; Kluwer Academic Plenum Publishers: Vienna, Austria, 1999.
2. Morcom, W.W.R.; Worrell, W.L.; Sell, H.G.; Kaplan, H.I. The preparation and characterization of beta-tungsten, a metastable tungsten phase. *Metallurg. Trans.* **1974**, *5*, 155–161.
3. Christian, J.; Singh Gaur, R.P.; Wolfe, T.; Trasorras, J.R.L. Tungsten Chemicals and their Applications. In *Tungsten*; Newsletter of the International Tungsten Industry Association: London, UK, 2011.
4. Chianelli, R.R.; Berhault, G.; Torres, B. Unsupported transition metal sulfide catalysts: 100 years of science and application. *Catal. Today* **2009**, *147*, 275–286. [CrossRef]
5. Shan, S.; Yuan, P.; Han, W.; Shi, G.; Bao, X. Supported NiW catalysts with tunable size and morphology of active phases for highly selective hydrodesulfurization of fluid catalytic cracking naphtha. *J. Catal.* **2015**, *330*, 288–301. [CrossRef]
6. Zou, X.; Zhang, Y. Noble metal-free hydrogen evolution catalysts for water splitting. *Chem. Soc. Rev.* **2015**, *44*, 5148–5180. [CrossRef] [PubMed]
7. Chung, K.K.; Hai, X.; Ye, J. Transition Metal Disulfides as Noble-Metal-Alternative Co-Catalysts for Solar Hydrogen Production. *Adv. Energy Mater.* **2016**, *6*, 1502555. [CrossRef]
8. Xiang, Q.J.; Cheng, F.Y.; Lang, D. Hierarchical Layered WS2/Graphene-Modified CdS Nanorods for Efficient Photocatalytic Hydrogen Evolution. *ChemSusChem* **2016**, *9*, 996–1002. [CrossRef]
9. Ledendecker, M.; Mondschein, J.S.; Kasian, O.; Geiger, S.; Göhl, D.; Schalenbach, M.; Zeradjanin, A.; Cherevko, S.; Schaak, R.E.; Mayrhofer, K. Stability and Activity of Non-Noble-Metal-Based Catalysts Toward the Hydrogen Evolution Reaction. *Angew. Chem. Int. Ed.* **2017**, *56*, 9767–9771. [CrossRef] [PubMed]
10. Tackett, B.M.; Sheng, W.; Chen, J.G. Opportunities and Challenges in Utilizing Metal-Modified Transition Metal Carbides as Low-Cost Electrocatalysts. Perspective paper. *Joule* **2017**, *1*, 253–263. [CrossRef]
11. Omwoma, S.; Chen, W.; Tsunashima, R.; Song, Y.F. Recent advances on polyoxometalates intercalated layered double hydroxides: From synthetic approaches to functional material applications. *Coord. Chem. Rev.* **2014**, *258–259*, 58–71. [CrossRef]
12. Enferadi-Kerenkan, A.; Do, T.O.; Kaliaguine, S. Heterogeneous catalysis by tungsten-based heteropoly compounds. *Catal. Sci. Technol.* **2018**, *8*, 2257–2284. [CrossRef]
13. Farsani, M.R.; Jalilian, F.; Yadollahi, B.; Rudbari, H.A. A comparative study on Keggin and Wells–Dawson sandwich type polyoxometallates in the oxidation of alcohols with 30% hydrogen peroxide. *Polyhedron* **2014**, *76*, 102–107. [CrossRef]
14. Vickers, J.W.; Ly, H.; Sumliner, J.M.; Zhu, G.; Luo, Z.; Musaev, D.G.; Geletii, Y.V.; Hill, C.L. Differentiating homogeneous and heterogeneous water oxidation catalysis: Confirmation that $[Co_4(H_2O)_2(\alpha\text{-}PW_9O_{34})_2]^{10-}$ is a molecular water oxidation catalyst. *J. Am. Chem. Soc.* **2013**, *135*, 14110–14118. [CrossRef] [PubMed]
15. Dai, W.L.; Ding, J.; Zhu, Q.; Gao, R.; Yang, X. Tungsten containing materials as heterogeneous catalysts for green catalytic oxidation process. In *Catalysis*; The Royal Society of Chemistry: London, UK, 2016; Volume 28, pp. 1–27.
16. Rieck, G.D. *Tungsten and Its Compounds*; Elsevier: Amsterdam, The Netherlands, 1967.
17. Diehl, R.; Brandt, G.; Salje, E. The crystal structure of triclinic WO_3. *Acta Cryst.* **1978**, *B34*, 1105–1111. [CrossRef]
18. Corà, F.; Patel, A.; Harrison, N.M.; Dovesi, R.; Catlow, C.R.A. An ab Initio Hartree-Fock Study of the cubic and tetragonal phases of bulk tungsten trioxide. *J. Am. Chem. Soc.* **1996**, *118*, 12174–12182. [CrossRef]
19. Sun, W.; Yeung, M.T.; Lech, A.T.; Lin, C.W.; Lee, C.; Li, T.; Duan, X.; Zhou, J.; Kaner, R.B. High surface area tunnels in hexagonal WO_3. *Nano Lett.* **2015**, *15*, 4834–4838. [CrossRef]
20. Szilágyi, I.M.; Fórizs, B.; Rosseler, O.; Szegedi, Á.; Németh, P.; Király, P.; Tárkány, G.; Vajna, B.; Varga-Josepovits, K.; László, K.; et al. WO_3 photocatalysts: Influence of structure and composition. *J. Catal.* **2012**, *294*, 119–127. [CrossRef]

21. Szilágyi, I.M.; Madarász, J.; Pokol, G.; Király, P.; Tárkány, G.; Saukko, S.; Mizsei, J.; Tóth, A.L.; Szabó, A.; Varga-Josepovits, K. Stability and controlled composition of hexagonal WO_3. *Chem. Mater.* **2008**, *20*, 4116–4125. [CrossRef]
22. Zhu, J.; Wang, S.; Xie, S.; Li, H. Hexagonal single crystal growth of WO_3 nanorods along a [110] axis with enhanced adsorption capacity. *Chem. Commun.* **2011**, *47*, 4403–4405. [CrossRef]
23. Gu, Z.; Li, H.; Zhai, T.; Yang, W.; Xia, Y.; Ma, Y.; Yao, J. Large-scale synthesis of single-crystal hexagonal tungsten trioxide nanowires and electrochemical lithium intercalation into the nanocrystals. *J. Solid State Chem.* **2007**, *180*, 98–105. [CrossRef]
24. Zheng, H.; Zhen Ou, J.; Strano, M.S.; Kaner, R.B.; Mitchell, A.; Kalantar-zadeh, K. Nanostructured tungsten oxide—Properties, synthesis, and applications. *Adv. Struct. Mater.* **2011**, *21*, 2175–2196. [CrossRef]
25. Zhang, H.; Duan, G.; Li, Y.; Xu, X.; Dai, Z.; Cai, W. Leaf-like tungsten oxide nanoplatelets induced by laser ablation in liquid and subsequent aging. *Cryst. Growth Des.* **2012**, *12*, 2646–2652. [CrossRef]
26. Magnéli, A. Crystal structure studies on beta-tungsten oxide. *Ark Kemie* **1950**, *1*, 513.
27. Magnéli, A. Structure of β-tungsten oxide. *Nature* **1950**, *165*, 356–357. [CrossRef]
28. Tilley, R.J.D. The crystal chemistry of the higher tungsten oxides. *Int. J. Refract. Met. Hard Mater.* **1995**, *13*, 93–109. [CrossRef]
29. Slobodchikov, A.A.; Nekrasov, I.A.; Pavlov, N.S.; Korshunov, M.M. Simplicity Out of Complexity: Band Structure for $W_{20}O_{58}$ Superconductor. *Nanomaterials* **2021**, *11*, 97. [CrossRef]
30. Chen, S.; Xiao, Y.; Xie, W.; Wang, Y.; Hu, Z.; Zhang, W.; Zhao, H. Facile Strategy for Synthesizing Non-stoichiometric monoclinic structured tungsten trioxide (WO_{3-x}) with plasma resonance absorption and enhanced photocatalytic activity. *Nanomaterials* **2018**, *8*, 553. [CrossRef]
31. Walter, J.L.; Lou, K.A. Structures and chemistry of tungsten powder from doped and undoped tungsten blue oxide. *J. Mater. Sci.* **1989**, *24*, 3577–3587. [CrossRef]
32. Kurumada, M.; Kido, O.; Sato, T.; Suzuki, H.; Kimura, Y.; Kamitsuji, K.; Saito, Y.; Kaito, C. Structure of WO_3 ultrafine particles and their characteristic solid states. *J. Cryst. Growth* **2005**, *275*, e1673–e1678. [CrossRef]
33. Fang, Z.; Jiao, S.; Wang, B.; Yin, W.; Liu, S.; Gao, R.; Liu, Z.; Pang, G.; Feng, S. Synthesis of reduced cubic phase WO_{3-x} nanosheet by direct reduction of $H_2WO_4 \cdot H_2O$. *Mater. Today Energy* **2017**, *6*, 146–153. [CrossRef]
34. Solonin, Y.M.; Khyzhun, O.Y.; Graivoronskaya, E.A. Nonstoichiometric tungsten oxide based on hexagonal WO_3. *Cryst. Growth Des.* **2001**, *1*, 473–477. [CrossRef]
35. Cheng, H.; Klapproth, M.; Sagaltchik, A.; Li, S.; Thomas, A. Ordered mesoporous $WO_{2.83}$: Selective reduction synthesis, exceptional localized surface Plasmon resonance and enhanced hydrogen evolution reaction activity. *J. Mater. Chem. A* **2018**, *6*, 2249–2256. [CrossRef]
36. Sarin, V.K. Morphological changes occurring during reduction of WO_3. *J. Mater. Sci.* **1975**, *10*, 593–598. [CrossRef]
37. Pfeifer, J.; Badaljan, E.; Tekula-Buxbaum, P.; Kovacs, T.; Geszti, O.; Toth, A.L.; Lunk, H.J. Growth and morphology of $W_{18}0_{49}$ crystals produced by microwave decomposition of ammonium paratungstate. *J. Cryst. Growth* **1996**, *169*, 727–733. [CrossRef]
38. Wu, C. Preparation of ultrafine tungsten powders by in-situ hydrogen reduction of nano-needle violet tungsten oxide. *Int. J. Refract. Met. Hard Mater.* **2011**, *29*, 686–691. [CrossRef]
39. Soultanidis, N.; Zhou, W.; Kiely, C.J.; Wong, M.S. Solvothermal Synthesis of Ultrasmall Tungsten Oxide Nanoparticles. *Langmuir* **2012**, *28*, 17771–17777. [CrossRef] [PubMed]
40. Shpak, A.P.; Korduban, A.M.; Medvedskij, M.M.; Kandyba, V.O. XPS studies of active elements surface of gas sensors based on WO_{3-x} nanoparticles. *J. Electron Spectrosc. Relat. Phenom.* **2007**, *156–158*, 172–175. [CrossRef]
41. Ben-Dor, L.; Shimony, Y. Crystal structure, magnetic susceptibility and electrical conductivity of pure and NiO-doped MoO_2 and WO_2. *Mat. Res. Bull.* **1974**, *9*, 837–844. [CrossRef]
42. Palmer, D.J.; Dickens, P.G. Tungsten dioxide: Structure refinement by powder neutron diffraction. *Acta. Cryst. B* **1979**, *35*, 2199–2201. [CrossRef]
43. Koltypin, Y.; Nikitenko, S.I.; Gedanken, A. The sonochemical preparation of tungsten oxide nanoparticles. *J. Mater. Chem.* **2002**, *12*, 1107–1110. [CrossRef]
44. Coşkun, S.; Koziol, K.K.K. A facile water-assisted route for synthesis of tungsten dioxide (WO_2) nanopowders. *Powder Technol.* **2014**, *256*, 1–4. [CrossRef]
45. Heda, N.L.; Ahuja, U. Electronic properties and Compton scattering studies of monoclinic tungsten dioxide. *Radait. Phys. Chem.* **2015**, *106*, 33–39. [CrossRef]
46. Knowles, W.V.; Nutt, M.O.; Wong, M.S. Supported Metal Oxides and the Surface Density Metric. In *Catalyst Preparation, Science & Engineering*; Regalbuto, J., Ed.; CRC Press: Boca Raton, FL, USA, 2007; Chapter 11; pp. 251–282.
47. Murrell, L.L.; Grenoble, D.C.; Baker, R.T.K.; Prestridge, E.B.; Fung, S.C.; Chianelli, R.R.; Cramer, S.P. The Structure and Properties of Tungsten Oxide on Silica and on Alumina. *J. Catal.* **1983**, *79*, 203–206. [CrossRef]
48. Kim, D.S.; Ostromecki, M.; Wachs, I.E. Surface structures of supported tungsten oxide catalysts under dehydrated conditions. *J. Mol. Catal. A* **1996**, *106*, 93–102. [CrossRef]
49. Lee, E.L.; Wachs, I.E. In Situ Raman Spectroscopy of SiO_2-Supported Transition Metal Oxide Catalysts: An Isotopic ^{18}O-^{16}O Exchange Study. *J. Phys. Chem. C* **2008**, *112*, 6487–6498. [CrossRef]
50. Ross-Medgaarden, E.I.; Wachs, I.E. Structural determination of bulk and surface tungsten oxides with UV-vis diffuse reflectance spectroscopy and Raman spectroscopy. *J. Phys. Chem. C* **2007**, *111*, 15089–15099. [CrossRef]

51. Kiani, D.; Sourav, S.; Taifan, W.; Calatayud, M.; Tielens, F.; Wachs, I.E.; Baltrusaitis, J. Existence and Properties of Isolated Catalytic Sites on the Surface of β-Cristobalite-Supported, Doped Tungsten Oxide Catalysts (WOx/β-SiO2, Na-WOx/β-SiO2, Mn-WOx/β-SiO2) for Oxidative Coupling of Methane (OCM): A Combined Periodic DFT and Experimental Study. *ACS Catal.* **2020**, *10*, 4580–4592.
52. Chauvin, J.; Thomas, K.; Clet, G.; Houalla, M. Comparative influence of surface tungstate species and bulk amorphous WO_3 particles on the acidity and catalytic activity of tungsten oxide supported on silica. *J. Phys. Chem. C* **2015**, *119*, 12345–12355. [CrossRef]
53. Chan, S.C.; Wachs, I.E.; Murrell, L.L.; Dispenziere, N.C., Jr. Laser raman characterization of tungsten oxide supported on alumina: Influence of calcination temperatures. *J. Catal.* **1985**, *92*, 1–10. [CrossRef]
54. Chen, X.; Clet, G.; Thomas, K.; Houalla, M. Correlation between structure, acidity and catalytic performance of WOx/Al_2O_3 catalysts. *J. Catal.* **2010**, *273*, 236–244. [CrossRef]
55. Lebarbier, V.; Clet, G.; Houalla, M. Relations between structure, acidity, and activity of WOx/TiO_2: Influence of the initial state of the support, titanium oxyhydroxide, or titanium oxide. *J. Phys. Chem. C* **2006**, *110*, 22608–22617. [CrossRef]
56. Tribalis, A.; Panagiotou, G.D.; Tsilomelekis, G.; Kalampounias, A.G.; Bourikas, K.; Kordulis, C.; Boghosian, S.; Lycourghiotis, A. Temperature-dependent evolution of the molecular configuration of oxo-tungsten(VI) species deposited on the surface of titania. *J. Phys. Chem. C* **2014**, *118*, 11319–11332. [CrossRef]
57. Onfroy, T.; Clet, G.; Houalla, M. Acidity, surface structure, and catalytic performance of WOx supported on monoclinic zirconia. *J. Phys. Chem. B* **2005**, *109*, 3345–3354. [CrossRef]
58. Song, K.; Zhang, H.; Zhang, Y.; Tang, Y.; Tang, K. Preparation and characterization of WOx/ZrO_2 nanosized catalysts with high WOx dispersion threshold and acidity. *J. Catal.* **2013**, *299*, 119–128. [CrossRef]
59. Zhou, W.; Soultanidis, N.; Xu, H.; Wong, M.S.; Neurock, M.; Kiely, C.J.; Wachs, I.E. Nature of Catalytically Active Sites in the Supported WO_3/ZrO_2 Solid acid system: A current perspective. *ACS Catal.* **2017**, *7*, 2181–2198. [CrossRef]
60. Wachs, I.E.; Kim, T.; Ross, E.I. Catalysis science of the solid acidity of model supported tungsten oxide catalysts. *Catal. Today* **2006**, *116*, 162–168. [CrossRef]
61. Barton, D.G.; Soled, S.L.; Meitzner, G.D.; Fuentes, G.A.; Iglesia, E. Structural and catalytic characterization of solid acids based on zirconia modified by tungsten oxide. *J. Catal.* **1999**, *181*, 57–72. [CrossRef]
62. Soultanidis, N.; Zhou, W.; Psarras, A.C.; Gonzalez, A.J.; Iliopoulou, E.F.; Kiely, C.r.J.; Wachs, I.E.; Wong, M.S. Relating n-pentane isomerization activity to the tungsten surface density of WOx/ZrO_2. *J. Am. Chem. Soc.* **2010**, *132*, 13462–13471. [CrossRef]
63. Zhou, W.; Wachs, I.E.; Kiely, C.J. Nanostructural and chemical characterization of supported metal oxide catalysts by aberration corrected analytical electron microscopy. *Curr. Opin. Solid State Mater. Sci.* **2012**, *16*, 10–22. [CrossRef]
64. Del Angel, P.; Hernandez-Pichardo, M.L.; Montoya de la Fuente, A. Aberration-corrected HRTEM study of Mn-doped tungstated zirconia catalysts. *Catal. Today* **2013**, *212*, 201–205. [CrossRef]
65. Dos Santos, V.C.; Wilson, K.; Lee, A.F.; Nakagaki, S. Physicochemical properties of WOx/ZrO_2 catalysts for palmitic acid esterification. *Appl. Catal. B* **2015**, *162*, 75–84. [CrossRef]
66. Carabineiro, H.; Villanneau, R.; Carrier, X.; Herson, P.; Lemos, F.; Ramôa Ribeiro, F.; Proust, A.; Che, M. Zirconium-Substituted isopolytungstates: Structural models for zirconia-supported tungsten catalysts. *Inorg. Chem.* **2006**, *45*, 1915–1923. [CrossRef]
67. Kim, H.; Jeong, S.; Kim, D.H.; Park, Y.K.; Jeon, J.K. Preparation of highly dispersed tungsten oxide on MCM-41 via atomic layer deposition and its application to butanol dehydration. *J. Nanosci. Nanotechnol.* **2012**, *12*, 6074–6079. [CrossRef] [PubMed]
68. Bhuiyan, T.I.; Arudra, P.; Akhtar, M.N.; Aitani, A.M.; Abudawoud, R.H.; Al-Yami, M.A.; Al-Khattaf, S.S. Metathesis of 2-butene to propylene over W-mesoporous molecular sieves: A comparative study between tungsten containing MCM-41 and SBA-15. *Appl. Catal. A* **2013**, *467*, 224–234. [CrossRef]
69. Ramanathan, A.; Maheswari, R.; Grady, B.P.; Moore, D.S.; Barich, D.H.; Subramaniam, B. Tungsten-incorporated cage-type mesoporous silicate: W-KIT-5. *Microporous Mesoporous Mater.* **2013**, *175*, 43–49. [CrossRef]
70. Wu, J.-F.; Ramanathan, A.; Snavely, W.K.; Zhu, H.; Rokicki, A.; Subramaniam, B. Enhanced metathesis of ethylene and 2-butene on tungsten incorporated ordered mesoporous silicates. *Appl. Catal. A* **2016**, *528*, 142–149. [CrossRef]
71. Herrera, J.E.; Kwak, J.H.; Hu, J.Z.; Wang, Y.; Peden, C.H.F.; Macht, J.; Iglesia, E. Synthesis, characterization, and catalytic function of novel highly dispersed tungsten oxide catalysts on mesoporous silica. *J. Catal.* **2006**, *239*, 200–211. [CrossRef]
72. Maheswari, R.; Pachamuthu, M.P.; Ramanathan, A.; Subramaniam, B. Synthesis, characterization, and epoxidation activity of tungsten incorporated SBA-16 (W-SBA-16). *Ind. Eng. Chem. Res.* **2014**, *53*, 18833–18839. [CrossRef]
73. Meyer, S.; Beyer, H.; Köhler, K.; Hindhede Jensen, A.; Christensen, E.; Bjerrum, N.J. Space confined preparation of high surface area tungsten oxide and tungsten nitride inside the pores of mesoporous silica SBA-15. *Microporous Mesoporous Mater.* **2015**, *211*, 147–151. [CrossRef]
74. Telalović, S.; Ramanathan, A.; Mul, G.; Hanefeld, U. TUD-1: Synthesis and application of a versatile catalyst, carrier, material. *J. Mater. Chem.* **2010**, *20*, 642–658. [CrossRef] [PubMed]
75. Pachamuthu, M.P.; Maheswari, R.; Ramanathan, A. Synthesis and characterizations of isolated WO_4 anchored on mesoporous TiTUD-1 support. *Appl. Surf. Sci.* **2017**, *402*, 286–293. [CrossRef]
76. Maksasithorn, S.; Praserthdam, P.; Suriye, K.; Debecker, D.P. Preparation of super-microporous WO_3-SiO_2 olefin metathesis catalysts by the aerosol-assisted sol-gel process. *Microporous Mesoporous Mater.* **2015**, *213*, 125–133. [CrossRef]

77. Bouhoute, Y.; Garron, A.; Grekov, D.; Merle, N.; Szeto, K.C.; De Mallmann, A.; Del Rosal, I.; Maron, L.; Girard, G.; Gauvin, R.M.; et al. Well-defined supported mononuclear tungsten oxo species as olefin metathesis pre-catalysts. *ACS Catal.* **2014**, *4*, 4232–4241. [CrossRef]
78. Coperet, C.; Comas-Vives, A.; Conley, M.P.; Estes, D.P.; Fedorov, A.; Mougel, V.; Nagae, H.; Nunez-Zarur, F.; Zhizhko, P.A. Surface organometallic and coordination chemistry toward single-site heterogeneous catalysts: Strategies, methods, structures, and activities. *Chem. Rev.* **2016**, *116*, 323–421. [CrossRef]
79. Busca, G. The surface acidity of solid oxides and its characterization by IR spectroscopic methods. An attempt at systematization. *Phys. Chem. Chem. Phys.* **1999**, *1*, 723–736. [CrossRef]
80. Kanan, S.M.; Lu, Z.; Cox, J.K.; Bernhardt, G.; Tripp, C.P. Identification of surface sites on monoclinic WO_3 powders by infrared spectroscopy. *Langmuir* **2002**, *18*, 1707–1712. [CrossRef]
81. Choi, H.; Lee, E.; Jin, M.; Park, Y.K.; Kim, J.M.; Jeon, J.K. Catalytic properties of highly ordered crystalline nanoporous tungsten oxide in butanol dehydration. *J. Nanosci. Nanotechnol.* **2014**, *14*, 8828–8833. [CrossRef]
82. Kasian, N.; Yaremov, P.S.; Shvets, O.V.; Burel, L.; Puzenat, E.; Tuel, A. Influence of thermal treatments on phase composition and acidity of mesoporous tungsten oxide. *Microporous Mesoporous Mater.* **2014**, *194*, 15–23. [CrossRef]
83. Yue, C.; Zhu, X.; Rigutto, M.; Hensen, E. Acid catalytic properties of reduced tungsten and niobium tungsten oxides. *Appl. Catal. B* **2015**, *163*, 370–381. [CrossRef]
84. Li, Z.; Fang, Z.; Kelley, M.S.; Kay, B.D.; Rousseau, R.; Dohnálek, Z.; Dixon, D.A. Ethanol conversion on cyclic $(MO_3)_3$ (M = Mo, W) clusters. *J. Phys. Chem. C* **2014**, *118*, 4869–4877. [CrossRef]
85. Rousseau, R.; Dixon, D.A.; Kay, B.D.; Dohnálek, Z. Dehydration, dehydrogenation, and condensation of alcohols on supported oxide catalysts based on cyclic $(WO_3)_3$ and $(MoO_3)_3$ clusters. *Chem. Soc. Rev.* **2014**, *43*, 7664–7680. [CrossRef] [PubMed]
86. Barton, D.G.; Soled, S.L.; Iglesia, E. Solid acid catalysts based on supported tungsten oxides. *Top. Catal.* **1998**, *6*, 87–99. [CrossRef]
87. Zaki, M.I.; Mekhemer, G.A.H.; Fouad, N.E.; Rabee, A.I.M. Structure-acidity correlation of supported tungsten(VI)-oxo-species: FT-IR and TPD studies of adsorbed pyridine and catalytic decomposition of 2-propanol. *Appl. Surf. Sci.* **2014**, *308*, 380–387. [CrossRef]
88. Martin, D.; Duprez, D. Evaluation of the acid-base surface properties of several oxides and supported metal catalysts by means of model reactions. *J. Mol. Catal. A* **1997**, *118*, 113–128. [CrossRef]
89. Hu, J.Z.; Kwak, J.H.; Wang, Y.; Hu, M.Y.; Turcu, R.V.; Peden, C.H.F. Characterizing surface acidic sites in mesoporous-silica-supported tungsten oxide catalysts using solid-state NMR and quantum chemistry calculations. *J. Phys. Chem. C* **2011**, *115*, 23354–23362. [CrossRef]
90. González, J.; Wang, J.A.; Chen, L.F.; Manríquez, M.E.; Dominguez, J.M. Structural defects, lewis acidity, and catalysis properties of mesostructured WO_3/SBA-15 nanocatalysts. *J. Phys. Chem. C* **2017**, *121*, 23988–23999. [CrossRef]
91. Kulal, A.B.; Dongare, M.K.; Umbarkar, S.B. Sol-gel synthesised WO_3 nanoparticles supported on mesoporous silica for liquid phase nitration of aromatics. *Appl. Catal. B* **2016**, *182*, 142–152. [CrossRef]
92. Bhaumik, P.; Dhepe, P.L. From lignocellulosic biomass to furfural: Insight into the active species of a silica-supported tungsten oxide catalyst. *ChemCatChem* **2017**, *9*, 2709–2716. [CrossRef]
93. Zhu, H.; Ramanathan, A.; Wu, J.F.; Subramaniam, B. Genesis of strong brønsted acid sites in WZr-KIT-6 catalysts and enhancement of ethanol dehydration activity. *ACS Catal.* **2018**, *8*, 4848–4859. [CrossRef]
94. DePuccio, D.P.; Ruíz-Rodríguez, L.; Rodríguez-Castellón, E.; Botella, P.; López Nieto, J.M.; Landry, C.C. Investigating the influence of Au nanoparticles on porous SiO_2-WO_3 and WO_3 methanol transformation catalysts. *J. Phys. Chem. C* **2016**, *120*, 27954–27963. [CrossRef]
95. Shi, G.; Cao, Z.; Xu, J.; Jin, K.; Bao, Y.; Xu, S. Effect of WOx doping into Pt/SiO_2 catalysts for glycerol hydrogenolysis to 1,3-propanediol in liquid phase. *Catal. Lett.* **2018**, *148*, 2304–2314. [CrossRef]
96. Soled, S.L.; McVicker, G.B.; Murrell, L.L.; Sherman, L.G.; Dispenziere, N.C.; Hsu, S.L.; Waldman, D. Comparison of the acidities of WO_3/Al_2O_3 and ultrastable faujasite catalysts. *J. Catal.* **1988**, *111*, 286–295. [CrossRef]
97. Zhang, R.; Jagiello, J.; Hu, J.F.; Huang, Z.Q.; Schwarz, J.A.; Datye, A. Effect of WO_3 loading on the surface acidity of WO_3/Al_2O_3 composite oxides. *Appl. Catal. A* **1992**, *84*, 123–139. [CrossRef]
98. Kitano, T.; Hayashi, T.; Uesaka, T.; Shishido, T.; Teramura, K.; Tanaka, T. Effect of high-temperature calcination on the generation of Brønsted acid sites on WO_3/Al_2O_3. *ChemCatChem* **2014**, *6*, 2011–2020. [CrossRef]
99. Barrault, J.; Boulinguiez, M.; Forquy, C.; Maurel, R. Synthesis of methyl mercaptan from carbon oxides and H_2S with tungsten-alumina catalysts. *Appl. Catal.* **1987**, *33*, 309–330. [CrossRef]
100. Mashkin, V.Y.; Kudenkov, V.M.; Mashkina, A.V. Kinetics of the catalytic reaction between methanol and hydrogen sulfide. *Ind. Eng. Chem. Res.* **1995**, *34*, 2964–2970. [CrossRef]
101. Cordova, A.; Blanchard, P.; Salembier, H.; Lancelot, C.; Frémy, G.; Lamonier, C. Direct synthesis of methyl mercaptan from $H_2/CO/H_2S$ using tungsten based supported catalysts: Investigation of the active phase. *Catal. Today* **2017**, *292*, 143–153. [CrossRef]
102. Taifan, W.; Baltrusaitis, J. Minireview: Direct catalytic conversion of sour natural gas (CH_4 + H_2S + CO_2) components to high value chemicals and fuels. *Catal. Sci. Technol.* **2017**, *7*, 2919–2929. [CrossRef]
103. Wang, W.; Li, Y.; Zhang, X.; Fang, W.; Yang, Y. Catalytic synthesis of methanethiol from methanol and carbon disulfide over KW/Al_2O_3 catalysts. *Catal. Commun.* **2015**, *69*, 104–108. [CrossRef]

104. Zhu, M.; Li, B.; Jehng, J.M.; Sharma, L.; Taborda, J.; Zhang, L.; Stach, E.; Wachs, I.E.; Wu, Z.; Baltrusaitis, J. Molecular structure and sour gas surface chemistry of supported $K_2O/WO_3/Al_2O_3$ catalysts. *Appl. Catal. B* **2018**, *232*, 146–154. [CrossRef]
105. Kiani, D.; Belletti, G.; Quaino, P.; Tielens, F.; Baltrusaitis, J. Structure and vibrational properties of potassium-promoted tungsten oxide catalyst monomeric sites supported on alumina ($K_2O/WO_3/Al_2O_3$) characterized using periodic density functional theory. *J. Phys. Chem. C* **2018**, *122*, 24190−24201. [CrossRef]
106. Hino, M.; Arata, K. Synthesis of Solid Superacid of tungsten oxide supported on zirconia and its catalytic action for reactions of butane and pentane. *J. Chem. Soc. Chem. Commun.* **1988**, *18*, 1259–1260. [CrossRef]
107. Li, S.; Zhou, H.; Jin, C.; Feng, N.; Liu, F.; Deng, F.; Wang, J.Q.; Huang, W.; Xiao, L.; Fan, J. Formation of subnanometer Zr-WOx clusters within mesoporous W−Zr mixed oxides as strong solid acid catalysts for Friedel−Crafts alkylation. *J. Phys. Chem. C* **2014**, *118*, 6283–6290. [CrossRef]
108. Kuba, S.; Heydorn, P.C.; Grasselli, R.K.; Gates, B.C.; Che, M. Knözinger, H. Redox properties of tungstated zirconia catalysts: Relevance to the activation of n-alkanes. *Phys. Chem. Chem. Phys.* **2001**, *3*, 146–154. [CrossRef]
109. Santiesteban, J.G.; Vartuli, J.C.; Han, S.; Bastian, R.D.; Chang, C.D. Influence of the preparative method on the activity of highly acidic WOx/ZrO_2 and the relative acid activity compared with zeolites. *J. Catal.* **1997**, *168*, 431–441. [CrossRef]
110. Afanasiev, P.; Geantet, C.; Breysse, M.; Coudurier, G.; Vedrine, J.C. Influence of preparation method on the acidity of $MoO_3(WO_3)/ZrO_2$ catalysts. *J. Chem. Soc. Faraday Trans.* **1994**, *90*, 193–202. [CrossRef]
111. Baertsch, C.D.; Soled, S.L.; Iglesia, E. Isotopic and Chemical titration of acid sites in tungsten oxide domains supported on zirconia. *J. Phys. Chem. B* **2001**, *105*, 1320–1330. [CrossRef]
112. Iglesia, E.; Barton, D.G.; Biscardi, J.A.; Gines, M.J.L.; Soled, S.L. Bifunctional pathways in catalysis by solid acids and bases. *Catal. Today* **1997**, *38*, 339–360. [CrossRef]
113. Di Gregorio, F.; Keller, V. Activation and isomerization of hydrocarbons over WO_3/ZrO_2 catalysts I. Preparation, characterization, and X-ray photoelectron spectroscopy studies. *J. Catal.* **2004**, *225*, 45–55. [CrossRef]
114. Galano, A.; Rodriguez-Gattorno, G.; Torres-García, E. A combined theoretical-experimental study on the acidity of WOx-ZrO_2 systems. *Phys. Chem. Chem. Phys.* **2008**, *10*, 4181–4188. [CrossRef] [PubMed]
115. Lee, J.H.; Shin, C.H.; Suh, Y.W. Higher Brønsted acidity of WOx/ZrO_2 catalysts prepared using a high surface area zirconium oxyhydroxide. *Mol. Catal.* **2017**, *438*, 272–279. [CrossRef]
116. Yamamoto, T.; Teramachi, A.; Orita, A.; Kurimoto, A.; Motoi, T.; Tanaka, T. Generation of strong acid sites on yttrium-doped tetragonal ZrO_2-supported tungsten oxides: Effects of dopant amounts on acidity, crystalline phase, kinds of tungsten species, and their dispersion. *J. Phys. Chem. C* **2016**, *120*, 19705–19713. [CrossRef]
117. Kourieh, R.; Bennici, S.; Marzo, M.; Gervasini, A.; Auroux, A. Investigation of the WO_3/ZrO_2 surface acidic properties for the aqueous hydrolysis of cellobiose. *Catal. Commun.* **2012**, *19*, 119–126. [CrossRef]
118. Wang, H.; Wu, Y.; He, L.; Liu, Z. Supporting Tungsten Oxide on Zirconia by Hydrothermal and Impregnation Methods and Its Use as a Catalyst To Reduce the Viscosity of Heavy Crude Oil. *Energy Fuels* **2012**, *26*, 6518–6527. [CrossRef]
119. Signoretto, M.; Ghedini, E.; Menegazzo, F.; Cerrato, G.; Crocellà, V.; Bianchi, C.L. Aerogel and xerogel WO_3/ZrO_2 samples for fine chemicals production. *Microporous Mesoporous Mater.* **2013**, *165*, 134–141. [CrossRef]
120. Miao, Z.; Zhao, H.; Song, H.; Chou, L. Ordered mesoporous zirconium oxophosphate supported tungsten oxide solid acid catalysts: The improved Brønsted acidity for benzylation of anisole. *RSC Adv.* **2014**, *4*, 22509–22519. [CrossRef]
121. Miao, Z.; Song, H.; Zhao, H.; Xu, L.; Chou, L. One-pot synthesis of mesoporous ZrPW solid acid catalyst for liquid phase benzylation of anisole. *Catal. Sci. Technol.* **2014**, *4*, 838–850. [CrossRef]
122. Vilcocq, L.; Koerin, R.; Cabiac, A.; Especel, C.; Lacombe, S.; Duprez, D. New bifunctional catalytic systems for sorbitol transformation into biofuels. *Appl. Catal. B* **2014**, *148–149*, 499–508. [CrossRef]
123. Chen, J.P.; Yang, R.T. Role of WO_3 in mixed V_2O_5-WO_3/TiO_2 catalysts for selective catalytic reduction of nitric oxide with ammonia. *Appl. Catal. A* **1992**, *80*, 135–148. [CrossRef]
124. Alemany, L.J.; Lietti, L.; Ferlazzo, N.; Forzatti, P.; Busca, G.; Giamello, E.; Bregani, F. Reactivity and physico-chemical characterisation of V_2O_5-WO_3/TiO_2 De-NO_x catalysts. *J. Catal.* **1995**, *155*, 117–130. [CrossRef]
125. Forzatti, P. Present status and perspectives in de-NO_x SCR catalysis. *Appl. Catal. A* **2001**, *222*, 221–236. [CrossRef]
126. Paganini, M.C.; Dall'Acqua, L.; Giamello, E.; Lietti, L.; Forzatti, P.; Busca, G. An EPR Study of the surface chemistry of the V_2O_5-WO_3/tio_2 catalyst: Redox behaviour and state of V(IV). *J. Catal.* **1997**, *166*, 195–205. [CrossRef]
127. Wang, C.; Yang, S.; Chang, H.; Peng, Y.; Li, J. Dispersion of tungsten oxide on SCR performance of V_2O_5-WO_3/TiO_2: Acidity, surface species and catalytic activity. *Chem. Eng. J.* **2013**, *225*, 520–527. [CrossRef]
128. Kompio, P.G.W.A.; Brückner, A.; Hipler, F.; Auer, G.; Löffler, E.; Grünert, W. A new view on the relations between tungsten and vanadium in V_2O_5-WO_3/TiO_2 catalysts for the selective reduction of NO with NH_3. *J. Catal.* **2012**, *286*, 237–247. [CrossRef]
129. Lai, J.K.; Wachs, I.E. A Perspective on the selective catalytic reduction (SCR) of NO with NH_3 by supported $V_2O_5−WO_3/TiO_2$ catalysts. *ACS Catal.* **2018**, *8*, 6537–6551. [CrossRef]
130. Topsøe, N.Y.; Dumesic, J.A.; Topsøe, H. Vanadia/Titania Catalysts for Selective catalytic reduction of nitric oxide by ammonia. II studies of active sites and formulation of catalytic cycles. *J. Catal.* **1995**, *151*, 241–252. [CrossRef]
131. Dumesic, J.A.; Topsøe, N.Y.; Topsøe, H.; Chen, Y.; Slabiak, T. Kinetics of Selective catalytic reduction of nitric oxide by ammonia over vanadia/titania. *J. Catal.* **1996**, *163*, 409–417. [CrossRef]

132. Han, L.; Cai, S.; Gao, M.; Hasagawa, J.; Wang, P.; Zhang, J.; Shi, L.; Zhang, D. Selective Catalytic Reduction of NO_x with NH_3 by Using Novel Catalysts: State of the Art and Future Prospects. *Chem. Rev.* **2019**, *119*, 10916–10976. [CrossRef]
133. Lietti, L.; Ramis, G.; Berti, F.; Toledo, G.; Robba, D.; Busca, G.; Forzatti, P. Chemical, structural and mechanistic aspects on NO_x SCR over commercial and model oxide catalyst. *Catal. Today* **1998**, *42*, 101–116. [CrossRef]
134. Montzka, S.A.; Dlugokencky, E.J.; Butler, J.H. Review: Non-CO_2 greenhouse gases and climate change. *Nature* **2011**, *476*, 43–50. [CrossRef]
135. Van Groenigen, K.J.; Osenberg, C.W.; Hungate, B.A. Increased soil emissions of potent greenhouse gases under increased atmospheric CO_2. *Nature* **2011**, *475*, 214–216. [CrossRef]
136. Djerad, S.; Tifouti, L.; Crocoll, M.; Weisweiler, W. Effect of vanadia and tungsten loadings on the physical and chemical characteristics of V_2O_5-WO_3/TiO_2 catalysts. *J. Mol. Catal. A* **2004**, *208*, 257–265. [CrossRef]
137. Liu, X.; Li, J.; Li, X.; Peng, Y.; Wang, H.; Jiang, X.; Wang, L. NH_3 selective catalytic reduction of NO: A large surface TiO_2 support and its promotion of V_2O_5 dispersion on the prepared catalyst. *Chin. J. Catal.* **2016**, *37*, 878–887. [CrossRef]
138. Zhu, M.; Lai, J.-K.; Tumuluri, U.; Wu, Z.; Wachs, I.E. Nature of active sites and surface intermediates during SCR of NO with NH_3 by supported $V_2O_5-WO_3/TiO_2$ catalysts. *J. Am. Chem. Soc.* **2017**, *139*, 15624–15627. [CrossRef] [PubMed]
139. Liu, H.; You, C.; Wang, H. Time-resolved in-situ IR and DFT study: NH_3 adsorption and redox cycle of acid site on vanadium-based catalysts for NO abatement via selective catalytic reduction. *Chem. Eng. J.* **2020**, *382*, 122756–122764. [CrossRef]
140. Giraud, F.; Couble, J.; Geantet, C.; Guilhaume, N.; Loridant, S.; Gros, S.; Porcheron, L.; Kanniche, M.; ianchi, D. Experimental Microkinetic Approach of De-NO_x by NH_3 on $V_2O_5/WO_3/TiO_2$ Catalysts. 5. Impacts of the NH_3-H_2O Coadsorption on the Coverage of Sulfated TiO_2-Based Solids. *J. Phys. Chem. C* **2018**, *122*, 24619–24633. [CrossRef]
141. Zhao, X.; Yan, Y.; Mao, L.; Fu, M.; Zhao, H.; Sun, L.; Xiao, Y.; Dong, G. A relationship between the V^{4+}/V^{5+} ratio and the surface dispersion, surface acidity, and redox performance of V_2O_5–WO_3/TiO_2 SCR catalysts. *RSC Adv.* **2018**, *8*, 31081–31093. [CrossRef]
142. He, G.; Lian, Z.; Yu, Y.; Yang, Y.; Liu, K.; Shi, X.; Yan, Z.; Shan, W.; He, H. Polymeric vanadyl species determine the low-temperature activity of V-based catalysts for the SCR of NO_x with NH_3. *Sci. Adv.* **2018**, *4*, eaau4637. [CrossRef] [PubMed]
143. Chen, H.; Xia, Y.; Fang, R.; Huang, H.; Gan, Y.; Liang, C.; Zhang, J.; Zhang, W.; Liu, X. The effects of tungsten and hydrothermal aging in promoting NH_3-SCR activity on V_2O_5/WO_3-TiO_2 catalysts. *Appl. Surf. Sci.* **2018**, *459*, 639–646. [CrossRef]
144. Kompio, P.G.W.A.; Brückner, A.; Hipler, F.; Manoylova, O.; Auer, G.; Mestl, G.; Grünert, W. V_2O_5-WO_3/TiO_2 catalysts under thermal stress: Responses of structure and catalytic behavior in the selective catalytic reduction of NO by NH_3. *Appl. Catal. B* **2017**, *217*, 365–377. [CrossRef]
145. Kwon, D.W.; Park, K.H.; Hong, S.C. Effect of vanadium structure and lattice oxygen in V-based TiO_2 catalysts on selective catalytic reduction of NO_x by NH_3. *J. Chem. Eng. Jpn.* **2016**, *49*, 526–533. [CrossRef]
146. Marberger, A.; Elsener, M.; Nuguid, R.J.G.; Ferri, D.; Kröcher, O. Thermal activation and aging of a V_2O_5-WO_3/TiO_2 catalyst for the selective catalytic reduction of NO with NH_3. *Appl. Catal. A* **2019**, *573*, 64–72. [CrossRef]
147. Liang, Q.; Li, J.; He, H.; Yue, T.; Tong, L. Effects of SO_2 and H_2O on low-temperature NO conversion over F-V_2O_5-WO_3/TiO_2 catalysts. *J. Environ. Sci.* **2020**, *90*, 253–261. [CrossRef]
148. Beale, A.M.; Lezcano-Gonzalez, I.; Maunula, T.; Palgrave, R.G. Development and characterization of thermally stable supported V–W–TiO_2 catalysts for mobile NH_3–SCR applications. *Catal. Struct. React.* **2015**, *1*, 25–34. [CrossRef]
149. Marberger, A.; Ferri, D.; Rentsch, D.; Krumeich, F.; Elsener, M.; Kröcher, O. Effect of SiO_2 on co-impregnated V_2O_5/WO_3–TiO_2 catalysts for the selective catalytic reduction of NO with NH_3. *Catal. Today* **2019**, *320*, 123–132. [CrossRef]
150. Shin, J.B.; Dung, T.W.; Lee, H. Structure, surface acidity and catalytic activity of WO_3-TiO_2 catalyst for NH_3-SCR of NO_x. *J. Ceram. Proc. Res.* **2014**, *15*, 125–129.
151. He, Y.; Ford, M.E.; Zhu, M.; Liu, Q.; Tumuluri, U.; Wu, Z.; Wachs, I.E. Influence of catalyst synthesis method on selective catalytic reduction(SCR) of NO by NH_3 with V_2O_5-WO_3/TiO_2 catalysts. *Appl. Catal. B* **2016**, *193*, 141–150. [CrossRef]
152. Ferjani, W.; Khalfallah Boudali, L.; Delahay, G.; Petitto, C. Reduction of nitrogen oxide by ammonia over vanadium supported on mixed tungsten–titanium-pillared clays. *Chem. Lett.* **2016**, *45*, 872–874. [CrossRef]
153. Wang, J.; Miao, J.; Yu, W.; Chen, Y.; Chen, J. Study on the local difference of monolithic honeycomb V_2O_5-WO_3/TiO_2 denitration catalyst. *Mater. Chem. Phys.* **2017**, *198*, 193–199. [CrossRef]
154. Zhao, K.; Han, W.; Tang, Z.; Zhang, G.; Lu, J.; Lu, G.; Zhen, X. Investigation of coating technology and catalytic performance over monolithic V_2O_5-WO_3/TiO_2 catalyst for selective catalytic reduction of NO_x with NH_3. *Colloids Surf. A Physicochem. Eng. Asp.* **2016**, *503*, 53–60. [CrossRef]
155. Johnson, T.V. Review of selective catalytic reduction (SCR) and related technologies for mobile applications. In *Urea-SCR Technology for deNO$_x$ after Treatment of Diesel Exhausts. Fundamental and Applied Catalysis*; Nova, I., Tronconi, I.E., Eds.; Springer: New York, NY, USA, 2014; pp. 3–31.
156. Jung, Y.; Shin, Y.J.; Pyo, Y.D.; Cho, C.P.; Jang, J.; Kim, G. NO_x and N_2O emissions over a Urea-SCR system containing both V_2O_5-WO_3/TiO_2 and Cu-zeolite catalysts in a diesel engine. *Chem. Eng. J.* **2017**, *326*, 853–862. [CrossRef]
157. Cho, C.P.; Pyo, Y.D.; Jang, J.Y.; Kim, G.C.; Shin, Y.J. NO_x reduction and N_2O emissions in a diesel engine exhaust using Fe-zeolite and vanadium based SCR catalysts. *Appl. Therm. Eng.* **2017**, *110*, 18–24. [CrossRef]
158. Szymaszek, A.; Samojeden, B.; Motak, M. The Deactivation of Industrial SCR Catalysts—A Short Review. *Energies* **2020**, *13*, 3870. [CrossRef]

159. Kröcher, O.; Elsener, M. Chemical deactivation of $V_2O_5/WO_3–TiO_2$ SCR catalysts by additives and impurities from fuels, lubrication oils, and urea solution I. Catalytic studies. *Appl. Catal. B* **2008**, *75*, 215–227. [CrossRef]
160. Nicosia, D.; Czekaj, I.; Kröcher, O. Chemical deactivation of $V_2O_5/WO_3–TiO_2$ SCR catalysts by additives and impurities from fuels, lubrication oils, and urea solution Part II. Characterization study of the effect of alkali and alkaline earth metals. *Appl. Catal. B* **2008**, *75*, 228–236. [CrossRef]
161. Xie, X.; Lu, J.; Hums, E.; Huang, Q.; Lu, Z. Study on the deactivation of $V_2O_5-WO_3/TiO_2$ selective catalytic reduction catalysts through transient kinetics. *Energy Fuel* **2015**, *29*, 3890–3896. [CrossRef]
162. Siaka, H.; Dujardin, C.; Moissette, A.; Granger, P. Structural Induced Effect of Potassium on the Reactivity of Vanadate Species in $V_2O_5–WO_3/TiO_2$ SCR-Catalyst. *Top. Catal.* **2019**, *62*, 55–62. [CrossRef]
163. Chen, C.; Wu, X.; Yu, W.; Gao, Y.; Weng, D.; Shi, L.; Geng, C. Potassium poisoning of titania supported $deNO_x$ catalysts: Preservation of vanadia and sacrifice of tungsten oxide. *Chin. J. Catal.* **2015**, *36*, 1287–1294. [CrossRef]
164. Wu, X.; Yu, W.; Si, Z.; Weng, D. Chemical deactivation of $V_2O_5-WO_3/TiO_2$ SCR catalyst by combined effect of potassium and chloride. *Front. Environ. Sci. Eng.* **2013**, *7*, 420–427. [CrossRef]
165. Reddy Putluru, S.S.; Schill, L.; Godiksena, A.; Poreddy, R.; Mossina, S.; Jensen, A.D.; Fehrmann, R. Promoted V_2O_5/TiO_2 catalysts for selective catalytic reduction of NO with NH_3 at low temperatures. *Appl. Catal. B* **2016**, *183*, 282–290. [CrossRef]
166. Miao, J.; Yi, X.; Su, Q.; Li, H.; Chen, J.; Wang, J. Poisoning Effects of Phosphorus, Potassium and Lead on V_2O_5-WO_3/TiO_2 Catalysts for Selective Catalytic Reduction with NH_3. *Catalysts* **2020**, *10*, 345. [CrossRef]
167. Xiang, J.; Du, X.; Wan, Y.; Chen, Y.; Ran, J.; Zhang, L. Alkali-driven active site shift of fast SCR with NH_3 on V_2O_5-WO_3/TiO_2 catalyst via a novel Eley-Rideal mechanism. *Catal. Sci. Technol.* **2019**, *9*, 6085–6091. [CrossRef]
168. Li, H.; Miao, J.; Su, Q.; Yu, Y.; Chen, Y.; Chen, J.; Wang, J. Improvement in alkali metal resistance of commercial $V_2O_5–WO_3/TiO_2$ SCR catalysts modified by Ce and Cu. *J. Mater. Sci.* **2019**, *54*, 14707–14719. [CrossRef]
169. Li, X.; Li, X.-S.; Chen, J.; Li, J.; Hao, J. An efficient novel regeneration method for Ca-poisoning $V_2O_5/WO_3–TiO_2$ catalysts. *Catal. Commun.* **2016**, *87*, 45–48. [CrossRef]
170. Li, X.; Li, X.S.; Yang, R.T.; Mo, J.; Li, J.; Hao, J. The poisoning effects of calcium on $V_2O_5/WO_3–TiO_2$ catalysts for the SCR reaction: Comparison of different forms of calcium. *Mol. Catal.* **2017**, *434*, 16–24. [CrossRef]
171. Odenbrand, C.U.I. $CaSO_4$ deactivated V_2O_5-WO_3/TiO_2 SCR catalyst for a diesel power plant. Characterization and simulation of the kinetics of the SCR reactions. *Appl. Catal. B* **2018**, *234*, 365–377. [CrossRef]
172. Phil, H.H.; Reddy, M.P.; Kumar, P.A.; Ju, L.K.; Hyo, J.S. SO_2 resistant antimony promoted V_2O_5/TiO_2 catalyst for NH_3-SCR of NO_x at low temperatures. *Appl. Catal. B* **2008**, *78*, 301–308. [CrossRef]
173. Kwon, D.W.; Park, K.H.; Hong, S.C. Enhancement of SCR activity and SO_2 resistance on VOx/TiO_2 catalyst by addition of molybdenum. *Chem. Eng. J.* **2016**, *284*, 315–324. [CrossRef]
174. Zhu, N.; Shan, W.; Lian, Z.; Zhang, Y.; Liu, K.; He, H. A superior Fe-V-Ti catalyst with high activity and SO_2 resistance for the selective catalytic reduction of NO_x with NH_3. *J. Hazard. Mater.* **2020**, *382*, 120970–120978. [CrossRef]
175. Xu, T.; Wu, X.; Gao, Y.; Lin, Q.; Hu, J.; Wen, D. Comparative study on sulfur poisoning of V_2O_5-Sb_2O_3/TiO_2 and V_2O_5-WO_3/TiO_2 monolithic catalysts for low-temperature NH_3-SCR. *Catal. Commun.* **2017**, *93*, 33–36. [CrossRef]
176. Xu, L.; Wang, C.; Chang, H.; Wu, Q.; Zhang, T.; Li, J. New Insight into SO_2 Poisoning and Regeneration of CeO_2-WO_3/TiO_2 and V_2O_5-WO_3/TiO_2 Catalysts for Low-Temperature NH_3-SCR. *Environ. Sci. Technol.* **2018**, *52*, 7064–7071. [CrossRef]
177. Wang, Y.; Yi, W.; Yu, J.; Zeng, J.; Chang, H. A novel method for assessing SO_2 poisoning effect and thermal regeneration possibility of MO_x-WO_3/TiO2 (M = Fe, Mn, Cu, V) catalysts for NH_3-SCR. *Environ. Sci. Technol.* **2020**, *54*, 12612–12620. [CrossRef]
178. Cao, L.; Wu, X.; Chen, Z.; Ma, Y.; Ma, Z.; Ran, R.; Si, Z.; Weng, D.; Wang, B. A comprehensive study on sulfur tolerance of niobia modified CeO_2/WO_3-TiO_2 catalyst for low-temperature NH_3-SCR. *Appl. Catal. A* **2019**, *580*, 121–130. [CrossRef]
179. Jeong, B.; Ye, B.; Kim, E.-S.; Kim, H.D. Characteristics of selective catalytic reduction (SCR) catalyst adding graphene-tungsten nanocomposite. *Catal. Commun.* **2017**, *93*, 15–19. [CrossRef]
180. Xu, T.; Wu, X.; Liu, X.; Cao, L.; Lin, Q.; Wen, D. Effect of barium sulfate modification on the SO_2 tolerance of V_2O_5/TiO_2 catalyst for NH_3-SCR reaction. *J. Environ. Sci.* **2017**, *57*, 110–117. [CrossRef] [PubMed]
181. Senior, C.L.; Lignell, D.O.; Sarofim, A.F.; Mehta, A. Modeling arsenic partitioning in coal-fired power plants. *Comb. Flame* **2006**, *147*, 209–221. [CrossRef]
182. Peng, Y.; Li, J.; Si, W.; Luo, J.; Dai, Q.; Luo, X.; Liu, X.; Hao, J. Insight into Deactivation of Commercial SCR Catalyst by Arsenic: An Experiment and DFT Study. *Environ. Sci. Technol.* **2014**, *48*, 13895–13900. [CrossRef]
183. Peng, Y.; Si, W.; Li, X.; Luo, J.; Li, J.; Crittenden, J.; Hao, J. Comparison of MoO_3 and WO_3 on arsenic poisoning $V_2O_5–WO_3/TiO_2$ catalyst: DRIFTS and DFT study. *Appl. Catal. B* **2016**, *181*, 692–698. [CrossRef]
184. Kong, M.; Liu, Q.; Wang, X.; Ren, S.; Yang, J.; Zhao, D.; Xi, W.; Yao, L. Performance impact and poisoning mechanism of arsenic over commercial $V_2O_5–WO_3/TiO_2$ SCR catalyst. *Catal. Commun.* **2015**, *72*, 121–126. [CrossRef]
185. Zhang, H.; Kong, M.; Cai, Z.; Jiang, L.; Liu, Q.; Yang, J.; Ren, S.; Li, J.; Duan, M. Synergistic effect of arsenic and different potassium species on V_2O_5-WO_3/TiO_2 catalyst poisoning: Comparison of Cl^-, SO_4^{2-} and NO_3^- anions. *Catal. Commun.* **2020**, *144*, 106069. [CrossRef]
186. Li, L.; Chen, L.; Kong, M.; Liu, Q.; Ren, S. New insights into the deactivation mechanism of V_2O_5-WO_3/TiO_2 catalyst during selective catalytic reduction of NO with NH_3: Synergies between arsenic and potassium species. *RSC Adv.* **2019**, *9*, 37724–37732. [CrossRef]

187. Tian, Y.; Yang, J.; Liu, L.; Liu, Q.; Kong, B.; Lin, F.; Kong, M.; Hu, G. Insight into regeneration mechanism with sulfuric acid for arsenic poisoned commercial SCR catalyst. *J. Energy Inst.* **2020**, *93*, 387–394. [CrossRef]
188. Qi, L.; Li, J.; Yao, Y.; Zhang, Y. Heavy metal poisoned and regeneration of selective catalytic reduction catalysts. *J. Hazard. Mater.* **2019**, *366*, 492–500. [CrossRef] [PubMed]
189. Xue, Y.; Wang, Y. Effective industrial regeneration of arsenic poisoning waste selective catalytic reduction catalyst: Contaminants removal and activity recovery. *Environ. Sci. Pollut. Res.* **2018**, *25*, 34114–34122. [CrossRef] [PubMed]
190. Chapman, D.M. Behavior of titania-supported vanadia and tungsta SCR catalysts at high temperatures in reactant streams: Tungsten and vanadium oxide and hydroxide vapor pressure reduction by surficial stabilization. *Appl. Catal. A* **2011**, *392*, 143–150. [CrossRef]
191. Liu, Z.G.; Ottinger, N.A.; Cremeens, C.M. Vanadium and tungsten release from V-based selective catalytic reduction diesel aftertreatment. *Atmos. Environ.* **2015**, *104*, 154–161. [CrossRef]
192. Wu, W.C.; Tsai, T.Y.; Shen, Y.H. Tungsten recovery from spent SCR catalyst using alkaline leaching and ion exchange. *Minerals* **2016**, *6*, 107. [CrossRef]
193. Huo, Y.; Chang, Z.; Li, W.; Liu, S.; Dong, B. Reuse and valorization of vanadium and tungsten from waste V_2O_5–WO_3/TiO_2 SCR catalyst. *Waste Biomass Valor.* **2015**, *6*, 159–165. [CrossRef]
194. Giordano, F.; Trovarelli, A.; de Leitenburg, C.; Giona, M. A model for the temperature-programmed reduction of low and high surface area ceria. *J. Catal.* **2000**, *193*, 273–282. [CrossRef]
195. Montini, T.; Melchionna, M.; Monai, M.; Fornasiero, P. Fundamentals and catalytic applications of CeO_2-based materials. *Chem. Rev.* **2016**, *116*, 5987–6041. [CrossRef]
196. Martin, D.; Duprez, D. Mobility of surface species on oxides. 1. isotopic exchange of $^{18}O2$ with ^{16}O of SiO_2, Al_2O_3, ZrO_2, MgO, CeO_2, and CeO_2-Al_2O_3. activation by noble metals. correlation with oxide basicity. *J. Phys. Chem.* **1996**, *100*, 9429–9438. [CrossRef]
197. Madier, Y.; Descorme, C.; Le Govic, A.M.; Duprez, D. Oxygen mobility in CeO_2 and $Ce_xZr_{(1-x)}O_2$ compounds: Study by CO transient oxidation and $^{18}O/^{16}o$ isotopic exchange. *J. Phys. Chem. B* **1999**, *103*, 10999–11006. [CrossRef]
198. Liu, F.; Yu, Y.; He, H. Environmentally-benign catalysts for the selective catalytic reduction of NO_x from diesel engines: Structure–activity relationship and reaction mechanism aspects. *Chem. Commun.* **2014**, *50*, 8445–8463. [CrossRef] [PubMed]
199. Chen, L.; Li, J.; Ge, M. Promotional Effect of Ce-doped V_2O_5-WO_3/TiO_2 with low vanadium loadings for selective catalytic reduction of NO_x by NH_3. *J. Phys. Chem. C* **2009**, *113*, 21177–21184. [CrossRef]
200. Wang, X.; Shi, A.; Duan, Y.; Wang, J.; Shen, M. Catalytic performance and hydrothermal durability of CeO_2-V_2O_5-ZrO_2/WO_3-TiO_2 based NH_3-SCR catalysts. *Catal. Sci. Technol.* **2012**, *2*, 1386–1395. [CrossRef]
201. Shen, M.; Xu, L.; Wang, J.-Q.; Li, C.; Wang, W.; Wang, J.; Zhai, Y. Effect of synthesis methods on activity of V_2O_5/CeO_2/WO_3-TiO_2 catalyst for selective catalytic reduction of NO_x with NH_3. *J. Rare Earths* **2016**, *34*, 256–267. [CrossRef]
202. Youn, S.; Song, I.; Kim, D.H. Roles of promoters in V_2O_5/TiO_2 catalysts for selective catalytic reduction of NO_x with NH_3: Effect of order of impregnation. *J. Nanosci. Nanotechnol.* **2016**, *16*, 4350–4356. [CrossRef]
203. Liu, X.; Zhao, Z.; Ning, R.; Qin, Y.; Zhu, T.; Liu, F. Ce-Doped V_2O_5-WO_3/TiO_2 with Low Vanadium Loadings as SCR Catalysts and the Resistance of H_2O and SO_2. *Catal. Lett.* **2019**, *150*, 375–383. [CrossRef]
204. Tian, X.; Xiao, Y.; Zhang, W.; Luo, X. Investigation on performance of V_2O_5–WO_3–TiO_2–cordierite catalyst modified with Cu, Mn and Ce for urea-SCR of NO. *Mater. Res. Innov.* **2014**, *18*, 202–206. [CrossRef]
205. Liang, Q.; Li, J.; He, H.; Liang, W.; Zhang, T.; Fan, X. Effects of SO_2 on the low temperature selective catalytic reduction of NO by NH_3 over CeO_2-V_2O_5-WO_3/TiO_2 catalysts. *Front. Environ. Sci. Eng.* **2017**, *11*, 4. [CrossRef]
206. Zhao, X.; Mao, L.; Dong, G. Mn-Ce-V-WOx/TiO_2 SCR Catalysts: Catalytic activity, stability and interaction among catalytic oxides. *Catalysts* **2018**, *8*, 76. [CrossRef]
207. Cao, J.; Yao, X.; Yang, F.; Chen, L.; Fu, M.; Tang, C.; Dong, L. Improving the denitration performance and K-poisoning resistance of the V_2O_5-WO_3/TiO_2 catalyst by Ce^{4+} and Zr^{4+} co-doping. *Chin. J. Catal.* **2019**, *40*, 95–104. [CrossRef]
208. Chen, L.; Li, J.; Ge, M. DRIFT study on cerium-tungsten/titania catalyst for selective catalytic reduction of NO_x with NH_3. *Environ. Sci. Technol.* **2010**, *44*, 9590–9596. [CrossRef]
209. Chen, L.; Weng, D.; Wang, J.; Weng, D.; Cao, L. Low-temperature activity and mechanism of WO_3-modified CeO_2-TiO_2 catalyst under NH_3-NO/NO_2 SCR conditions. *Chin. J. Catal.* **2018**, *39*, 1804–1813. [CrossRef]
210. Geng, Y.; Shan, W.; Xiong, S.; Liao, Y.; Yang, S.; Liu, F. Effect of CeO_2 for a high-efficiency CeO_2/WO_3-TiO_2 catalyst on N_2O formation in NH_3-SCR: A kinetic study. *Catal. Sci. Technol.* **2016**, *6*, 3149–3155. [CrossRef]
211. Michalow-Mauke, K.A.; Lu, Y.; Ferri, D.; Graule, T.; Kowalski, K.; Elsener, M.; Kröcher, O. WO_3/CeO_2/TiO_2 catalysts for selective catalytic reduction of NO_x by NH_3: Effect of the synthesis method. *Chimia* **2015**, *69*, 220–224. [CrossRef]
212. Michalow-Mauke, K.A.; Lu, Y.; Kowalski, K.; Graule, T.; Nachtegaal, M.; Kröcher, O.; Ferri, D. Flame-made WO_3/CeO_x-TiO_2 catalysts for selective catalytic reduction of NO_x by NH_3. *ACS Catal.* **2015**, *5*, 5657–5672. [CrossRef]
213. Jiang, Y.; Xing, Z.; Wang, X.; Huang, S.; Wang, X.; Liu, Q. Activity and characterization of a Ce-W-Ti oxide catalyst prepared by a single step sol-gel method for selective catalytic reduction of NO with NH_3. *Fuel* **2015**, *151*, 124–129. [CrossRef]
214. Shan, W.; Liu, F.; He, H.; Shi, X.; Zhang, C. A superior Ce-W-Ti mixed oxide catalyst for the selective catalytic reduction of NO_x with NH_3. *Appl. Catal. B* **2012**, *115–116*, 100–106. [CrossRef]

215. Liu, J.; Xiong, Z.-B.; Zhou, F.; Lu, W.; Jin, J.; Ding, S.-F. Promotional effect of H_2O_2 modification on the cerium-tungsten-titanium mixed oxide catalyst for selective catalytic reduction of NO with NH_3. *J. Phys. Chem. Solids* **2018**, *121*, 360–366. [CrossRef]
216. Dankeaw, A.; Gualandris, F.; Silva, R.H.; Norrman, K.; Gudik-Sørensen, M.; Kammer Hansen, K.; Ksapabutr, B.; Esposito, V.; Marani, D. Amorphous saturated cerium–tungsten–titanium oxide nanofiber catalysts for NO_x selective catalytic reaction. *New J. Chem.* **2018**, *42*, 9501–9509. [CrossRef]
217. Salazar, M.; Becker, R.; Grünert, W. A close-up to the promoting effect of tungsten in Ce/TiO_2 catalysts for the selective catalytic reduction of NO with NH_3. *Mol. Catal.* **2018**, *451*, 66–75. [CrossRef]
218. Cao, L.; Wu, X.; Xu, Y.; Lin, Q.; Hu, J.; Chen, Y.; Ran, R.; Weng, D. Ceria-modified WO_3-TiO_2-SiO_2 monolithic catalyst for high-temperature NH_3-SCR. *Catal. Commun.* **2019**, *120*, 55–58. [CrossRef]
219. Zhang, Q.; Song, Z.; Ning, P.; Liu, X.; Li, H.; Gu, J. Novel promoting effect of acid modification on selective catalytic reduction of NO with ammonia over CeO_2 catalysts. *Catal. Commun.* **2015**, *59*, 170–174. [CrossRef]
220. Song, Z.; Zhang, Q.; Ning, P.; Fan, J.; Duan, Y.; Liu, X.; Huang, Z. Effect of CeO_2 support on the selective catalytic reduction of NO with NH_3 over $P\text{-}W/CeO_2$. *J. Taiwan Inst. Chem. Eng.* **2016**, *65*, 149–161. [CrossRef]
221. Wang, D.; Peng, Y.; Yang, Q.; Hu, F.; Li, J.; Crittenden, J. NH_3-SCR performance of WO_3 blanketed CeO_2 with different morphology: Balance of surface reducibility and acidity. *Catal. Today* **2019**, *332*, 42–48. [CrossRef]
222. Peng, R.; Sun, X.; Li, S.; Chen, L.; Fu, M.; Wu, J.; Ye, D. Shape effect of Pt/CeO_2 catalysts on the catalytic oxidation of toluene. *Chem. Eng. J.* **2016**, *306*, 1234–1246. [CrossRef]
223. Ma, Z.; Wu, X.; Feng, Y.; Si, Z.; Weng, D. Effects of WO_3 doping on stability and N_2O escape of MnO_x–CeO_2 mixed oxides as a low-temperature SCR catalyst. *Catal. Commun.* **2015**, *69*, 188–192. [CrossRef]
224. Daturi, M.; Finocchio, E.; Binet, C.; Lavalley, J.-C.; Fally, F.; Perrichon, V.; Vidal, H.; Hickey, N.; Kašpar, J. Reduction of high surface area CeO_2-ZrO_2 mixed oxides. *J. Phys. Chem. B* **2000**, *104*, 9186–9194. [CrossRef]
225. Aneggi, E.; Boaro, M.; de Leitenburg, C.; Dolcetti, G.; Trovarelli, A. Insights into the redox properties of ceria-based oxides and their implications in catalysis. *J. Alloy Compd.* **2006**, *408–412*, 1096–1102. [CrossRef]
226. Ning, P.; Song, Z.; Li, H.; Zhang, Q.; Liu, X.; Zhang, J.; Tang, X.; Huang, Z. Selective catalytic reduction of NO with NH_3 over CeO_2-ZrO_2-WO_3 catalysts prepared by different methods. *Appl. Surf. Sci.* **2015**, *332*, 130–137. [CrossRef]
227. Song, Z.; Yin, L.; Zhang, Q.; Ning, P.; Duan, Y.; Wang, J.; Liu, X.; Long, K.; Huang, Z. Relationship between the WO_3 states and reaction pathway over CeO_2-ZrO_2-WO_3 catalysts for selective catalytic reduction of NO with NH_3. *Mol. Catal.* **2017**, *437*, 95–104. [CrossRef]
228. Liu, S.; Lin, Q.; Liu, J.; Xu, S.; Wang, Y.; Xu, H.; Wang, J.; Chen, Y. Enhancement of the Hydrothermal Stability of $WO_3/Ce_{0.68}Zr_{0.32}O_2$ Catalyst by Silica Modification for NH_3-SCR. *ACS Appl. Energy Mater.* **2020**, *3*, 1161–1170. [CrossRef]
229. Xu, H.; Liu, S.; Wang, Y.; Lin, Q.; Lin, C.; Lan, L.; Wang, Q.; Chen, Y. Promotional effect of Al_2O_3 on WO_3/CeO_2-ZrO_2 monolithic catalyst for selective catalytic reduction of nitrogen oxides with ammonia after hydrothermal aging treatment. *Appl. Surf. Sci.* **2018**, *427*, 656–669. [CrossRef]
230. Can, F.; Berland, S.; Royer, S.; Courtois, X.; Duprez, D. Composition-dependent performance of Ce_xZr_{1-x} O_2 mixed-oxide supported WO_3 catalysts for the NO_x storage reduction-selective catalytic reduction coupled process. *ACS Catal.* **2013**, *3*, 1120–1132. [CrossRef]
231. Martin, N.; Vennestrom, P.N.R.; Thogersen, J.R.; Moliner, M.; Corma, A. Iron-containing SSZ-39 (AEI) zeolite: An active and stable high-temperature NH_3-SCR catalyst. *ChemCatChem* **2017**, *9*, 1754–1757. [CrossRef]
232. Li, X.; Li, J.; Peng, Y.; Zhang, T.; Liu, S.; Hao, J. Selective catalytic reduction of NO with NH_3 over novel iron–tungsten mixed oxide catalyst in a broad temperature range. *Catal. Sci. Technol.* **2015**, *5*, 4556–4564. [CrossRef]
233. Wang, H.; Qu, Z.; Dong, S.; Xie, H.; Tang, C. Superior performance of $Fe_{1-x}W_xO_\delta$ for the selective catalytic reduction of NO_x with NH_3: Interaction between Fe and W. *Environ. Sci. Technol.* **2016**, *50*, 13511–13519. [CrossRef]
234. Wang, H.; Qu, Z.; Dong, S.; Tang, C. Mechanistic investigation into the effect of sulfuration on the FeW catalysts for the selective catalytic reduction of NO_x with NH_3. *ACS Appl. Mater. Interfaces* **2017**, *9*, 7017−7028. [CrossRef]
235. Liu, F.; Shan, W.; Lian, Z.; Liu, J.; He, H. The smart surface modification of Fe_2O_3 by WO_x for significantly promoting the selective catalytic reduction of NO_x with NH_3. *Appl. Catal. B* **2018**, *230*, 165–176. [CrossRef]
236. Li, C.; Huang, Z.; Chen, Y.; Liu, X.; Chen, J.; Qu, W.; Ma, Z.; Tang, X. Optimizing selective catalytic reduction of NO with NH_3 on Fe_2O_3/WO_3 via redox-acid synergy. *ChemCatChem* **2018**, *10*, 3990–3994. [CrossRef]
237. Foo, R.; Vazhnova, T.; Lukyanov, D.B.; Millington, P.; Collier, J.; Rajaram, R.; Golunski, S. Formation of reactive Lewis acid sites on Fe/WO_3-ZrO_2 catalysts for higher temperature SCR applications. *Appl. Catal. B* **2015**, *162*, 174–179. [CrossRef]
238. Xu, H.; Li, Y.; Xu, B.; Cao, Y.; Feng, X.; Sun, M.; Gong, M.; Chen, Y. Effectively promote catalytic performance by adjusting W/Fe molar ratio of $FeW_x/Ce_{0.68}Zr_{0.32}O_2$ monolithic catalyst for NH_3-SCR. *J. Ind. Eng. Chem.* **2016**, *36*, 334–345. [CrossRef]
239. Xiong, Z.B.; Peng, B.; Zhou, F.; Wu, C.; Lu, W.; Jin, J.; Ding, S.F. Magnetic iron-cerium-tungsten mixed oxide pellets prepared through citric acid sol-gel process assisted by microwave irradiation for selective catalytic reduction of NO_x with NH_3. *Powder Technol.* **2017**, *319*, 19–25. [CrossRef]
240. Ma, S.; Zhao, X.; Li, Y.; Zhang, T.; Yuan, F.; Niu, X.; Zhu, Y. Effect of W on the acidity and redox performance of the $Cu_{0.02}Fe_{0.2}W_\alpha TiO_x$ (α= 0.01, 0.02, 0.03) catalysts for NH_3-SCR of NO. *Appl. Catal. B* **2019**, *248*, 226–238. [CrossRef]
241. Su, Y.; Dong, G.; Zhao, Y.; Zhang, Y.; Wang, Y. FeOx-VOx-WOx-MnO_x-CeOx/TiO_2 as a catalyst for selective catalytic reduction of NO_x with NH_3 and the role of iron. *Indian J. Chem.* **2015**, *54A*, 744–751.

242. Kong, Z.; Wang, C.; Ding, Z.; Chen, Y.; Zhang, Z. Enhanced activity of $Mn_xW_{0.05}Ti_{0.95-x}O_{2-\delta}$ for selective catalytic reduction of NO_x with ammonia by self-propagating high-temperature synthesis. *Catal. Commun.* **2015**, *64*, 27–31. [CrossRef]
243. Shin, B.; Lee, H.; Park, H. Catalytic Activity and surface characteristics of WO_3-doped MnO_x-TiO_2 catalysts for low-temperature selective catalytic reduction of NO_x with NH_3. *Korean J. Met. Mater.* **2016**, *54*, 787–792.
244. Wang, X.; Li, X.; Zhao, Q.; Sun, W.; Tade, M.; Liu, S. Improved activity of W-modified MnO_x–TiO_2 catalysts for the selective catalytic reduction of NO with NH_3. *Chem. Eng. J.* **2016**, *288*, 216–222. [CrossRef]
245. Phule, A.D.; Choi, J.H.; Kim, J.H. High performance of catalytic sheet filters of V_2O_5-WO_3/TiO_2 for NO_x reduction. *Environ. Sci. Pollut. Res.* **2020**. [CrossRef] [PubMed]
246. Zhang, D.; Ma, Z.; Wang, B.; Sun, Q.; Xu, W.; Zhu, T. Effects of MO_x (M=Mn, Cu, Sb, La) on V-Mo-Ce/Ti selective catalytic reduction catalysts. *J. Rare Earth* **2020**, *38*, 157–166. [CrossRef]
247. Nie, J.; Wu, X.; Ma, Z.; Xu, T.; Si, Z.; Chen, L.; Wen, D. Tailored temperature window of MnO_x-CeO_2 SCR catalyst by addition of acidic metal oxides. *Chin. J. Catal.* **2014**, *35*, 1281–1288. [CrossRef]
248. Zhang, T.; Qiu, F.; Chang, H.; Peng, Y.; Li, J. Novel W-modified SnMnCeOx catalyst for the selective catalytic reduction of NO_x with NH_3. *Catal. Commun.* **2017**, *100*, 117–120. [CrossRef]
249. Kwon, D.W.; Nam, K.B.; Hong, S.C. Influence of tungsten on the activity of a Mn/Ce/W/Ti catalyst for the selective catalytic reduction of NO with NH_3 at low temperatures. *Appl. Catal. A* **2015**, *497*, 160–166. [CrossRef]
250. Nam, K.B.; Kwon, D.W.; Hong, S.C. DRIFT study on promotion effects of tungsten-modified Mn/Ce/Ti catalysts for the SCR reaction at low-temperature. *Appl. Catal. A* **2017**, *542*, 55–62. [CrossRef]
251. Nam, K.B.; Kim, D.H.; Hong, S.C. Enhancement of Mn/Ce/W/Ti catalysts through control of pH and oxygen mobility during their preparation. *Appl. Catal. A* **2019**, *572*, 107–114. [CrossRef]
252. Liu, Z.; Liu, Y.; Li, Y.; Su, H.; Ma, L. WO_3 promoted Mn–Zr mixed oxide catalyst for the selective catalytic reduction of NO_x with NH_3. *Chem. Eng. J.* **2016**, *283*, 1044–1050. [CrossRef]
253. Zhang, R.; Liu, N.; Luo, Z.; Yang, W.; Liang, X.; Xu, R.; Chen, B.; Duprez, D.; Royer, S. A remarkable catalyst combination to widen the operating temperature window of the selective catalytic reduction of NO by NH_3. *ChemCatChem* **2014**, *6*, 2263–2269. [CrossRef]
254. Can, F.; Courtois, X.; Duprez, D. Chapter 3 NSR catalytic materials. In *NO_x Trap Catalysts and Technologies: Fundamentals and Industrial Applications*; Catalysis Series; Lietti, L., Castoldi, L., Eds.; RSC Publishing: Cambridge, UK, 2018; pp. 67–103.
255. Can, F.; Courtois, X.; Royer, S.; Blanchard, G.; Rousseau, S.; Duprez, D. An overview of the production and use of ammonia in NSR + SCR coupled system for NO_x reduction from lean exhaust gas. *Catal. Today* **2012**, *197*, 144–154. [CrossRef]
256. Shinjoh, H.; Takahashi, N.; Yokota, K. Synergic effect of Pd/gamma-alumina and Cu/ZSM-5 on the performance of NO_x storage reduction catalyst. *Top. Catal.* **2007**, *42–43*, 215–219. [CrossRef]
257. Corbos, E.C.; Haneda, M.; Courtois, X.; Marecot, P.; Duprez, D.; Hamada, H. NO_x abatement for lean burn engines under lean-rich atmosphere over mixed NSR-SCR catalysts: Influences of the addition of a SCR catalyst and of the operational conditions. *Appl. Catal. A* **2009**, *365*, 187–193. [CrossRef]
258. De La Torre, U.; Pereda-Ayo, B.; Moliner, M.; González-Velasco, J.R.; Corma, A. Cu-zeolite catalysts for NO_x removal by selective catalytic reduction with NH_3 and coupled to NO storage/reduction monolith in diesel engine exhaust aftertreatment systems. *Appl. Catal. B* **2016**, *187*, 419–427. [CrossRef]
259. Cortés-Reyes, M.; Herrera, C.; Larrubia, M.Á.; Alemany, L.J. Hybrid technology for DeNOxing by LNT-SCR system for efficient diesel emission control: Influence of operation parameters in H_2O + CO_2 atmosphere. *Catalysts* **2020**, *10*, 228. [CrossRef]
260. Zukerman, R.; Vradman, L.; Herskowitz, M.; Liverts, E.; Liverts, M.; Massner, A.; Weibel, M.; Brilhac, J.F.; Blakeman, P.G.; Peace, L.J. Modeling and simulation of a smart catalytic converter combining NO_x storage, ammonia production and SCR. *Chem. Eng. J.* **2009**, *155*, 419–426. [CrossRef]
261. Castoldi, L.; Bonzi, R.; Lietti, L.; Forzatti, P.; Morandi, S.; Ghiotti, G.; Dzwigaj, S. Catalytic behaviour of hybrid LNT/SCR systems: Reactivity and in situ FTIR study. *J. Catal.* **2011**, *282*, 128–144. [CrossRef]
262. Can, F.; Courtois, X.; Berland, S.; Seneque, M.; Royer, S.; Duprez, D. Composition dependent performance of alumina-based oxide supported WO_3 catalysts for the NH_3-SCR reaction and the NSR + SCR coupled process. *Catal. Today* **2015**, *257*, 41–50. [CrossRef]
263. Väliheikki, A.; Petallidou, K.C.; Kalamaras, C.M.; Kolli, T.; Huuhtanen, M.; Maunula, T.; Keiski, R.L.; Efstathiou, A.M. Selective catalytic reduction of NO_x by hydrogen (H_2-SCR) on WO_x-promoted $Ce_zZr_{1-z}O_2$ solids. *Appl. Catal. B* **2014**, *156–157*, 72–83. [CrossRef]
264. Shibata, J.; Hashimoto, M.; Shimizu, K.I.; Yoshida, H.; Hattori, T.; Satsuma, A. Factors Controlling activity and selectivity for SCR of NO by hydrogen over supported platinum catalysts. *J. Phys. Chem. B* **2004**, *108*, 18327–18335. [CrossRef]
265. Costa, C.N.; Efstathiou, A.M. Mechanistic Aspects of the H_2-SCR of NO on a Novel Pt/MgO-CeO_2 Catalyst. *J. Phys. Chem. C* **2007**, *111*, 3010–3020. [CrossRef]
266. Savva, P.G.; Costa, C.N. Hydrogen Lean-$DeNO_{(x)}$ as an alternative to the ammonia and hydrocarbon selective catalytic reduction (SCR). *Catal. Rev. Sci. Eng.* **2011**, *53*, 91–151. [CrossRef]
267. Schott, F.J.P.; Balle, P.; Adler, J.; Kureti, S. Reduction of NO_x by H_2 on Pt/WO_3/ZrO_2 catalysts in oxygen-rich exhaust. *Appl. Catal. B* **2009**, *87*, 18–29. [CrossRef]
268. Yang, S.; Wang, X.; Chu, W.; Song, Z.; Zhao, S. An investigation of the surface intermediates of H_2-SCR of NO_x over Pt/H-FER. *Appl. Catal. B* **2011**, *107*, 380–385. [CrossRef]

269. Zhang, X.; Wang, X.; Zhao, X.; Xu, Y.; Liu, Y.; Yu, Q. Promotion effect of tungsten on the activity of Pt/HZSM-5 for H_2-SCR. *Chem. Eng. J.* **2015**, *260*, 419–426. [CrossRef]
270. Sun, M.; Wang, S.; Li, Y.; Xu, H.; Chen, Y. Promotion of catalytic performance by adding W into Pt/ZrO_2 catalyst for selective catalytic oxidation of ammonia. *Appl. Surf. Sci.* **2017**, *402*, 323–329. [CrossRef]
271. Wang, H.; Ning, P.; Zhang, Q.; Liu, X.; Zhang, T.; Fan, J.; Wang, J.; Long, K. Promotional mechanism of WO_3 over RuO_2-Fe_2O_3 catalyst for NH_3-SCO reaction. *Appl. Catal. A* **2018**, *561*, 158–167. [CrossRef]
272. Miyadera, T. Alumina-supported silver catalysts for the selective reduction of nitric oxide with propene and oxygen-containing organic compounds. *Appl. Catal. B* **1993**, *2*, 199–205. [CrossRef]
273. Bion, N.; Saussey, J.; Hedouin, C.; Seguelong, T.; Daturi, M. Evidence by in situ FTIR spectroscopy and isotopic effect of new assignments for isocyanate species vibrations on Ag/Al_2O_3. *Phys. Chem. Chem. Phys.* **2011**, *3*, 4811–4816. [CrossRef]
274. Bion, N.; Saussey, J.; Haneda, M.; Daturi, M. Study by in situ FTIR spectroscopy of the SCR of NO_x by ethanol on Ag/Al_2O_3-Evidence of the role of isocyanate species. *J. Catal.* **2003**, *217*, 47–58. [CrossRef]
275. Kameoka, S.; Ukisu, Y.; Miyadera, T. Selective catalytic reduction of NO_x with and CH_3OH, C_2H_5OH and C_3H_6 in the presence of O_2 over Ag/Al_2O_3 catalyst: Role of surface nitrate species. *Phys. Chem. Chem. Phys.* **2000**, *2*, 367–372. [CrossRef]
276. Yeom, Y.H.; Li, M.; Sachtler, W.M.H.; Weitz, E. A study of the mechanism for NO_x reduction with ethanol on γ-alumina supported silver. *J. Catal.* **2006**, *238*, 100–110. [CrossRef]
277. Barreau, M.; Tarot, M.-L.; Duprez, D.; Courtois, X.; Can, F. Remarkable enhancement of the selective catalytic reduction of NO at low temperature by collaborative effect of ethanol and NH_3 over silver supported catalyst. *Appl. Catal. B* **2018**, *220*, 19–30. [CrossRef]
278. Barreau, M.; Delporte, M.; Iojoiu, E.; Courtois, X.; Can, F. Lean NO_x removal by a bifunctional (EtOH + NH_3) mixture dedicated to (Ag/Al_2O_3+ NH_3-SCR) dual-bed catalytic system: Comparison between WO_3/$CeZrO_2$ and Cu–FER as NH_3-SCR catalyst. *Top. Catal.* **2019**, *62*, 79–85. [CrossRef]
279. Barreau, M.; Courtois, X.; Can, F. Selective catalytic reduction of NO at low temperature using a (ethanol+ammonia) mixture over a Ag/Al_2O_3+WO_3/$Ce_xZr_yO_2$ dual-bed catalytic system: Reactivity insight of WO_3/$Ce_xZr_yO_2$. *Catal. Today* **2020**, *355*, 375–384. [CrossRef]
280. Altman, E.I.; Schwarz, U.D. Mechanisms, Kinetics, and Dynamics of Oxidation and Reactions on Oxide Surfaces Investigated by Scanning Probe Microscopy. *Adv. Mater.* **2010**, *22*, 2854–2869. [CrossRef]
281. Balzer, R.; Drago, V.; Schreiner, W.H.; Probst, L.F.D. Synthesis and structure-activity relationship of a WO_3 catalyst for the total oxidation of BTX. *J. Braz. Chem. Soc.* **2014**, *25*, 2026–2031.
282. Pansare, S.S.; Goodwin, J.G., Jr.; Gangwal, S. Simultaneous ammonia and toluene decomposition on tungsten-based catalysts for hot gas cleanup. *Ind. Eng. Chem. Res.* **2008**, *47*, 8602–8611. [CrossRef]
283. Debecker, D.P.; Delaigle, R.; Bouchmella, K.; Eloy, P.; Gaigneaux, E.M.; Mutin, P.H. Total oxidation of benzene and chlorobenzene with MoO_3- and WO_3-promoted V_2O_5/TiO_2 catalysts prepared by a nonhydrolytic sol-gel route. *Catal. Today* **2010**, *157*, 125–130. [CrossRef]
284. Lu, S.-Y.; Wang, Q.-L.; Stevens, W.R.; Lee, C.W.; Gullett, B.K.; Zhao, Y.-X. Study on the decomposition of trace benzene over V_2O_5–WO_3/TiO_2-based catalysts in simulated flue gas. *Appl. Catal. B* **2014**, *147*, 322–329. [CrossRef]
285. Gullett, B.; Touati, A.; Oudejans, L. Use of REMPI–TOFMS for real-time measurement of trace aromatics during operation of aircraft ground equipment. *Atmos. Environ.* **2008**, *42*, 2117–2128. [CrossRef]
286. Gancheva, M.; Naydenov, A.; Iordanova, R.; Nihtianova, D.; Stefanov, P. Mechanochemically assisted solid state synthesis, characterization, and catalytic properties of $MgWO_4$. *J. Mater. Sci.* **2015**, *50*, 3447–3456. [CrossRef]
287. Blanch-Raga, N.; Soriano, M.D.; Palomares, A.E.; Concepción, P.; Martínez-Triguero, J.; López-Nieto, J.M. Catalytic abatement of trichloroethylene over Mo and/or W-based bronzes. *Appl. Catal. B* **2013**, *130–131*, 36–43. [CrossRef]
288. Haneda, M.; Suzuki, K.; Sasaki, M.; Hamada, H.; Ozawa, M. Catalytic performance of bimetallic PtPd/Al_2O_3 for diesel hydrocarbon oxidation and its implementation by acidic additives. *Appl. Catal. A* **2014**, *475*, 109–115. [CrossRef]
289. Le, Y.; Qi, L.F.; Wang, C.; Song, S.X. Hierarchical Pt/WO_3 nanoflakes assembled hollow microspheres for room-temperature formaldehyde oxidation activity. *Appl. Surf. Sci.* **2020**, *512*, 145763. [CrossRef]
290. Fukushi, D.; Sato, A.; Kusaka, T.; Kataoka, Y.; Kobayashi, K. Enhancing the rate of organic material decomposition photo catalyzed by high performance visible light activated tungsten oxide. *ECS Trans.* **2014**, *61*, 43–49. [CrossRef]
291. Fukushi, D.; Sato, A.; Yoshida, K.; Kitano, M. Decomposition of gas-phase organic pollutants over nanocrystalline tungsten oxide photocatalysts under visible-light irradiation. *Bull. Chem. Soc. Jpn.* **2017**, *90*, 885–892. [CrossRef]
292. Fukumura, T.; Sambandan, E.; Yamashita, H. Synthesis and VOC degradation ability of a CeO_2/WO thin-layer visible-light photocatalyst. *Mater. Res. Bull.* **2017**, *94*, 493–499. [CrossRef]
293. Balayeva, N.O.; Fleisch, M.; Bahnemann, D.W. Surface-grafted WO_3/TiO_2 photocatalysts: Enhanced visible-light activity towards indoor air purification. *Catal. Today* **2018**, *313*, 63–71. [CrossRef]
294. Caudillo-Flores, U.; Munoz-Batista, M.J.; Hungria, A.B.; Haro, M.L.; Fernandez-Garcia, M.; Kubacka, A. Toluene and styrene photo-oxidation quantum efficiency: Comparison between doped and composite tungsten-containing anatase-based catalysts. *Appl. Catal. B* **2019**, *245*, 49–61. [CrossRef]
295. Li, Y.; Wu, X.; Li, J.; Wang, K.; Zhang, G. Z-scheme g-C_3N_4@CsxWO_3 heterostructure as smart window coating for UV isolating, Vis penetrating, NIR shielding and full spectrum photocatalytic decomposing VOCs. *Appl. Catal. B* **2018**, *229*, 218–226. [CrossRef]

296. Dong, C.; Zhao, R.; Yao, L.; Ran, Y.; Zhang, X.; Wang, Y. A review on WO_3 based gas sensors: Morphology control and enhanced sensing properties. *J. Alloy Compd.* **2020**, *820*, 153194. [CrossRef]
297. Rickerby, D.G. Metal oxides: Nanostructured metal oxide for gas sensing application. In *CRC Concise Encyclopedia of Nanotechnology*; Ildusovich Kharisov, B., Kharissova, O.V., Ortiz-Mendez, U., Eds.; CRC Press: Boca Raton, FL, USA, 2016; pp. 481–492.
298. Kaur, M.; Aswal, D.K.; Yakhmi, J.V. Chapter 2 Chemiresistor Gas Sensors: Materials, mechanisms and fabrication. In *Science and Technology of Chemiresistor Gas Sensors*; Aswal, D.K., Gupta, S.K., Eds.; Nova Publishers: Hauppauge, NY, USA, 2007; pp. 33–94.
299. Gardner, J.W. Electrical conduction in solid-state gas sensors. *Sens. Actuators* **1989**, *18*, 373–387. [CrossRef]
300. Gardner, J.W. Detection of vapours and odours from a multisensor array using pattern recognition Part 1. Principal component and cluster analysis. *Sens. Actuators B* **1991**, *4*, 109–115. [CrossRef]
301. Han, X.; Yin, X. Density functional theory study of the NO2-sensing mechanism on a WO3 (0 0 1) surface: The role of surface oxygen vacancies in the formation of NO and NO3. *Mol. Phys.* **2016**, *114*, 3546–3555. [CrossRef]
302. Yang, L.; Marikutsa, A.; Rumyantseva, M.; Konstantinova, E.; Khmelevsky, N.; Gaskov, A. Quasi similar routes of NO_2 and NO sensing by nanocrystalline WO_3: Evidence by in situ DRIFT spectroscopy. *Sensors* **2019**, *19*, 3405. [CrossRef]
303. Chandrasekaran, G.; Sundararaj, A.; Therese, H.A.; Jeganathan, K. Ni-catalysed WO_3 nanostructures grown by electron beam rapid thermal annealing for NO_2 gas sensing. *J. Nanopart Res.* **2015**, *17*, 292. [CrossRef]
304. Li, J.; Liu, X.; Cui, J.; Sun, J. Hydrothermal synthesis of self-assembled hierarchical tungsten oxides hollow spheres and their gas sensing properties. *ACS Appl. Mater. Interfaces* **2015**, *7*, 10108–10114. [CrossRef] [PubMed]
305. Zhang, Y.; Cheng, X.; Zhang, X.; Major, Z.; Xu, Y.; Gao, S.; Zhao, H.; Huo, L. Ionic liquid-assisted synthesis of tungsten oxide nanoparticles with enhanced NO_2 sensing properties at near room temperature. *Appl. Surf. Sci.* **2020**, *505*, 144533. [CrossRef]
306. Cao, P.J.; Li, M.; Rao, C.N.; Han, S.; Xu, W.-Y.; Fang, M.; Liu, X.-K.; Zeng, Y.-X.; Liu, W.J.; Zhu, D.L.; et al. High Sensitivity NO_2 Gas Sensor Based on 3D WO_3 Microflowers Assembled by Numerous Nanoplates. *J. Nanosci. Nanotechnol.* **2020**, *20*, 1790–1798. [CrossRef]
307. Liu, D.; Ren, X.; Li, Y.; Tang, Z.; Zhang, Z. Nanowires-assembled WO_3 nanomesh for fast detection of ppb-level NO_2 at low temperature. *J. Adv. Ceram.* **2020**, *9*, 17–26. [CrossRef]
308. Lu, N.; Yang, C.; Liu, P.; Su, X. Preparation of 2 nm tungsten oxide nanowires based on two-phase strategy and their ultra-sensitive NO_2 gas sensing properties. *J. Colloid Interfaces Sci.* **2019**, *557*, 311–317. [CrossRef]
309. Song, W.; Zhang, R.; Bai, X.; Jia, Q.; Ji, H. Exposed crystal facets of WO_3 nanosheets by phase control on NO_2-sensing performance. *J. Mater. Sci. Mater. Electr.* **2020**, *31*, 610–620. [CrossRef]
310. Zheng, E.X.; Zhang, C.; Xia, J.; Zhou, G.; Jiang, D.; Wang, S.; Li, X.; Shen, Y.; Dai, M.; Wang, B.; et al. Mesoporous tungsten oxide electrodes for YSZ-based mixed potential sensors to detect NO_2 in the sub ppm-range. *Sens. Actuators B Chem.* **2019**, *284*, 575–581. [CrossRef]
311. Ma, S.; Hu, M.; Zeng, P.; Yan, W.; Li, M. Growth of tungsten oxide nanorods onto porous silicon and their sensing properties for NO2. *Mater. Lett.* **2013**, *99*, 57–60. [CrossRef]
312. Ma, S.; Hu, M.; Zeng, P.; Li, M.; Yan, W.; Li, C. Synthesis of tungsten oxide nanowires/porous silicon composites and their application in NO2 sensors. *Mater. Lett.* **2013**, *112*, 12–15. [CrossRef]
313. Ma, S.; Hu, M.; Zeng, P.; Li, M.; Yan, W.; Qin, Y. Synthesis and low-temperature gas sensing properties of tungstenoxide nanowires/porous silicon composite. *Sens. Actuators B Chem.* **2014**, *192*, 341–349. [CrossRef]
314. Li, M.; Hu, M.; Jia, D.; Ma, S.; Yan, W. NO2-sensing properties based on the nanocomposite of n-WO3−x/n-porous silicon at room temperature. *Sens. Actuators B Chem.* **2013**, *186*, 140–147. [CrossRef]
315. Lee, K.; Beak, D.-H.; Na, H.; Choi, J.; Kim, J. Simple fabrication method of silicon/tungsten oxide nanowires heterojunction for NO_2 gas sensors. *Sens. Actuators B Chem.* **2018**, *265*, 522–528. [CrossRef]
316. Godbole, R.; Vedpathak, A.; Godbole, V.; Bhagwat, S. Tungsten oxide thin films: Detection and trapping of hazardous gases. *Mater. Res. Express* **2017**, *4*, 1–7. [CrossRef]
317. Najafi-Ashtiani, H. The effect of different surface morphologies on WO_3 and WO_3-Au gas-sensors performance. *J. Mater. Sci. Mater. Electr.* **2019**, *30*, 12224–12233. [CrossRef]
318. Kim, T.H.; Hasani, A.; Quyet, L.V.; Kim, Y.; Park, S.Y.; Lee, M.G.; Sohn, W.; Nguyen, T.P.; Choi, K.S.; Kim, S.Y.; et al. NO_2 sensing properties of porous Au-incorporated tungsten oxide thin films prepared by solution process. *Sens. Actuators B Chem.* **2019**, *286*, 512–520. [CrossRef]
319. Urasinska-Wojcik, B.; Vincent, T.A.; Chowdhury, M.F.; Gardner, J.W. Ultrasensitive WO3 gas sensors for NO2 detection in air and low oxygen environment. *Sens. Actuators B Chem.* **2017**, *239*, 1051–1059. [CrossRef]
320. Staerz, A.; Berthold, C.; Russ, T.; Wicker, S.; Weimar, U.; Barsan, N. The oxidizing effect of humidity on WO3 based sensors. *Sens. Actuators B Chem.* **2016**, *237*, 54–58. [CrossRef]
321. Sevastyanov, E.Y.; Maksimova, N.K.; Rudov, F.V.; Sergeichenko, N.V.; Chernikov, E.V. Effect of humidity on the properties of NO2 sensors based on thin WO3 and SnO2 films modified with gold. *Russ. J. Phys. Chem. A* **2015**, *89*, 447–452. [CrossRef]
322. Zhao, S.; Shen, Y.; Zhou, P.; Zhong, X.; Han, C.; Zhao, Q.; Wei, D. Design of Au@WO_3 core—Shell structured nanospheres for ppb-level NO_2 sensing. *Sens. Actuators B Chem.* **2019**, *282*, 917–926. [CrossRef]
323. Zhang, H.; Wang, Y.; Zhu, X.; Li, Y.; Cai, W. Bilayer Au nanoparticle-decorated WO_3 porous thin films: On-chip fabrication and enhanced NO_2 gas sensing performances with high selectivity. *Sens. Actuators B Chem.* **2019**, *280*, 192–200. [CrossRef]

324. Almaev, A.V.; Yakovlev, N.N.; Chernikov, E.V.; Tolbanov, O.P. Selective sensors of nitrogen dioxide based on thin tungsten oxide films under optical irradiation. *Tech. Phys. Lett.* **2019**, *45*, 1016–1019. [CrossRef]
325. Chmela, O.; Sadilek, J.; Domenech-Gil, G.; Sama, J.; Somer, J.; Mohan, R.; Romano-Rodriguez, A.; Hubalek, J.; Vallejos, S. Selectively arranged single-wire based nanosensor array systems for gas monitoring. *Nanoscale* **2018**, *10*, 9087–9096. [CrossRef]
326. Kim, D.-H.; Jung, J.-W.; Choi, S.-J.; Jang, J.-S.; Koo, W.-T.; Kim, I.-D. Pt nanoparticles functionalized tungsten oxynitride hybrid chemiresistor: Low-temperature NO_2 sensing. *Sens. Actuators B Chem* **2018**, *273*, 1269–1277. [CrossRef]
327. Lu, R.; Zhong, X.; Shang, S.; Wang, S.; Tang, M. Effects of sintering temperature on sensing properties of WO_3 and Ag-WO_3 electrode for NO_2 sensor. *R. Soc. Open Sci.* **2018**, *5*, 171691. [CrossRef]
328. Kamble, C.; Panse, M.; Nimbalkar, A. Ag decorated WO_3 sensor for the detection of sub-ppm level NO_2 concentration in air. *Mater. Sci. Semicon. Proc* **2019**, *103*, 104613. [CrossRef]
329. Jaroenapibal, P.; Boonma, P.; Saksilaporn, N.; Horprathum, M.; Amornkitbamrung, V.; Triroj, N. Improved NO_2 sensing performance of electrospun WO_3 nanofibers with silver doping. *Sens. Actuators B Chem.* **2018**, *255*, 1831–1840. [CrossRef]
330. Li, T.; Shen, Y.; Zhong, X.; Zhao, S.; Li, G.; Cui, B.; Wei, D.; Wei, K. Effect of noble metal element on microstructure and NO_2 sensing properties of WO_3 nanoplates prepared from a low-grade scheelite concentrate. *J. Alloy Compd.* **2020**, *818*, 152927. [CrossRef]
331. Liu, H.; Xu, Y.; Zhang, X.; Zhao, W.; Ming, A.; Wei, F. NO_2 gas sensing properties of Pd/WO_3 films prepared by glancing angle deposition. *J. Mater. Sci. Mater. Electr.* **2020**, *31*, 5827–5832. [CrossRef]
332. Van, P.T.H.; Thanh, N.H.; Quang, V.V.; Duy, N.V.; Hoa, N.D.; Hieu, N.V. Scalable fabrication of high-performance NO2 Gas sensors based on tungsten oxide nanowires by on-chip growth and RuO2-functionalization. *ACS Appl. Mater. Interfaces* **2014**, *6*, 12022–12030.
333. Zhang, Z.; Haq, M.; Wen, Z.; Ye, Z.; Zhu, L. Ultrasensitive ppb-level NO_2 gas sensor based on WO_3 hollow nanospheres doped with Fe. *Appl. Surf. Sci.* **2018**, *434*, 891–897. [CrossRef]
334. Haiduk, D.Y.S.; Khort, A.A.; Lapchuk, N.M.; Savitsky, A.A. Study of WO_3-In_2O_3 nanocomposites for highly sensitive CO and NO_2 gas sensors. *J. Solid State Chem.* **2019**, *273*, 25–31. [CrossRef]
335. Qi, J.; Chen, K.; Xing, Y.; Fan, H.; Zhao, H.; Yang, J.; Li, L.; Yan, B.; Zhou, J.; Guo, L.; et al. Application of 3D hierarchical monoclinic-type structural Sb-doped WO_3 towards NO_2 gas detection at low temperature. *Nanoscale* **2018**, *10*, 7440–7450. [CrossRef] [PubMed]
336. Guo, W.L.; Xie, N.; Kou, X.; Sun, Y.; Chuai, X.; Zhang, S.; Song, H.; Wang, Y.; Lu, G. Enhanced nitrogen oxide sensing performance based on tin-doped tungsten oxide nanoplates by a hydrothermal method. *J. Colloid Interface Sci.* **2018**, *512*, 740–749.
337. Shujah, T.; Ikram, M.; Butt, A.R.; Shahzad, M.K.; Rashid, K.; Zafar, Q.; Ali, S. H_2S Gas sensor based on WO_3 nanostructures synthesized via aerosol assisted chemical vapor deposition technique. *Nanosci. Nanotechnol. Lett.* **2019**, *11*, 1247–1256. [CrossRef]
338. Wang, Q.; Huang, J.; Zhou, J.; Liu, Z.; Gen, Y.; Liang, Z.; Du, Y.; Tian, X. Different nanostructured tungsten oxides synthesized by facile solvothermal route for chlorine gas sensing. *Sens. Actuators B Chem.* **2018**, *275*, 306–311. [CrossRef]
339. Sachdeva, S.; Agarwal, R.; Agarwal, A. Effect of annealing on tungsten oxide thin films for acetone gas detection. *Bull. Mater. Sci.* **2018**, *41*, 105. [CrossRef]
340. Sachdeva, S.; Agarwal, A.; Agarwal, R. A comparative study of gas sensing properties of tungsten oxide, tin oxide and tin-doped tungsten oxide thin films for acetone gas detection. *J. Electron. Mater.* **2019**, *48*, 1617–1628. [CrossRef]
341. Zanetti, S.M.; Rocha, K.O.; Rodrigues, J.A.J.; Longo, E. Soft-chemical synthesis, characterization and humidity sensing behavior of WO_3/TiO_2 nanopowders. *Sens. Actuators B Chem.* **2014**, *190*, 40–47. [CrossRef]
342. Faia, P.M.; Libardi, J. Response to humidity of TiO2: WO3 sensors doped with V2O5: Influence of fabrication route. *Sens. Actuators B Chem.* **2016**, *236*, 682–700. [CrossRef]
343. Godbole, R.; Godbole, V.; Bhagwat, S. Palladium enriched tungsten oxide thin films: An efficient gas sensor for hazardous gases. *Eur. Phys. J. B* **2019**, *92*, 78. [CrossRef]
344. Navarrete, E.; Bittencourt, C.; Umek, P.; Cossement, D.; Guell, F.; Llobet, E. Tungsten trioxide nanowires decorated with iridium oxide nanoparticles as gas sensing material. *J. Alloy Compd.* **2020**, *812*, 152156. [CrossRef]
345. Vallejos, S.; Umek, P.; Stoycheva, T.; Annanouch, F.; Llobet, E.; Correig, X.; De Marco, P.; Bittencourt, C.; Blackman, C. Single-step deposition of Au- and Pt-nanoparticle-functionalized tungsten oxide nanoneedles synthesized via aerosol-assisted CVD, and used for fabrication of selective gas microsensor arrays. *Adv. Funct. Mater.* **2013**, *23*, 1313–1322. [CrossRef]
346. Liu, S.; Liang, L.; Zhang, Q.; Liu, C.; Xing, W.; Dong, X. Reductive-heat-treated platinum tungsten oxide catalyst with improved CO oxidation activity and CO gas sensing property. *Anal. Methods* **2019**, *11*, 1811–1815. [CrossRef]
347. Xu, Y.; Ma, T.; Zhao, Y.; Zheng, L.; Liu, X.; Zhang, J. Multi-metal functionalized tungsten oxide nanowires enabling ultra-sensitive detection of triethylamine. *Sens. Actuators B Chem.* **2019**, *300*, 127042. [CrossRef]
348. Yamaguchi, Y.; Imamura, S.; Ito, S.; Nishio, K.; Fujimoto, K. Influence of oxygen gas concentration on hydrogen sensing of Pt/WO_3 thin film prepared by sol–gel process. *Sens. Actuators B Chem.* **2015**, *216*, 394–401. [CrossRef]
349. Paza, E.C.; Aveiro, L.R.; Pinheiro, V.S.; Souza, F.M.; Lima, V.B.; Silva, F.L.; Hammer, P.; Lanza, M.R.V.; Santos, M.C. Evaluation of H_2O_2 electrogeneration and decolorization of Orange II azo dye using tungsten oxide nanoparticle-modified carbon. *Appl. Catal. B* **2018**, *232*, 436–445. [CrossRef]
350. Guo, W.-Z.; Lu, H.; Li, X.-K.; Cao, G.-P. Tungsten-promoted titania as solid acid for catalytic hydrolysis of waste bottle PET in supercritical CO_2. *RSC Adv.* **2016**, *6*, 43171–43184. [CrossRef]

351. Li, W.; Xia, F.; Qu, J.; Li, P.; Chen, D.; Chen, Z.; Yu, Y.; Lu, Y.; Caruso, R.A.; Song, W. Versatile inorganic–organic hybrid WOx–ethylenediamine nanowires: Synthesis, mechanism and application in heavy metal ion adsorption and catalysis. *Nano Res.* **2014**, *7*, 903–916. [CrossRef]
352. Dong, P.; Hou, G.; Xi, X.; Shao, R.; Dong, F. WO_3-based photocatalysts: Morphology control, activity enhancement and multifunctional applications. *Environ. Sci. Nano* **2017**, *4*, 539–557. [CrossRef]
353. Gusaina, R.; Gupta, K.; Joshia, P.; Khatri, O.P. Adsorptive removal and photocatalytic degradation of organic pollutants using metal oxides and their composites: A comprehensive review. *Adv. Colloid Interface Sci.* **2019**, *272*, 102009. [CrossRef]
354. Quan, H.Q.; Gao, Y.F.; Wang, W.Z. Tungsten oxide-based visible light-driven photocatalysts: Crystal and electronic structures and strategies for photocatalytic efficiency enhancement. *Inorg. Chem. Front.* **2020**, *7*, 817–838. [CrossRef]
355. Xie, Y.P.; Liu, G.; Yin, L.; Cheng, H.M. Crystal facet-dependent photocatalytic oxidation and reduction reactivity of monoclinic WO_3 for solar energy conversion. *J. Mater. Chem.* **2012**, *22*, 6746–6751. [CrossRef]
356. Rey, A.; Mena, E.; Chávez, A.M.; Beltrán, F.J.; Medina, F. Influence of structural properties on the activity of WO_3 catalysts for visible light photocatalytic ozonation. *Chem. Eng. Sci.* **2015**, *126*, 80–90. [CrossRef]
357. Chen, P.; Qin, M.; Chen, Z.; Jia, B.; Qu, X. Solution combustion synthesis of nanosized WO_x: Characterization, mechanism and excellent photocatalytic properties. *RSC Adv.* **2016**, *6*, 83101–83109. [CrossRef]
358. Shang, J.; Xiao, Z.L.; Yu, L.X.; Aprea, P.; Hao, S.Y. An insight on the role of PVP in the synthesis of monoclinic WO_3 with efficiently photocatalytic activity. *Nanotechnology* **2020**, *31*, 125603. [CrossRef]
359. Zhang, H.; Yang, J.; Li, D.; Guo, W.; Qin, Q.; Zhu, L.; Zheng, W. Template-free facile preparation of monoclinic WO3 nanoplates and their high photocatalytic activities. *Appl. Surf. Sci.* **2014**, *305*, 274–280. [CrossRef]
360. Zhang, Y.; Zhang, R.C.; Zhao, L.; Xu, X.Y. Characterization and the removal efficiency of Rhodamine B by monoclinic and hexagonal WO_3 with oxidized and partially reduced states. *Mater. Res. Express* **2019**, *6*, 025008. [CrossRef]
361. Lu, Y.; Zhang, J.; Wang, F.; Chen, X.; Feng, Z.; Li, C. K_2SO_4-assisted hexagonal/monoclinic WO_3 phase junction for efficient photocatalytic degradation of RhB. *ACS Appl. Energy Mater.* **2018**, *1*, 2067–2077. [CrossRef]
362. Li, Z.; Zhou, Y.; Yao, Q.; Wang, W.; Wang, H.; Wang, D.; Liu, X.; Xu, J. Facile synthesis of WO_3 nanocuboids from tungsten trioxide powder and hydrogen peroxide. *Mater. Lett.* **2019**, *236*, 197–200. [CrossRef]
363. Yamamoto, A.; Tanaka, A.; Kominami, H.; Fujioka, D.; Sanada, T.; Kojima, K. Synthesis of disk-shaped tungsten(VI) oxide particles with various physical properties for mineralization of acetic acid in water under irradiation of visible light. *J. Nanosci. Nanotechnol.* **2020**, *20*, 4131–4137. [CrossRef] [PubMed]
364. Wang, C.; Li, A.; Li, C.; Zhang, S.B.; Li, H.; Zhou, X.Y.; Hu, L.M.; Feng, Y.; Wang, K.W.; Zhu, Z.; et al. Ultrahigh photocatalytic rate at a single-metal-atom-oxide. *Adv. Mater.* **2019**, *31*, 1903491. [CrossRef]
365. Cheng, Y.W.; Chang, Y.S.; Ng, K.H.; Wu, T.Y.; Cheng, C.K. Photocatalytic restoration of liquid effluent from oil palm agroindustry in Malaysia using tungsten oxides catalyst. *J. Clean. Prod.* **2017**, *162*, 205–219. [CrossRef]
366. Zheng, Q.; Lee, C. Visible light photoelectrocatalytic degradation of methyl orange using anodized nanoporous WO_3. *Electrochim. Acta* **2014**, *115*, 140–145. [CrossRef]
367. Scott-Emuakpor, E.; Paton, G.I.; Todd, M.J.; Macphee, D.E. Disinfection of E. coli contaminated water using tungsten trioxide-based photoelectrocatalysis. *Environ. Eng. Manag. J.* **2016**, *15*, 899–903.
368. Mei, L.; Zhao, H.; Lu, B. Ultra-efficient photocatalytic properties in porous tungsten oxide/graphene film under visible light irradiation. *Adv. Sci.* **2015**, *2*, 1500116. [CrossRef]
369. Malefane, M.E.; Ntsendwana, B.; Mafa, P.J.; Mabuba, N.; Feleni, U.; Kuvarega, A.T. In-situ synthesis of tetraphenylporphyrin/tungsten (VI) oxide/reduced graphene oxide (TPP/WO_3/RGO) nanocomposite for visible light photocatalytic degradation of Acid Blue 25. *ChemistrySelect* **2019**, *4*, 8379–8389. [CrossRef]
370. Ibrahim, Y.O.; Gondal, M.A.; Alaswad, A.; Moqbel, R.A.; Hassan, M.; Cevik, E.; Qahtan, T.F.; Dastageer, M.A.; Bozkurt, A. Laser-induced anchoring of WO_3 nanoparticles on reduced graphene oxide sheets for photocatalytic water decontamination and energy storage. *Ceram. Int.* **2020**, *46*, 444–451. [CrossRef]
371. Tong, M.X.; Yang, J.X.; Jin, Q.Y.; Zhang, X.; Gao, J.; Li, G.H. Facile preparation of amorphous carbon-coated tungsten trioxide containing oxygen vacancies as photocatalysts for dye degradation. *J. Mater. Sci.* **2019**, *54*, 10656–10669. [CrossRef]
372. Isari, A.A.; Mehregan, M.; Mehregan, S.; Hayati, F.; Kalantary, R.R.; Kakavandi, B. Sono-photocatalytic degradation of tetracycline and pharmaceutical wastewater using WO_3/CNT heterojunction nanocomposite under US and visible light irradiations: A novel hybrid system. *J. Hazard. Mater.* **2020**, *390*, 122050. [CrossRef]
373. Abe, R.; Takami, H.; Murakami, N.; Ohtani, B. Pristine simple oxides as visible light driven photocatalysts: Highly efficient decomposition of organic compounds over platinum-loaded tungsten oxide. *J. Am. Chem. Soc.* **2008**, *130*, 7780–7781. [CrossRef] [PubMed]
374. Hosseini, F.; Safaei, E.; Mohebbi, S. Modified WO_3 nanorod with Pt nanoparticle as retrievable materials in catalytic and photocatalytic aerobic oxidation of alcohols. *J. Nanopart Res.* **2017**, *19*, 240–251. [CrossRef]
375. Gunji, T.; Tsuda, T.; Jeevagan, A.J.; Hashimoto, M.; Kaneko, S.; Tanabe, T.; Matsumoto, F. Site-selective deposition of ordered intermetallic PtPb nanoparticle co-catalysts on WO_3 surfaces to enhance photocatalytic activity. *ECS Trans.* **2014**, *61*, 55–59. [CrossRef]
376. Georgieva, J.; Sotiropoulos, S.; Valova, E.; Armyanov, S.; Karanasios, N. Methanol oxidation and photo-oxidation at Pt/WO_3 electrocatalysts on graphite substrates. *J. Electroanal. Chem.* **2014**, *727*, 135–140. [CrossRef]

377. Kale, M.J.; Avanesian, T.; Christopher, P. Direct photocatalysis by plasmonic nanostructures. *ACS Catal.* **2014**, *4*, 116–128. [CrossRef]
378. Ding, J.; Chai, Y.; Liu, Q.; Liu, X.; Ren, J.; Dai, W.L. Selective deposition of silver nanoparticles onto WO_3 Nanorods with different facets: The correlation of facet-induced electron transport preference and photocatalytic activity. *J. Phys. Chem. C* **2016**, *120*, 4345−4353. [CrossRef]
379. Wei, W.; Yao, Y.; Zhao, Q.; Xu, Z.L.; Wang, Q.F.; Zhang, Z.T.; Gao, Y.F. Oxygen defect-induced localized surface plasmon resonance at the WO_{3-x} quantum dot/silver nanowire interface: SERS and photocatalysis. *Nanoscale* **2019**, *11*, 5535–5547. [CrossRef] [PubMed]
380. Capeli, R.A.; Dalmaschio, C.J.; Texeira, S.R.; Mastelaro, V.R.; Chiquito, A.J.; Longo, E.; Pontes, F.M. One-step controllable synthesis of three-dimensional WO_3 hierarchical architectures with different morphologies decorated with silver nanoparticles: Enhancing the photocatalytic activity. *RSC Adv.* **2020**, *10*, 6625–6639. [CrossRef]
381. Gao, L.; Gan, W.; Cao, G.; Zhan, X.; Qiang, T.; Li, J. Visible light activate Ag/WO_3 films based on wood with enhanced negative oxygen ions production properties. *Appl. Surf. Sci.* **2017**, *425*, 889–895. [CrossRef]
382. Ma, B.; Guo, J.; Dai, W.-L.; Fan, K. Ag-$AgCl/WO_3$ hollow sphere with flower-like structure and superior visible photocatalytic activity. *Appl. Catal. B* **2012**, *123–124*, 193–199. [CrossRef]
383. Adhikari, R.; Gyawali, G.; Sekino, T.; Lee, S.W. Microwave assisted hydrothermal synthesis of $Ag/AgCl/WO_3$ photocatalyst and its photocatalytic activity under simulated solar light. *J. Solid State Chem.* **2013**, *197*, 560–565. [CrossRef]
384. Fang, H.; Cao, X.; Yu, J.; Lv, X.; Yang, N.; Wang, T.; Jiang, W. Preparation of the all-solid-state Z-scheme $WO_3/Ag/AgCl$ film on glass accelerating the photodegradation of pollutants under visible light. *J. Mater. Sci.* **2019**, *54*, 286–301. [CrossRef]
385. Li, Q.; Yao, J.; Arif, M.; Huang, T.; Liu, X.; Duan, G.; Yang, X. Facile fabrication and photocatalytic performance of WO3 nanoplates in situ decorated with Ag/β-Ag_2WO_4 nanoparticles. *J. Environ. Chem. Eng.* **2018**, *6*, 1969–1978. [CrossRef]
386. Sahoo, D.P.; Patnaik, S.; Parida, K. Construction of a Z-scheme dictated $WO_{3-x}/Ag/ZnCr$ LDH synergistically visible light-induced photocatalyst towards tetracycline degradation and H_2 evolution. *ACS Omega* **2019**, *4*, 14721–14741. [CrossRef]
387. Zhuang, T.-T.; Liu, Y.; Li, Y.; Zhao, Y.; Wu, L.; Jiang, J.; Yu, S.-H. Integration of semiconducting sulfides for full-spectrum solar energy absorption and efficient charge separation. *Angew. Chem. Int. Ed.* **2016**, *55*, 6396–6400. [CrossRef]
388. Gao, L.; Gan, W.; Qiu, Z.; Zhan, X.; Qiang, T.; Li, J. Preparation of heterostructured WO_3/TiO_2 catalysts from wood fibers and its versatile photodegradation abilities. *Sci. Rep.* **2017**, *7*, 1102–1114. [CrossRef]
389. Ding, R.; Wang, K.; Hong, K.Q.; Zhang, Y.; Cui, Y.X. Hierarchical core-shell tungsten oxide/TiO2 nanowires as an effective photocatalyst. *Chem. Phys. Lett.* **2019**, *714*, 156–159. [CrossRef]
390. Bai, S.; Liu, H.; Sun, J.; Tian, Y.; Chen, S.; Song, J.; Luo, R.; Li, D.; Chen, A.; Liu, C.C. Improvement of TiO_2 photocatalytic properties under visible light by WO_3/TiO_2 and MoO_3/TiO_2 composites. *Appl. Surf. Sci.* **2015**, *338*, 61–68. [CrossRef]
391. Yang, L.; Si, Z.; Weng, D.; Yao, Y. Synthesis, characterization and photocatalytic activity of porous WO_3/TiO_2 hollow microspheres. *Appl. Surf. Sci.* **2014**, *313*, 470–478. [CrossRef]
392. Ramos-Delgado, N.A.; Hinojosa-Reyes, L.; Guzman-Mar, I.L.; Gracia-Pinilla, M.A.; Hernández-Ramírez, A. Synthesis by sol–gel of WO_3/TiO_2 for solar photocatalytic degradation of malathion pesticide. *Catal. Today* **2013**, *209*, 35–40. [CrossRef]
393. Ismail, A.A.; Abdelfattah, I.; Helal, A.; Al-Sayari, S.A.; Robben, L.; Bahnemann, D.W. Ease synthesis of mesoporous WO_3–TiO_2 nanocomposites with enhanced photocatalytic performance for photodegradation of herbicide imazapyr under visible light and UV illumination. *J. Hazard. Mater.* **2016**, *307*, 43–54. [CrossRef]
394. Ioannidou, E.; Frontistis, Z.; Antonopoulou, M.; Venieri, D.; Konstantinou, I.; Kondarides, D.I.; Mantzavinos, D. Solar photocatalytic degradation of sulfamethoxazole over tungsten—Modified TiO_2. *Chem. Eng. J.* **2017**, *318*, 143–152. [CrossRef]
395. Riboni, F.; Bettini, L.G.; Bahnemann, D.W.; Selli, E. WO_3–TiO_2 vs. TiO_2 photocatalysts: Effect of the W precursor and amount on the photocatalytic activity of mixed oxides. *Catal. Today* **2013**, *209*, 28–34. [CrossRef]
396. Ki, S.J.; Park, Y.-K.; Kim, J.-S.; Lee, W.-J.; Lee, H.; Jung, S.-C. Facile preparation of tungsten oxide doped TiO_2 photocatalysts using liquid phase plasma process for enhanced degradation of diethyl phthalate. *Chem. Eng. J.* **2019**, *377*, 120087. [CrossRef]
397. Khan, H.; Rigamonti, M.G.; Patience, G.S.; Boffito, D.D. Spray dried TiO_2/WO_3 heterostructure for photocatalytic applications with residual activity in the dark. *Appl. Catal. B* **2018**, *226*, 311–323. [CrossRef]
398. Rimoldi, L.; Giordana, A.; Cerrato, G.; Falletta, E.; Meroni, D. Insights on the photocatalytic degradation processes supported by TiO_2/WO_3 systems. The case of ethanol and tetracycline. *Catal. Today* **2019**, *328*, 210–215. [CrossRef]
399. Dominguez, S.; Huebra, M.; Han, C.; Campo, P.; Nadagouda, M.N.; Rivero, M.J.; Ortiz, I.; Dionysiou, D.D. Magnetically recoverable TiO_2-WO_3 photocatalyst to oxidize bisphenol A from model wastewater under simulated solar light. *Environ. Sci. Pollut. Res.* **2017**, *24*, 12589–12598. [CrossRef] [PubMed]
400. Huang, W.; Wang, J.; Bian, L.; Zhao, C.; Liu, D.; Guo, C.; Yang, B.; Cao, W. Oxygen vacancy induces self-doping effect and metalloid LSPR in non-stoichiometric tungsten suboxide synergistically contributing to the enhanced photoelectrocatalytic performance of WO_{3-X}/TiO_{2-X} heterojunction. *Phys. Chem. Chem. Phys.* **2018**, *20*, 17268—17278. [CrossRef]
401. Rey, A.; García-Munoz, P.; Hernández-Alonso, M.D.; Mena, E.; García-Rodríguez, S.; Beltrán, F.J. WO_3–TiO_2 based catalysts for the simulated solar radiation assisted photocatalytic ozonation of emerging contaminants in a municipal waste water treatment plant effluent. *Appl. Catal. B* **2014**, *154–155*, 274–284. [CrossRef]
402. Rusu, M.; Baia, M.; Pap, Z.S.; Danciu, V.; Baia, L. Structural investigations of TiO_2–WO_3–Au porous composites. *J. Mol. Struct.* **2014**, *1073*, 150–156. [CrossRef]

403. Kovács, G.; Baia, L.; Vulpoi, A.; Radu, T.; Karácsonyi, É.; Dombi, A.; Hernádi, K.; Danciu, V.; Simon, S.; Pap, Z. TiO_2/WO_3/Au nanoarchitectures' photocatalytic activity, "from degradation intermediates to catalysts' structural peculiarities", Part I: Aeroxide P25 based composites. *Appl. Catal. B* **2014**, *147*, 508–517. [CrossRef]
404. Baia, L.; Vulpoi, A.; Radu, T.; Karácsonyc, É.; Domic, A.; Hernádi, K.; Danciu, V.; Simon, S.; Norén, K.; Canton, S.E.; et al. TiO_2/WO_3/Au nanoarchitectures' photocatalytic activity "from degradation intermediates to catalysts' structural peculiarities" Part II: Aerogel based composites—Fine details by spectroscopic means. *Appl. Catal. B* **2014**, *148–149*, 589–600. [CrossRef]
405. Khan, H.; Rigamonti, M.G.; Boffito, D.C. Enhanced photocatalytic activity of Pt-TiO_2/WO_3 hybrid material with energy storage ability. *Appl. Catal. B* **2019**, *252*, 77–85. [CrossRef]
406. Rengifo-Herrera, J.A.; Frenzel, R.A.; Blanco, M.N.; Pizzio, L.R. Visible-light-absorbing mesoporous TiO_2 modified with tungstosilicicacid as photocatalyst in the photodegradation of 4-chlorophenol. *J. Photochem. Photobiol. A* **2014**, *289*, 22–30. [CrossRef]
407. Maleki, A.; Moradi, F.; Shahmoradi, B.; Rezaee, R.; Lee, S.-M. The photocatalytic removal of diazinon from aqueous solutions using tungsten oxide doped zinc oxide nanoparticles immobilized on glass substrate. *J. Mol. Liquids* **2020**, *297*, 111918. [CrossRef]
408. Ebrahimi, R.; Maleki, A.; Zandsalimi, Y.; Ghanbari, R.; Shahmoradi, B.; Rezaee, R.; Safari, M.; Joo, S.W.; Daraei, H.; Puttaiah, S.H.; et al. Photocatalytic degradation of organic dyes using WO_3-doped ZnO nanoparticles fixed on a glass surface in aqueous solution. *J. Ind. Eng. Chem.* **2019**, *73*, 297–305. [CrossRef]
409. Sajjad, A.K.L.; Sajjad, S.; Iqbal, A.; Ryma, N.U.A. ZnO/WO_3 nanostructure as an efficient visible light catalyst. *Ceram. Int.* **2018**, *44*, 9364–9371. [CrossRef]
410. Mugunthan, E.; Saidutta, M.B.; Jagadeeshbabu, P.E. Photocatalytic activity of ZnO-WO_3 for diclofenac degradation under visible light irradiation. *J. Photochem. Photobiol. A* **2019**, *383*, 111993.
411. Arshad, M.; Ehtisham-ul-Haque, S.; Bilal, M.; Ahmad, N.; Ahmad, A.; Abbas, M.; Nisar, J.; Khan, M.I.; Nazir, A.; Ghaffar, A.; et al. Synthesis and characterization of Zn doped WO_3 nanoparticles: Photocatalytic, antifungal and antibacterial activities evaluation. *Mater. Res. Express* **2020**, *7*, 015407. [CrossRef]
412. Al-Amshany, Z.M.; Hussein, M.A. Novel Pd/$ZnWO_4$ nanocomposite materials for photocatalytic degradation of atrazine. *Appl. Nanosci.* **2018**, *8*, 527–536. [CrossRef]
413. Wang, H.; Wang, C.; Cui, X.; Qin, L.; Ding, R.; Wang, L.; Liu, Z.; Zheng, Z.; Lv, B. Design and facile one-step synthesis of $FeWO_4/Fe_2O_3$ di-modified WO_3 with super high photocatalytic activity toward degradation of quasiphenothiazine dyes. *Appl. Catal. B* **2018**, *221*, 169–178. [CrossRef]
414. Ngigi, E.M.; Nomngongo, P.N.; Ngila, J.C. Synthesis and application of Fe-doped WO_3 nanoparticles for photocatalytic degradation of methylparaben using visible-light radiation and H_2O_2. *Catal. Lett.* **2019**, *149*, 49–60. [CrossRef]
415. Ullah, I.; Munir, A.; Muhammad, S.; Ali, S.; Khalid, N.; Zubair, M.; Sirajuddin, M.; Hussain, S.Z.; Ahamed, S.; Khan, Y.; et al. Influence of W-doping on the optical and electrical properties of SnO_2 towards photocatalytic detoxification and electrocatalytic water splitting. *J. Alloy Compd.* **2020**, *827*, 154247. [CrossRef]
416. Ahmad, M.; Khan, M.Y.; Sadaf, S.; Iqbal, S.; Nawaz, F.; Iqbal, J. Novel indigo-dye-doped graphene-supported Mn/WO_3 nanocomposite as visible light photocatalyst for degradation of methylene blue dye. *Mater. Res. Express* **2019**, *6*, 055050. [CrossRef]
417. Rosaline, D.R.; Inbanathan, S.S.R.; Suganthi, A.; Rajarajan, M.; Kavitha, G.; Srinivasan, R.; Hegazy, H.H.; Umar, A.; Alagarni, H.; Manikandan, E. Visible-light driven photocatalytic degradation of eosin yellow (EY) dye based on NiO-WO_3 nanoparticles. *J. Nanosci. Nanotechnol.* **2020**, *20*, 924–933. [CrossRef] [PubMed]
418. Silveira, J.V.; Moraes, E.C.; Moura, J.V.B.; Ghosh, A.; Senna, C.A.; Archanjo, B.S.; Vasconcelos, T.L.; Souza Filho, A.G.; Freire, P.T.C.; Luz Lima, C. Mo-doped WO_3 nanowires for adsorbing methylene blue dye from wastewater. *J. Mater. Sci.* **2020**, *55*, 6429–6440. [CrossRef]
419. Wang, F.; Di Valentin, C.; Pacchioni, G. Doping of WO_3 for photocatalytic water splitting: Hints from density functional theory. *J. Phys. Chem. C* **2012**, *116*, 8901–8909. [CrossRef]
420. Malefane, M.E. Feleni, U.; Kuvarega, A.T. Cobalt (II/III) oxide and tungsten (VI) oxide p-n heterojunction photocatalyst for photodegradation of diclofenac sodium under visible light. *J. Environ. Chem. Eng.* **2020**, *8*, 103560. [CrossRef]
421. Zhang, K.; Wang, J.; Jiang, W.; Yao, W.; Yang, H. Self-assembled perylene diimide based supramolecular heterojunction with Bi_2WO_6 for efficient visible-light-driven photocatalysis. *Appl. Catal. B* **2018**, *232*, 175–181. [CrossRef]
422. Priya, A.; Arunachalam, P.; Selvi, A.; Madhavan, J.; Al-Mayouf, A.M. Synthesis of $BiFeWO_6/WO_3$ nanocomposite and its enhanced photocatalytic activity towards degradation of dye under irradiation of light. *Colloid Surf. A* **2018**, *559*, 83–91.
423. Abbas, H.A.; Nasr, R.A.; Abu-Zurayk, R.; Al Bawab, A.; Jamil, T.S. Decolourization of crystal violet using nano-sized novel fluorite structure $Ga_2Zr_{2-x}W_xO_7$ photocatalyst under visible light irradiation. *R. Soc. Open Sci.* **2020**, *7*, 191632. [CrossRef]
424. Wan, J.; Liu, Y.; Yin, H.; Huang, X.; Bai, M. Synthesis and photocatalytic performance of a WSe_2QD/N-GO nanocomposite under visible light Irradiation. *J. Mater. Sci.* **2020**, *55*, 10009–10021. [CrossRef]
425. Aslam, M.; Qamar, M.T.; Soomro, M.T.; Ismail, I.M.I.; Rehan, Z.A.; Ashrafd, M.W.; Hameed, A. The effect of cerium alteration on the photocatalytic performance of WO_3 in sunlight exposure for water decontamination. *RSC Adv.* **2016**, *6*, 2436–2449. [CrossRef]
426. Tahir, M.B.; Sagir, M. Carbon nanodots and rare metals (RM = La, Gd, Er) doped tungsten oxide nanostructures for photocatalytic dyes degradation and hydrogen production. *Sep. Purif. Technol.* **2019**, *209*, 94–102. [CrossRef]
427. Wen, J.; Xie, J.; Chen, X.; Li, X. A review on g-C_3N_4-based photocatalysts. *Appl. Surf. Sci.* **2017**, *391*, 72–123. [CrossRef]

428. Xiao, T.; Tang, Z.; Yang, Y.; Tang, L.; Zhou, Y.; Zou, Z. In situ construction of hierarchical WO_3/g-C_3N_4 composite hollow microspheres as a Z-scheme photocatalyst for the degradation of antibiotics. *Appl. Catal. B* **2018**, *220*, 417–428. [CrossRef]
429. Antoniadou, M.; Arfanis, M.K.; Ibrahim, I.; Falaras, P. Bifunctional g-C_3N_4/WO_3 thin films for photocatalytic water purification. *Water* **2019**, *11*, 2439. [CrossRef]
430. Jones, D.R.; Gomez, V.; Bear, J.C.; Rome, B.; Mazzali, F.; McGettrick, J.D.; Lewis, A.R.; Margadonna, S.; Al-Masry, W.A.; Dunnill, C.W. Active removal of waste dye pollutants using Ta_3N_5/$W_{18}O_{49}$ nanocomposite fibres. *Sci. Rep.* **2017**, *7*, 4090. [CrossRef] [PubMed]
431. Thwala, M.M.; Dlamini, L.N. Photocatalytic reduction of Cr(VI) using Mg-doped WO_3 nanoparticles. *Environ. Technol.* **2020**, *41*, 2277–2292. [CrossRef] [PubMed]